UNIVERSITY OF OKLAHOMA

GRADUATE COLLEGE

INVESTIGATION AND REAL-TIME MONITORING FOR SAFE WASTE-WATER DISPOSAL WITH A FOCUS ON ARBUCKLE GROUP, OKLAHOMA

A THESIS

SUBMITTED TO THE GRADUATE FACULTY

in partial fulfillment of the requirements for the

Degree of

MASTER OF SCIENCE

By

MAULIN GOGRI
Norman, Oklahoma
2018

INVESTIGATION AND REAL-TIME MONITORING FOR SAFE WASTE-WATER DISPOSAL WITH A FOCUS ON ARBUCKLE GROUP, OKLAHOMA

A THESIS APPROVED FOR THE
MEWBOURNE SCHOOL OF PETROLEUM AND GEOLOGICAL ENGINEERING

BY

_____
Dr. Zulfiquar Reza, Chair

_____
Dr. Deepak Devegowda

_____
Dr. Matthew Pranter

_____
Dr. Kurt Marfurt

_____
Dr. Mashhad Fahs

I dedicate this thesis to my Parents and Brother and almighty God.

Acknowledgments

I feel privileged to have pursued my graduate studies at University of Oklahoma. I would like to thank many people for their efforts for my success. First and foremost, I would sincerely like to thank my advisor, ***Dr. Zulfiquar Reza***. His constant support and mentoring helped me during my graduate school. His continuous motivation and guidance while carrying out the research and publishing manuscripts proved to be very beneficial. With his vast industry experience, I was fortunate to receive guidelines at par with industry standards while carrying out my graduate studies. It was truly an honor to have a research advisor and mentor like him.

I would also like to thank ***Dr. Kurt Marfurt*** and ***Dr. Matthew Pranter***, for their constant guidance and feedback during the entire course of the project. This thesis is part of the project. And along with them, ***Dr. Deepak Devegowda*** and ***Dr. Mashhad Fahs***, for being part of my Masters' committee and providing me feedback on my thesis. I am also thankful to my fellow colleagues, Gabriel Machhado and Garrett Hickman, who were also the part of this project. I would refer our collaborative work as 'I' while presenting this thesis. I would also like to deeply thank ***Shah Kabir*** for sharing his incredible knowledge and feedback while I was publishing our work. I would like to thank Bradley Cronk and Tien Phan for their collaboration during publications.

I would like to thank my parents for their incredible support and motivation, not only during Masters' but during my entire career till date. A very special thanks to my brother ***Saumil Gogri*** to always be available to discuss sports and investment

news and motivating me for fitness. And a special mention to my cousins Ami and Pooja. I would also like to thank my friends at OU. Norman felt like home because of the friends Abhijeet, Abhishek, Anvit, Aparajita, Dhanya, Diken, Gayatri, Harsh, Himanshu, Janny, Jyotaditya, Nauman, Nidhi, Richa, Rohit, Saket, Sami, Sarvesh, Shantanu, Soham, Subbu, Sumeer, Tabish, Tarek, Vineet and many more. I would like to extend my thanks to Yogashri Pradhan for helping me while reviewing my thesis.

Table of Contents

List of Tables

List of Figures

Abstract

Increase in the earthquakes in the State of Oklahoma in recent years has been tremendous with wastewater disposal considered to be the primary reason behind this increase. A large quantity of wastewater is being injected in the Arbuckle-Group and the connected basement in North Central Oklahoma. Because they are not hydrocarbon-bearing, very little information is available about these formations in the region. Additionally, there is a need to understand the dynamics of wastewater disposal process in order to design safe operational practices with proper monitoring. This thesis attempts to address both of these issues.

A major goal of this study is the characterization of the Arbuckle-Group which has been the primary disposal zones in North Central Oklahoma. To better understand the potential hydraulic coupling between the Arbuckle and underlying basement, an integrated subsurface characterization effort has been undertaken to this front by a team of earth-scientists and petroleum engineers. This thesis emphasizes the engineering aspect of that effort focused on Payne County in North Central Oklahoma. Geophysical, geological, and experimental data from various sources have been acquired, analyzed and employed in the model construction of the disposal zones in this area. Injection volumes, wellhead pressure data and well completion reports from 29 injection wells in the study area are acquired from Oklahoma Corporation Commission. Using a modified-Hall analysis which formed the basis of the work, I constructed a 3D simulation model of the Arbuckle-Group and the underlying basement that defined the lateral distribution,

petrophysical properties (including porosity and permeability), and major fault surfaces integrating the available static and dynamic data to characterize the disposal zones, I found the average porosity and permeability of the Arbuckle Group to be around 7% and 10 mD, respectively. The sealing and transmissive nature of a few major faults has been determined as well.

With the help of a suite of reservoir models using Arbuckle-specific data, I devised workflows to better understand the injection well dynamics. Important parameters that affect the disposal process have been identified by a number of Designs of Experiments (DoEs) using relevant uncertain variables and operational parameters. Using modified-Hall analysis I defined normal injection behavior and critically analyzed the safe limits of wastewater disposal operations. A smart and safe disposal-well monitoring scheme is developed based on the learnings, which will help disposal-well management become more economical and environmentally friendly.

Chapter 1: Background and Motivation

According to The Office of the Secretary of Energy and Environment (Oklahoma), the State of Oklahoma had been experiencing limited but consistent level of seismicity in the recorded history dating back to 1882 (earthquakes.ok.gov). However, North Central Oklahoma has seen a recent and dramatic rise in the number of earthquake events. This cannot be solely attributed to the natural causes. Walsh and Zoback (2015) discussed the increase in the seismicity through the **Figure 1**. They also mentioned that in recent years there has been no state that has witnessed an increase in seismicity as much as Oklahoma. Also, Jacobs (2016) reported that more than 2,500 seismic events of over 2.5 on Richter scale have occurred between 2010 and 2015 in Oklahoma.

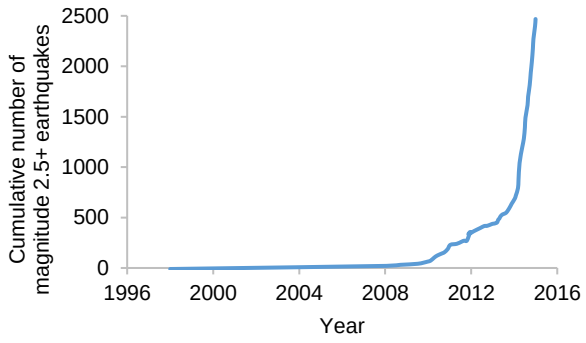

Figure 1. Cumulative number of magnitude 2.5+ earthquakes in Oklahoma After: Walsh and Zoback (2015)

Multiple studies including but not limited to Zoback (2010), Horton (2012), Kim (2013), McGarr et al. (2015), Walters et al. (2015) and more have indicated that the seismicity is linked with the disposal of the wastewater generated during the multistage hydraulic fracturing operations. On the contrary, several authors

attributed hydraulic fracturing operations to be the primary cause of induced seismicity (Holland, 2011, 2013; BC Oil and Gas Commission, 2011; The Royal Society, 2012; Friberg et al., 2014; Walters et al., 2015). However, this thesis will not focus on hydraulic-fracturing induced seismicity.

In general, permeable formations are the target of injection in Class II injection wells. According to U.S. Geological Survey (2017), 40,000 out of 150,000 Class II injection wells, operating in the USA, are used for oil and gas wastewater disposal. The total produced water volume in the USA exceeded 20 billion stock-tank barrels (STB) in 2007 as reported by Veil and Clark (2011). Enhanced recovery operations consumed over 55% of this water, whereas about 39% of the water was disposed of by injection. However, a small fraction of these disposal wells has caused induced seismicity, thereby triggering a large concern among the public and the governmental organizations. This has led federal as well as state bodies to find ways to mitigate the risk of induced seismicity. The State of Oklahoma Underground Injection Control division recognizes three necessary components for significant injection-induced seismicity: sufficient pressure buildup from disposal activities, faults, and a pathway allowing the increased pressure to communicate with the faults.

Resource plays such as the Mississippian Limestone of Oklahoma and Kansas are characterized by 95% hypersaline water production. Although Oklahoma is currently covered by thousands of water disposal wells, it is only the North Central part of the state that has experienced a recent increase in seismicity. Murray (2013 and 2014), and Walsh and Zoback (2015) state that, in Central

Oklahoma, most of the wastewater disposal occurs in the Arbuckle Group. **Figure 2** shows a map of injection wells penetrating the Arbuckle Group and **Figure 3** shows magnitude 2.5+ earthquakes since 2014 along with the injection wells penetrating the Arbuckle formation. Also, it appears that this formation is in hydraulic communication with the underlying crystalline basement. The increase in pressure in the Arbuckle Group propagates to the basement causing disturbances in that region.

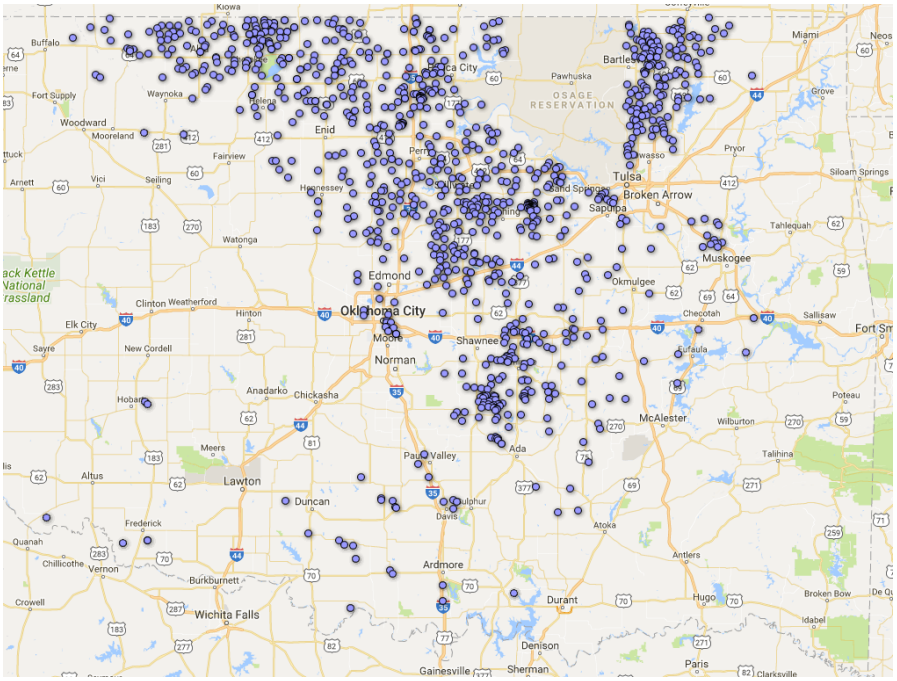

Figure 2. Map of injection wells penetrating Arbuckle-Group (Source: www.earthquakes.ok.gov)

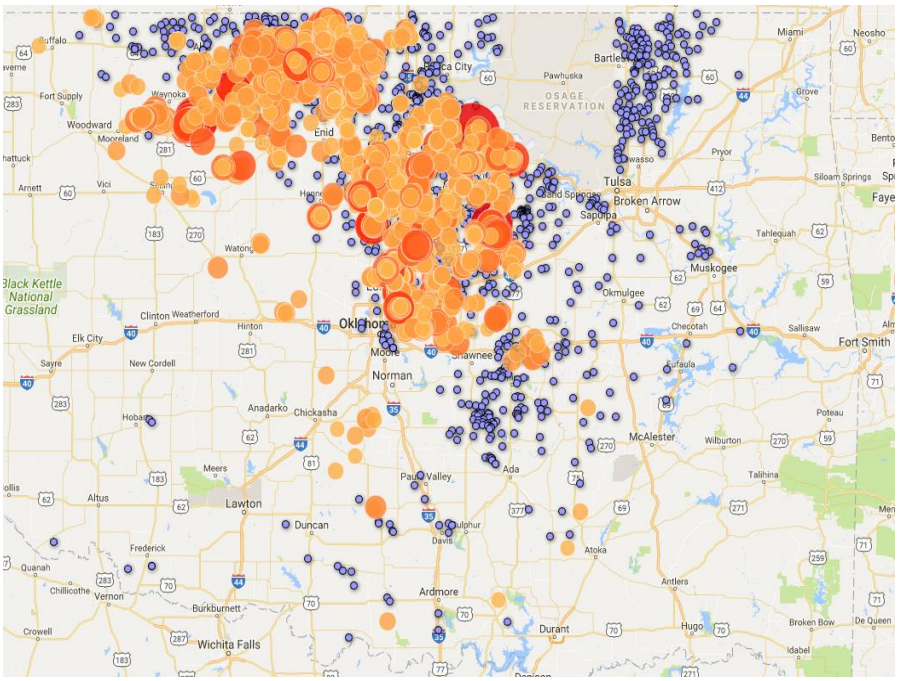

Figure 3. Map of magnitude 2.5+ earthquakes since 2014 in Oklahoma overlying on wells penetrating Arbuckle-Group (Source: www.earthquakes.ok.gov)

To study this issue, a project was awarded by Oklahoma Geological Survey (OGS) to the professors of University of Oklahoma - Dr. Kurt Marfurt, Dr. Matthew Pranter and Dr. Zulfiquar Reza. A study area in North Central Oklahoma is chosen, where evidently, there has been no study involving characterization of the Arbuckle-basement wastewater disposal system using the datasets and methods that shall be described in detail in the following sections. This area is situated in the Payne County, Oklahoma. 29 injection wells owned by 8 different operators are located in this study area. The wells are named as Well A through Well AC.

Figure 4a shows location of Payne County in the map of Oklahoma. The study area is chosen based on available 3D seismic survey containing Arbuckle

Group and basement along with other overlying formations. **Figure 4b** shows the location of wells of penetrating the Arbuckle in the study area. Here, I have considered Well E as a representative well to demonstrate the application of the analysis. **Figure 4c** shows a chair display through the seismic amplitude volume.

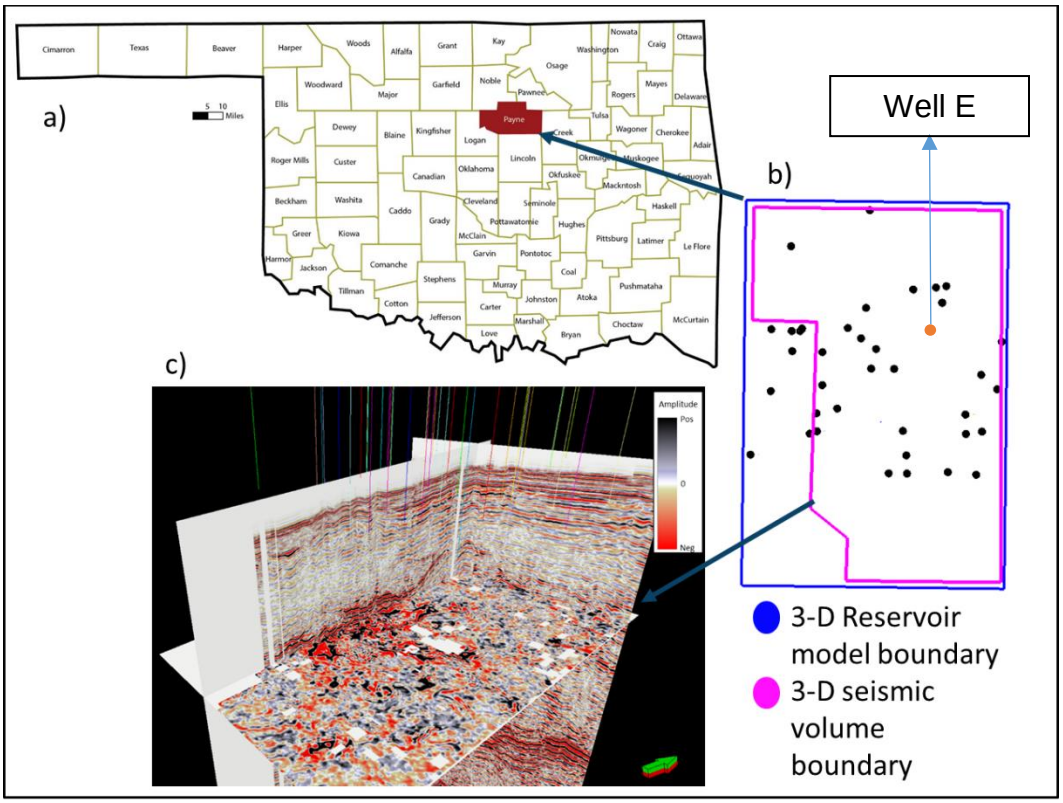

Figure 4. (a) Map showing the location of Payne County, Oklahoma., (b) Boundaries (in magenta) of the 3D seismic survey and (in blue) of the 3D cellular model. Black dots indicate the wells that penetrated the Arbuckle in the study area. (c) A chair display through seismic amplitude volume. The top of the survey has been cropped 20 ms above the top Arbuckle Formation. The time slice is approximately 800 ms below the top of basement.

I will now describe the geological setting for Arbuckle Group. The Arbuckle Group of Central and Northern Oklahoma were deposited during the

Cambrian and Ordovician as an extensive carbonate platform that covered most of the region. Strata in the study area are 100's to 1,000's of feet thick with extensive fracturing, dolomitization, and karstification in many of the sub-units. In the study area, these large carbonate units are underlain by 50 - 100 ft of interbedded sandstones and dolomites that make up the Reagan Sandstone (Stringer, 1958), which lies on top of the faulted Pre-Cambrian/Cambrian Granites and Rhyolites that form the shallow part of the basement throughout much of Oklahoma (Johnson, 1991). Historically, the heavily fractured and karsted carbonate formations have been utilized for salt water disposal (SWD) wells throughout much of the State of Oklahoma (Murray, 2015).

The major objectives of this project include integrating modern 3D seismic, well logs, and injection data from Payne County, Oklahoma to:

- To establish a stratigraphic and structural framework for Arbuckle-basement system as well as the overlying sedimentary section to the ground surface.
- To measure seismic attributes and use them to better map structure, stratigraphy, and large-scale diagenetic features of the Arbuckle-Group, such as collapse structures.
- To create 3D geocellular models of the subsurface geology that depict the spatial distribution of rock types and petrophysical properties.
- To use these 3D geocellular models as input to fluid flow simulations for history matching and to better understand subsurface dynamic pressure and injection conditions that can lead to characterization of Arbuckle-Group.

This thesis will present the engineering aspect of the project.

Additionally, various sources demonstrate that an improvement in operational practices of wastewater disposal is essential in order to curb the effect of induced seismicity. Although a few steps have been taken by the bodies of state government, such as Baker (2016), there is no apparent reduction in the seismicity. The other area of focus, in this thesis, will be to understand the disposal process in various scenarios and offer tools to monitor the wastewater disposal process. And based on these learnings, a safe water disposal procedure will be provided that might prove useful to reduce the effect of induced seismicity. The objectives of this thesis are described in Chapter 2.

Different aspects of this project have been presented and published in various fora. Some of the key publications are mentioned below:

1. A poster titled 'Multidisciplinary Characterization of Geomechanical Properties and Flow Behavior of the Coupled Arbuckle-Basement System, Payne County, Northern Oklahoma' was presented at AAPG Annual Convention and Exhibition 2017, Houston, TX.
2. A poster titled 'Multidisciplinary Geomechanical and Geophysical Characterization of the Coupled Arbuckle-Basement System, Payne County, Northern Oklahoma' was presented at AAPG Mid-Continent Section Meeting 2017 held at Oklahoma City, OK.
3. A paper (SPE-187083-MS) titled 'Prognosis for Safe Water-Disposal-Well Operations and Practices Based on Reservoir Flow Modeling and Real-Time Performance Analysis' was presented at SPE Annual Technical Conference and Exhibition 2017 held at San Antonio, TX.

4. A journal article (SPE-187083-PA) with the title ‘Prognosis for Safe Water-Disposal-Well Operations and Practices Based on Reservoir Flow Modeling and Real-Time Performance Analysis’ has been accepted for publication in SPE Reservoir Evaluation and Engineering Journal for 2018.

Chapter 2: Objectives

The major tasks of the study include characterizing Arbuckle Group in North Central Oklahoma region and offer a safe water disposal procedure by studying the wastewater disposal process. Key data available to characterize the Arbuckle-Group include 3D seismic survey, well logs, injection and completion data. I will describe and analyze the available data in detail in Chapter 3. The objectives will be to review and study the survey and well logs data. Further, to measure and analyze the core properties and to tie the core data with the log data. And to check the quality of the injection data and to understand the injection-well behavior using diagnostics tool. Additionally, to link seismicity with various injection parameters.

Chapter 4 will consist of methodology for constructing simulation model as well as conduct and analyze history matching. The objectives will be to review the 3D geocellular model, porosity model and the permeability model. Then, to create a robust 3D simulation model using the available datasets and to design well controls based upon the behavior of the well. Furthermore, to identify the parameters for history matching and their ranges. To point out the parameters that are impactful during history matching. And, to history match the injection rates and bottomhole pressures. Thus, I will be able to characterise the Arbuckle Group in North Central Oklahoma region.

I will discuss the other major task, which is to learn a safe operational procedure for disposal, in Chapter 5. The objectives laid out for this task will be to improve understanding of wastewater disposal process in confined space, to

examine the effect of various disposal-zone properties, to investigate operations practices in disposal-well performance, to identify critical parameters affecting water injection process, to identify diagnostics for water-disposal well monitoring and finally establish a workflow for safe water-disposal operations.

Chapter 6 will consist of points of discussion including limitations and assumptions as well as the conclusions drawn from the study. Chapter 7 shall indicate direction in which further work can be carried out on the subject matter.

Chapter 3: Data Acquisition and Analysis

In this chapter, datasets used in the study are described and analyzed. I will present the maps showing seismicity in the study area along with the location of injection wells. Next, the geophysical data used and analyzed by the geophysics experts for this study is described, along with the well log data used by the geology experts. The procedure of the core experiments is presented along with its analysis. I will explain the analysis on the injection data starting from quality checking the data to understand well behavior. And lastly, various injection parameters are linked with the seismicity events.

3.1. Seismicity Map

There have been several occurrences of earthquakes in the study area. **Figure 5** shows location of earthquakes occurred between in the years 2014, 2015 and 2016. The injection wells penetrating the Arbuckle-Group in the study area are also shown in the figure. From the available injection data, it is found that maximum injection occurs in the years 2014, 2015 and 2016 for the wells of interest. I will describe the relationship of seismicity with other injection parameters in section 3.6.

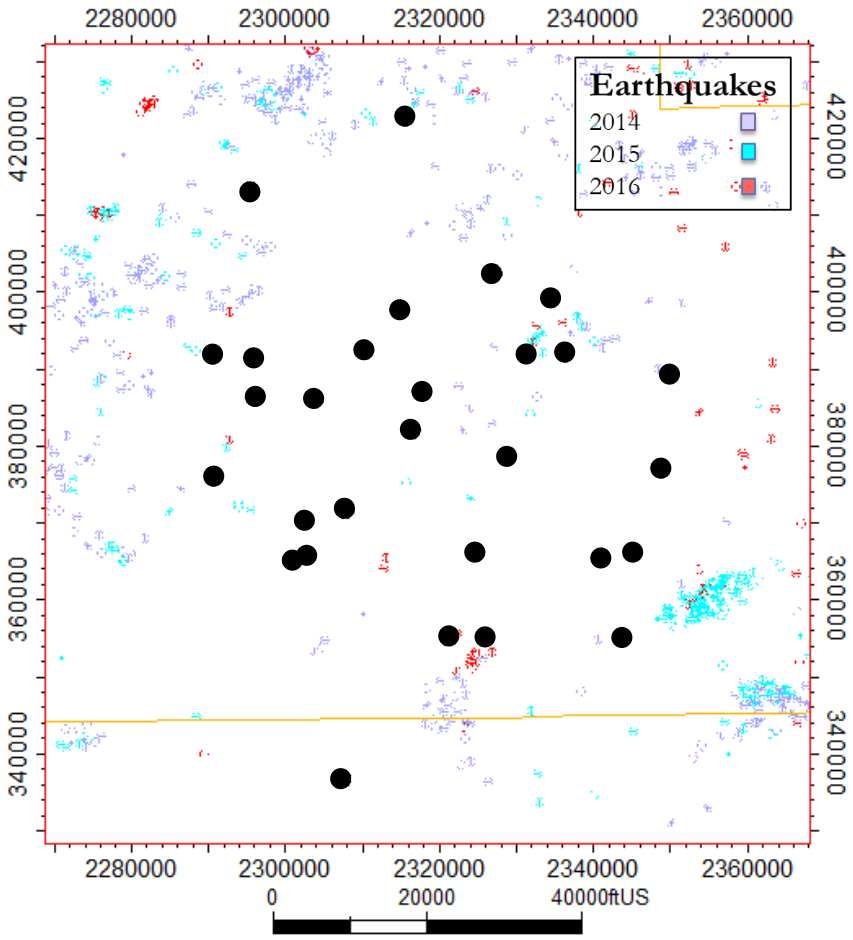

Figure 5. Map showing earthquakes that occurred in years 2014, 2015 and 2016 and the injection wells in the study area

3.2. Geophysical Data

I used geophysical data to initiate characterizing the subsurface properties of the Arbuckle-basement system (along with overlying formations) in North-Central Oklahoma. The following geophysical data is used:

- A 3D pre-stack time-migrated seismic data volume cropped above the Arbuckle Group (in order to protect the economic sensitivity of the overlying Mississippi Lime and Red Fork plays by the data owner)
- Seismic horizons for both the Arbuckle Group top and the basement top
- Velocity models for the cropped-out portion of the seismic

The seismic volume cropped above Arbuckle Group, seismic horizons and velocity models for the cropped-out portion of the seismic is shown in **Figure 6**.

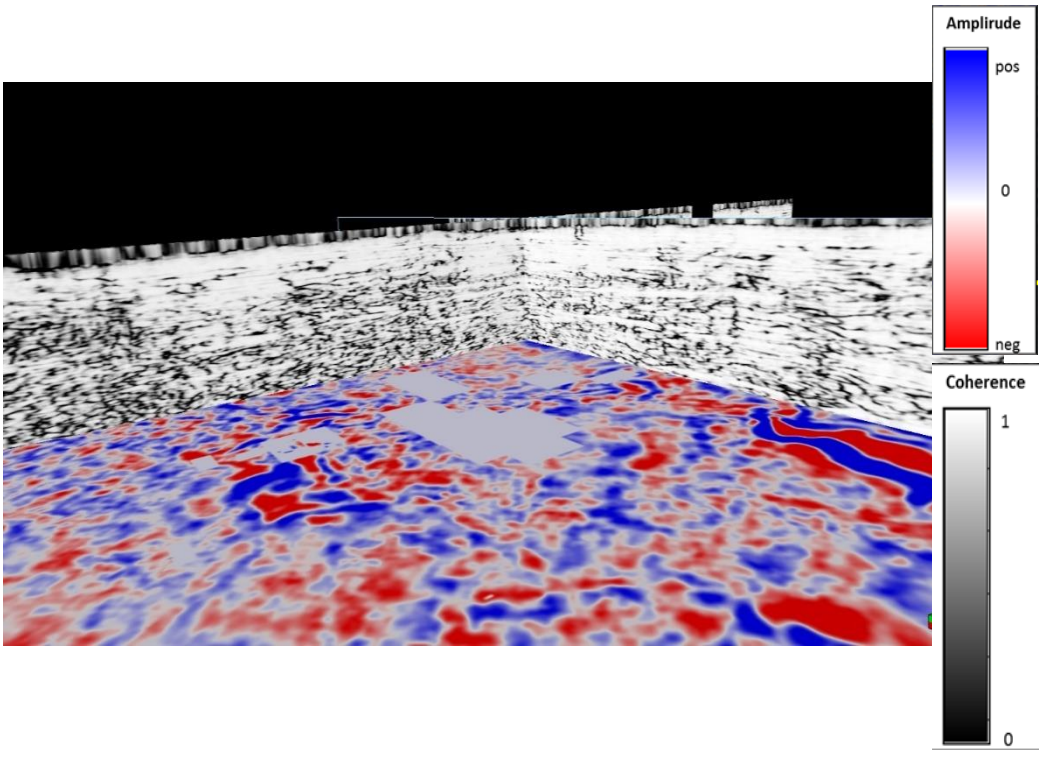

Figure 6. Seismic volume cropped above Arbuckle Group, seismic horizons and velocity models for the cropped-out portion of the seismic

3.3. Log Data

I digitized a suite of raster logs obtained from 29 wells that penetrate the Arbuckle Group to facilitate a more quantitative interpretation using modern statistical correlation techniques. A depth range of 3,000 - 6,000 ft. (914 - 1,282 m) of log data are available for each well. Digitized log curves include gamma ray (GR), bulk density (RHOB), neutron porosity (NPHI), density porosity (DPHI), spontaneous potential (SP), shallow resistivity (RESS), medium resistivity (RESM), and deep resistivity (RESD). I picked formation tops from these logs to create structural and stratigraphic cross sections. **Figure 7** shows the well section containing well logs and tops of various formation for 4 wells in the study area and **Figure 8** shows type log of a gamma ray, resistivity and porosity logs along with the major formation tops.

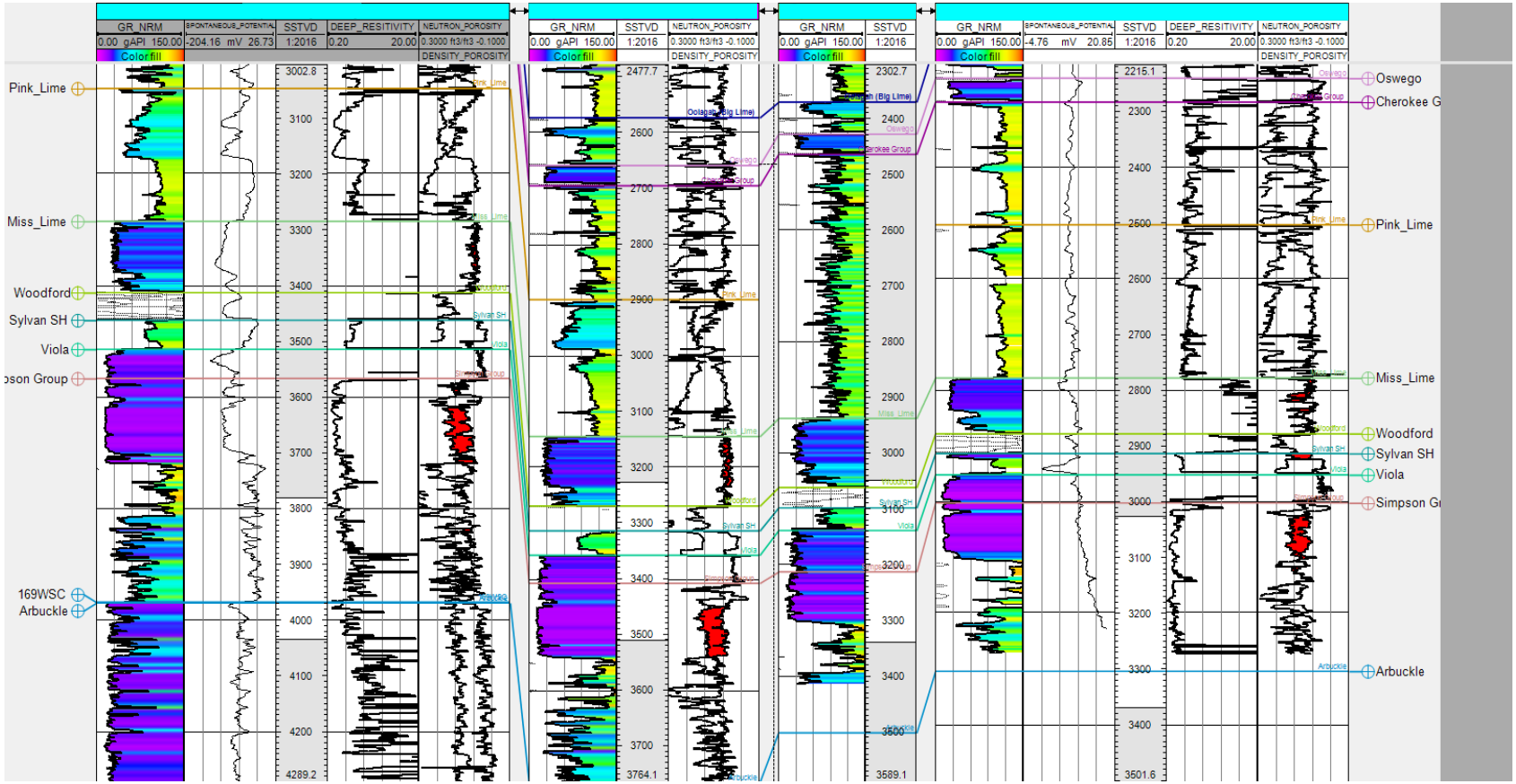

Figure 7. Well section showing well logs and identified Tops of the formation

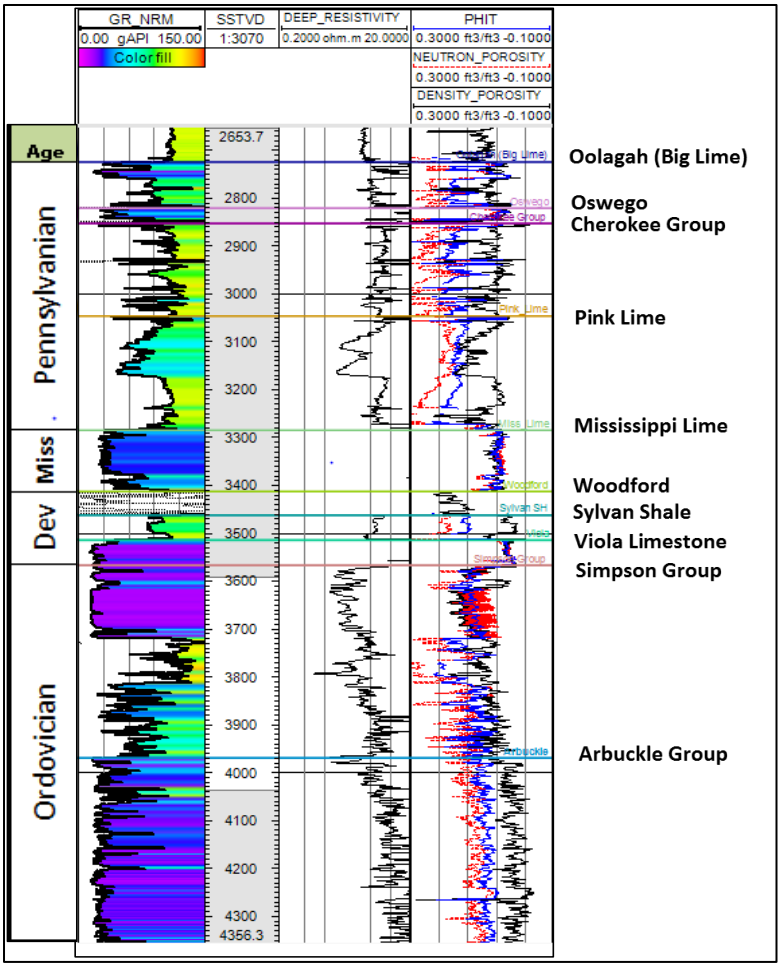

Figure 8. Type log of a gamma ray (to the left) and resistivity and porosity (to the right) showing the major formation tops picked from the Ordovician Arbuckle Group up through the Pennsylvanian Oolagah Limestone showing their ages

3.4. Experimental Core Data Acquisition and Analysis

I present the methodology and results of the experiments carried out to obtain petrophysical properties of Amoco's slim-hole advanced drilling SHADS No. 4 well. This well is not present in the study area. However, the various formations from which the samples are obtained are part of the Arbuckle Group or

the basement formation. I conducted four experiments on seven cores from different depths to obtain various properties. Depth locations of all the core samples are presented in **Figure 9**. I prepared the samples in accordance to the requirements of the respective experiment. The experiments consist of measuring porosity and permeability using the Automated Porosimeter-Permeameter, measuring porosity and grain density using Low-Pressure Pycnometer (LPP), obtaining mineralogy using Fourier Transform Infrared Spectroscopy (FTIR), and measuring ultrasonic velocities to obtain geomechanical properties.

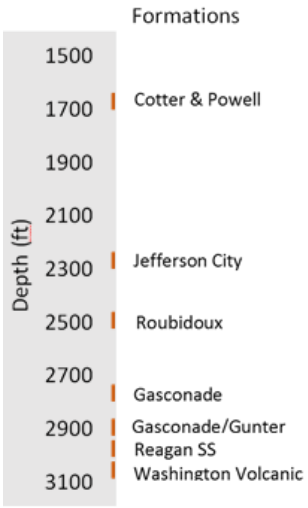

Figure 9. Core depths and formations encountered in the Catoosa, OK, Amoco Shads #4 Well

3.4.1. Methodology

3.4.1.1. Automated Porosimeter-Permeameter

The automated porosimeter-permeameter is based on Boyle's Law to measure porosity. The schematic (**Figure 10**) shows the setup of the equipment.

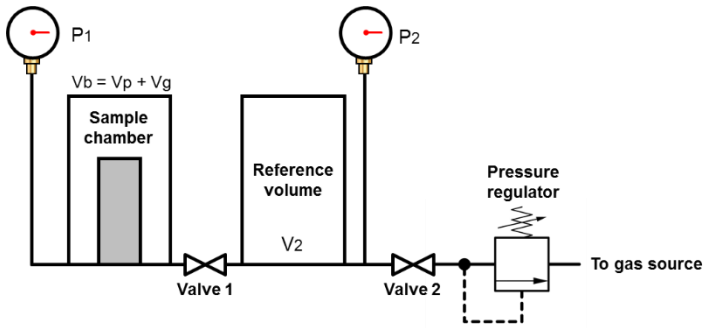

Figure 10. Schematic of Automated Porosimeter-Permeameter (After Henao, 2017)

Core sample is placed in a chamber with known volume, v_1, at a low pressure, P_1. Another chamber having volume, v_2, is connected with the first chamber and is pressurized typically at P_2 = 100 psia, with helium gas. On opening of the valve 1, the pressure in both the chambers equalizes to P_f, as the helium expansion takes place in the chamber with sample. Grain volume, V_G, can be determined using Boyle's Law. And porosity can be calculated using the bulk volume, using the following equations:

$$V_G = \frac{v_1(P_f - P_1) + v_2(P_f - P_2)}{P_f - P_2}, \quad (1)$$

$$\phi = \frac{V_B - V_G}{V_B}. \quad (2)$$

Klinkenberg-corrected permeability to helium was measured using the pressure decay technique to determine permeability to a resolution of 0.001 mD.

3.4.1.2. Low-Pressure Pycnometer (LPP)

Porosity and grain density measurement is carried out using Low-Pressure Pycnometer (LPP). Bulk volume of the sample is measured using Archimedes

Principle. For this, mercury immersion technique is used. The sample is immersed in a mercury bath and the volume of mercury displaced is noted as bulk volume.

The step-by-step procedure to measure porosity and grain density, as suggested by Karastathis (2007), using Low-Pressure Pycnometer is presented below:

1. Obtain a plug with approximately 12g (+/- 2g) weight.
2. Heat the sample at 100ºC for 8 hours in a vacuum oven. Level of vacuum can be ~ 800 mbar.
3. Remove the sample from the oven and allow it to cool for at least 30 minutes in a desiccator.
4. Using a balance, measure sample weight (m_1). From mercury immersion and the dimensions, obtain the bulk volume (V_B) of the sample.
5. Crush the plug. Be careful during this step as the loss of any sample during crushing should be minimized.
6. Transfer the powdered sample into the Low-Pressure Pycnometer (LPP) aluminum cell.
7. Measure weight m_1 of the powdered sample. Calculate the weight loss Δm which could have occurred during crushing and transferring.

   $$\Delta m = m_1 - m_2 \quad (3)$$

8. Keep the powdered sample packed in an aluminum cell in a vacuum at for 8 hours at 100ºC in order to remove all the gas, free water, and volatile hydrocarbons.

9. Cool the LPP aluminum cell containing the sample for 30 minutes in a desiccator.
10. Measure the weight m_3 again, after cooling.
11. Place the aluminum cell in the Low-Pressure Pycnometer and the average grain volume V_G is obtained after running the test three times.

The grain density is calculated by:

$$\rho_G = \frac{m_3}{V_G}, \tag{4}$$

and corrected grain volume is calculated by:

$$V_G{}^* = V_G + \frac{\Delta m}{\rho_G}, \tag{5}$$

and the water free porosity is calculated by:

$$\phi = \frac{V_B - V_G{}^*}{V_B} \times 100. \tag{6}$$

3.4.1.3. Fourier Transform Infrared Spectroscopy (FTIR)

Fourier Transform Infrared (FTIR) Spectroscopy is used to measure the mineral composition of the samples. The detailed discussion of this technique can be found in the literature by Sondergeld and Rai (1993) and Ballard (2007). The steps followed for measuring mineralogy using FTIR spectroscopy are:

1. Obtain a small portion of the sample and crush it to an extent that the sample gets as fine as talcum powder.
2. Ash the powder to remove the organic carbon and heat it at 100^{o}C for 24 hours to get rid of moisture from the sample.

3. Add 0.0005 gm of the powder 0.3 gm of potassium bromide (KBr). Press the mixture under 10 kpsi pressure to create a semi-transparent 13 mm disk.
4. Obtain the absorbance spectrum by passing the infrared beam through this disk in the spectrometer.
5. To obtain the mineralogy of the sample, an inversion scheme (Sondergeld and Rai, 1993) is applied to the obtained spectrum.

The minerals are analyzed and quantified in terms of weight % using the above procedure.

3.4.1.4. Ultrasonic Velocity Measurements

Henao (2017) discussed the methodology to carry out ultrasonic velocity measurements. Ultrasonic compressional waves with magnitude 1 MHz and shear waves with magnitude 500 kHz are passed through the sample under confining pressure. Travel time of these waves along the samples are measured as Δt_p and Δt_s. Based on the following equations, compressional (V_p) and shear (V_s) wave velocities are calculated using the sample length (L):

$$V_p = \frac{L}{\Delta t_p}, \tag{7}$$

$$V_s = \frac{L}{\Delta t_s}. \tag{8}$$

Using the bulk density and the wave velocities of the samples, dynamic Poisson's ratio, v_{dyn}, Bulk Modulus, K_b, Shear modulus, G, and Young's modulus, YME, are calculated:

$$v_{dyn} = \frac{1}{2}\frac{(V_p/V_s)^2 - 2}{(V_p/V_s)^2 - 1}, \quad (9)$$

$$K_b = \rho\left(V_p{}^2 - \frac{4}{3}V_s{}^2\right), \quad (10)$$

$$G = \rho\left(V_s{}^2\right), \quad (11)$$

$$YME = \rho\left(V_p{}^2 - \frac{4}{3}V_s{}^2\right)(3 - 6v_{dyn}). \quad (12)$$

3.4.2. Results and Analysis

This section presents results and analysis based on the methodology presented in the section above. I tested seven plugs, numbered as Plug #1, 15, 18, 22, 25B, 26 and 29. Properties obtained for Plug #1 (**Figure 11**) are presented below. This plug is obtained from the depth 1671.1 ft and from Cotter and Powell formation. **Figure 12** presents the porosity obtained from automated porosimeter and LPP. **Figure 13** presents the permeability obtained from automated permeameter. Grain and bulk density measured using LPP are 2.82 gm/cm^3 and 2.49 gm/cm^3. Mineral composition of the sample is presented in **Figure 14**. And, the geomechanical quantities calculated using ultrasonic wave velocities are presented in **Table 1**.

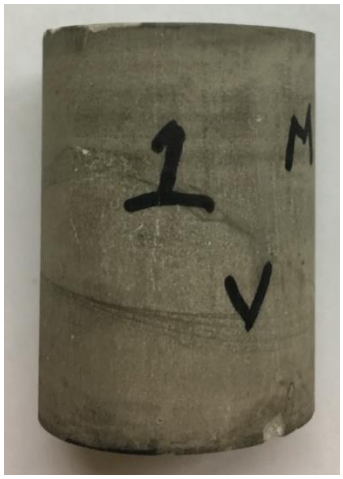

Figure 11. Plug #1 from the Cotter and Powell Formation at a depth of 1671.1 ft

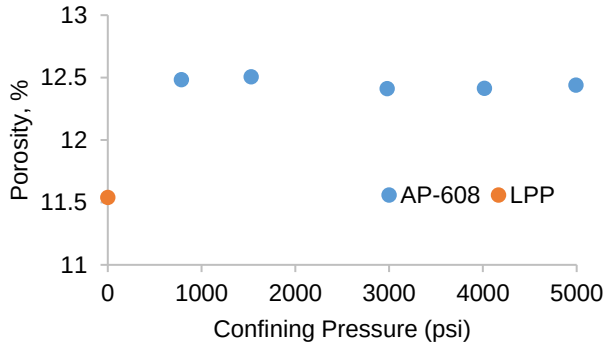

Figure 12. Porosity for Plug #1 from the Cotter and Powell Formation at a depth of 1671.1 ft

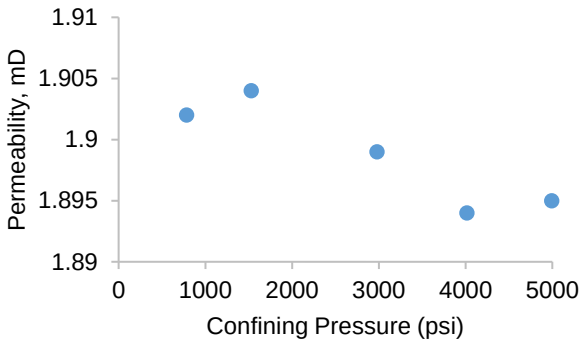

Figure 13. Permeability for plug #1 from the Cotter and Powell Formation at a depth of 1671.1 ft

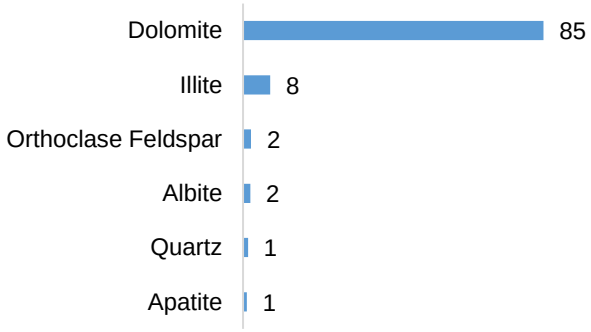

Figure 14. Mineralogy for Plug #1 from the Cotter and Powell Formation at a depth of 1671.1 ft

Table 1. Geomechanical quantities calculated from sonic velocities for the Plug #1 from Cotter and Powell Formation at a depth of 1671.1 ft

Confining Pressure	PR	YME (GPa)	Kb (GPa)	G (GPa)
750	0.24	57.37	36.89	3.35
1000	0.24	59.94	38.71	3.50
1500	0.26	62.74	43.01	3.62
2000	0.27	64.41	45.71	3.69
3000	0.26	66.88	45.97	3.86
4000	0.26	68.87	48.31	3.96
5000	0.26	70.44	49.43	4.04

Properties obtained for Plug #15 (**Figure 15**) are presented below. This plug is obtained from the depth 2267.15 ft and from Jefferson City formation. **Figure 15** presents the porosity obtained from automated porosimeter and LPP. **Figure 16** presents the permeability obtained from automated permeameter. Grain and bulk density measured using LPP are 2.81 gm/cm^3 and 2.45 gm/ cm^3 respectively. Mineral composition of the sample is presented in **Figure 17**. Compressional wave velocities were not calculated for this sample.

Figure 15. Plug #15 from the Jefferson City Formation at a depth of 2267.15 ft

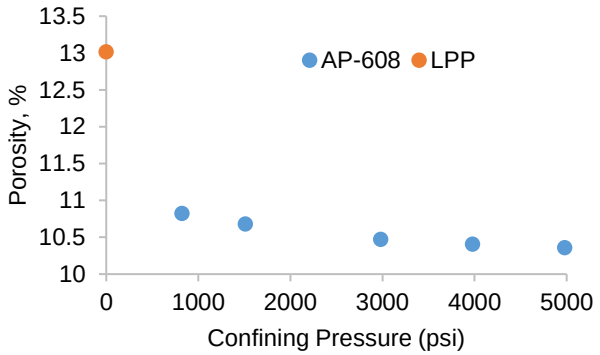

Figure 16. Porosity for Plug #15 from the Jefferson City Formation at a depth of 2267.15 ft

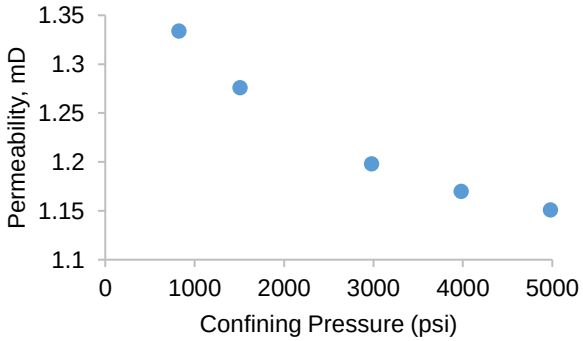

Figure 17. Permeability for plug #15 from the Jefferson City Formation at a depth of 2267.15 ft

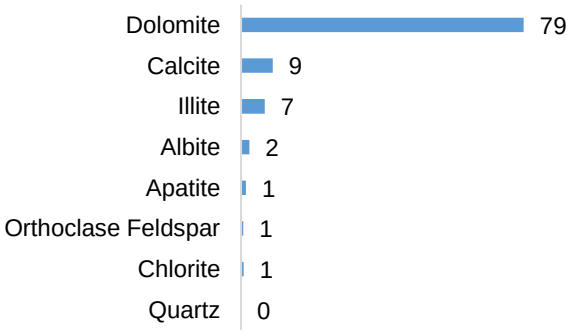

Figure 18. Mineralogy for Plug #15 from the Jefferson City Formation at a depth of 2267.15 ft

Properties obtained for Plug #18 (**Figure 19**) are presented below. This plug is obtained from the depth 2492.08 ft and from Roubidoux formation. **Figure 20** presents the porosity obtained from automated porosimeter and LPP. **Figure 21** presents the permeability obtained from automated permeameter. Grain and bulk density measured using LPP are 2.83 gm/cm^3 and 2.49 gm/cm^3 respectively. Mineral composition of the sample is presented in **Figure 22**. And, the geomechanical quantities calculated using ultrasonic wave velocities are presented in **Table 2**.

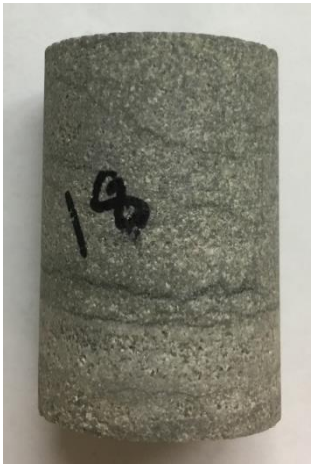

Figure 19. Plug #18 from the Roubidoux Formation at a depth of 2492.08 ft

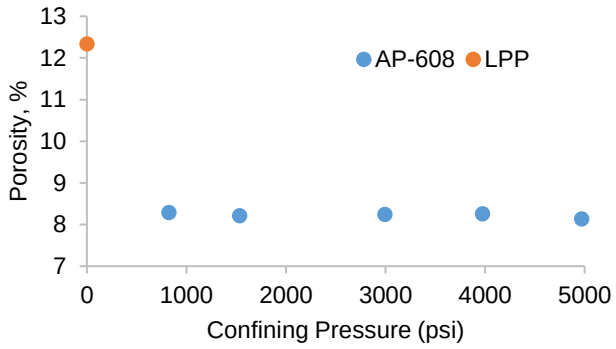

Figure 20. Porosity for Plug #18 from the Roubidoux Formation at a depth of 2492.08 ft

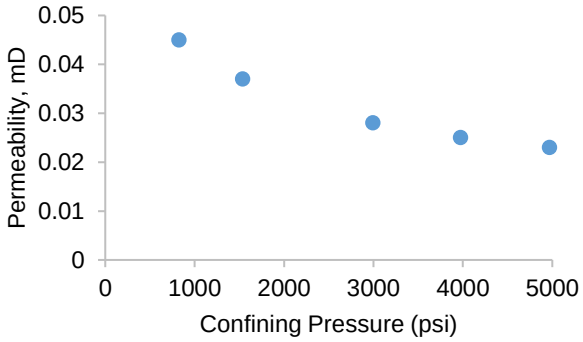

Figure 21. Permeability for plug #18 from the Roubidoux Formation at a depth of 2492.08 ft

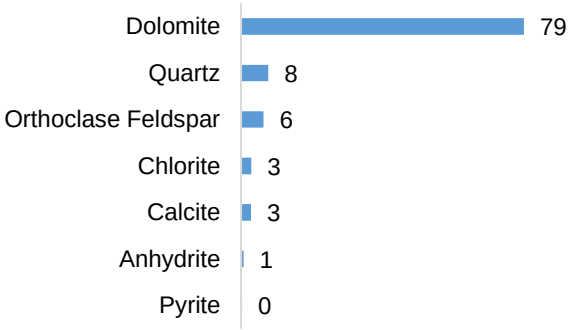

Figure 22. Mineralogy for Plug #18 from the Roubidoux Formation at a depth of 2492.08 ft

Table 2. Geomechanical quantities calculated from Sonic velocities for Plug #18 from the Roubidoux Formation at a depth of 2492.08 ft

Confining Pressure	PR	YME (GPa)	Kb (GPa)	G (GPa)
250	0.20	55.08	30.70	3.32
500	0.23	56.87	34.93	3.36
750	0.23	58.08	36.16	3.42
1000	0.24	58.85	37.50	3.45
1500	0.24	61.67	39.78	3.60
2000	0.25	63.17	42.50	3.66
3000	0.25	65.11	44.22	3.76

4000	0.25	66.07	44.92	3.82
5000	0.25	66.94	45.20	3.87

Properties obtained for Plug #22 (**Figure 23**) are presented below. This plug is obtained from the depth 2766 ft and from Gasconade formation. **Figure 24** presents the porosity obtained from automated porosimeter and LPP. **Figure 25** presents the permeability obtained from automated permeameter. Grain and bulk density measured using LPP are 2.83 gm/cm^3 and 2.57 gm/cm^3 respectively. Mineral composition of the sample is presented in **Figure 26**. And, the geomechanical quantities calculated using ultrasonic wave velocities are presented in **Table 3**.

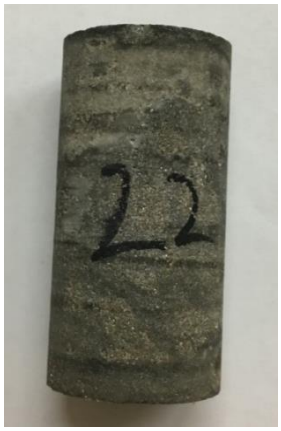

Figure 23. Plug #22 from the Gasconade Formation at a depth of 2766 ft

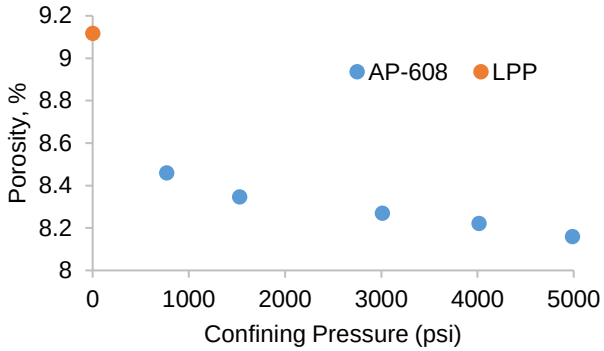

Figure 24. Porosity for Plug #22 from the Gasconade Formation at a depth of 2766 ft

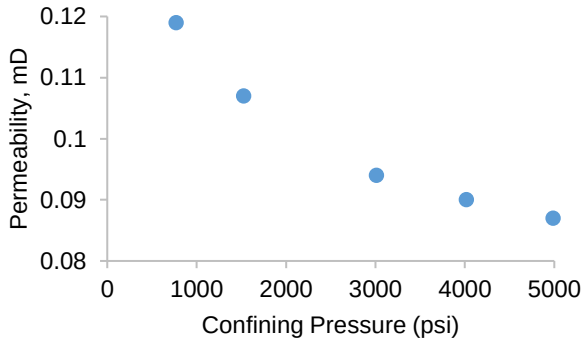

Figure 25. Permeability for plug #22 from the Gasconade Formation at a depth of 2766 ft

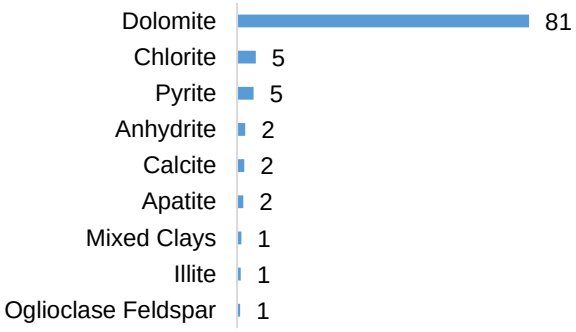

Figure 26. Mineralogy for Plug #22 from the Gasconade Formation at a depth of 2766 ft

Table 3. Geomechanical quantities calculated from sonic velocities for Plug #22 from the Gasconade Formation at a depth of 2766 ft

Confining Pressure	PR	YME (GPa)	Kb (GPa)	G (GPa)
250	0.20	51.82	28.48	3.14
500	0.21	54.65	31.88	3.26
750	0.23	55.80	34.47	3.29
1000	0.24	56.77	36.14	3.32
1500	0.25	59.23	39.33	3.44
2000	0.25	61.22	40.82	3.55
3000	0.25	64.23	42.05	3.74
4000	0.25	65.87	43.49	3.83
5000	0.27	67.89	48.77	3.88

Properties obtained for Plug #25B (**Figure 27**) are presented below. This plug is obtained from the depth 2893.1 ft and from Gasconade/Gunter SS formation. **Figure 28** presents the porosity obtained from automated porosimeter and LPP. **Figure 29** presents the permeability obtained from automated permeameter. Grain and bulk density measured using LPP are 2.84 gm/cm^3 and 2.80 gm/cm^3 respectively. Mineral composition of the sample is presented in **Figure 30**. And, the geomechanical quantities calculated using ultrasonic wave velocities are presented in **Table 4**.

Figure 27. Plug #25B from the Gasconade/Gunter SS Formation at a depth of 2893.1 ft

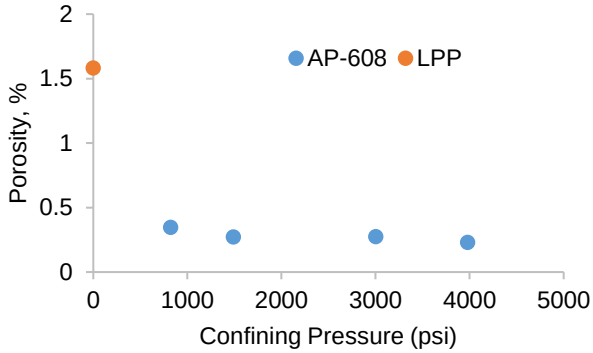

Figure 28. Porosity for Plug #25B from the Gasconade/Gunter SS Formation at a depth of 2893.1 ft

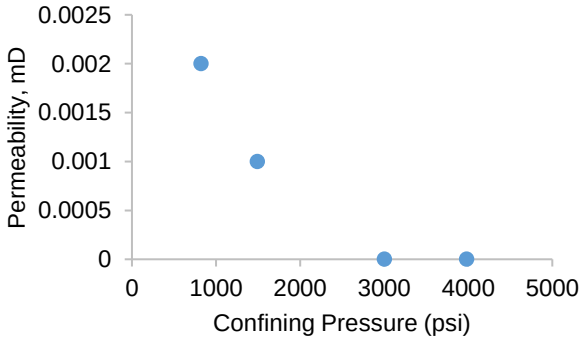

Figure 29. Permeability for plug #25B from the Gasconade/Gunter SS Formation at a depth of 2893.1 ft

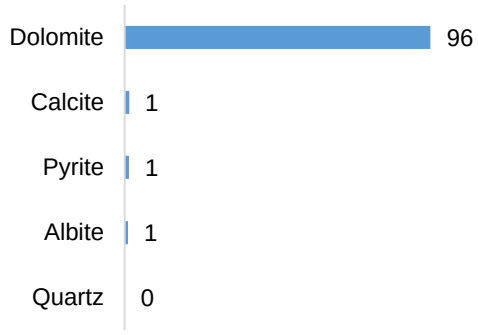

Figure 30. Mineralogy for Plug #25B from the Gasconade/Gunter SS Formation at a depth of 2893.1 ft

Table 4. Geomechanical quantities calculated from Sonic velocities for Plug #25B from the Gasconade/Gunter SS Formation at a depth of 2893.1 ft

Confining Pressure	PR	YME (GPa)	Kb (GPa)	G (GPa)
250	0.23	80.50	50.08	4.74
500	0.25	81.45	53.57	4.74
750	0.25	82.80	55.69	4.79
1000	0.25	84.22	56.60	4.88
1500	0.25	85.32	56.44	4.96
2000	0.25	86.35	56.98	5.02
3000	0.26	88.27	60.44	5.09
4000	0.26	89.72	61.52	5.17
5000	0.26	91.33	62.55	5.27

Properties obtained for Plug #26 (**Figure 31**) are presented below. This plug is obtained from the depth 2973.8 ft and from Reagan SS Formation. **Figure 32** presents the porosity obtained from automated porosimeter and LPP. **Figure 33** presents the permeability obtained from automated permeameter. Grain and bulk density measured using LPP are 2.63 gm/cm^3 and 2.12 gm/cm^3 respectively.

Mineral composition of the sample is presented in **Figure 34**. And, the geomechanical quantities calculated using ultrasonic wave velocities are presented in **Table 5**.

Figure 31. Plug #26 from the Reagan SS Formation at a depth of 2973.8 ft

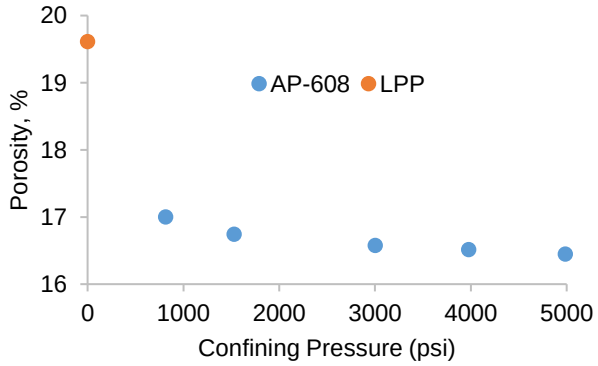

Figure 32. Porosity for Plug #26 from the Reagan SS Formation at a depth of 2973.8 ft

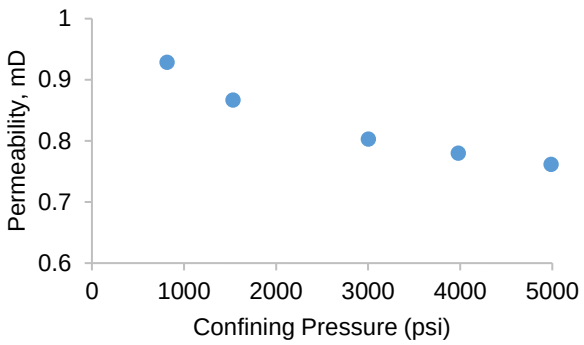

Figure 33. Permeability for plug #26 from the Reagan SS Formation at a depth of 2973.8 ft

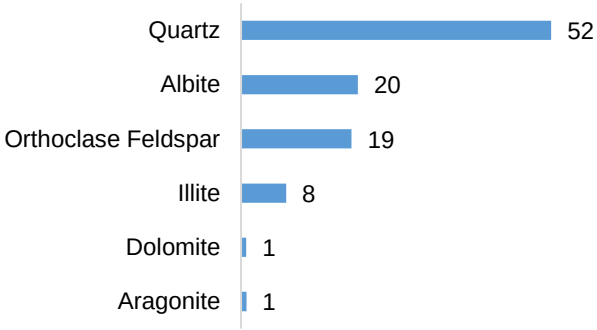

Figure 34. Mineralogy for Plug #26 from the Reagan SS Formation at a depth of 2973.8 ft

Table 5. Geomechanical quantities calculated from sonic velocities for Plug #26 from the Reagan SS Formation at a depth of 2973.8 ft

Confining Pressure	PR	YME (GPa)	Kb (GPa)	G (GPa)
250	0.20	21.77	12.00	1.32
500	0.18	22.89	11.82	1.41
750	0.16	23.97	11.69	1.50
1000	0.20	25.93	14.59	1.56
1500	0.18	28.17	14.64	1.73
2000	0.20	29.90	16.49	1.81
3000	0.21	32.06	18.19	1.93
4000	0.21	33.07	18.90	1.98
5000	0.21	34.18	19.61	2.05

Properties obtained for Plug #29 (**Figure 35**) are presented below. This plug is obtained from the depth 3056.35 ft and from Washington Volcanic Group. **Figure 36** presents the porosity obtained from automated porosimeter and LPP. **Figure 37** presents the permeability obtained from automated permeameter. Grain and bulk density measured using LPP are 2.72 gm/cm^3 and 2.70 gm/cm^3 respectively. Mineral composition of the sample is presented in **Figure 38**. And, the geomechanical quantities calculated using ultrasonic wave velocities are presented in **Table 6**.

Figure 35. Plug #29 from the Washington Volcanic Group at a depth of 3056.35 ft

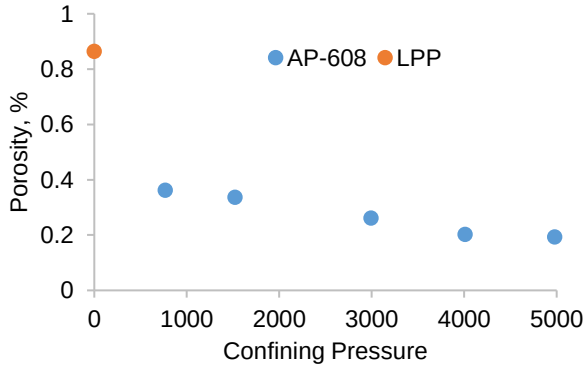

Figure 36. Porosity for Plug #29 from the Washington Volcanic Group at a depth of 3056.35 ft

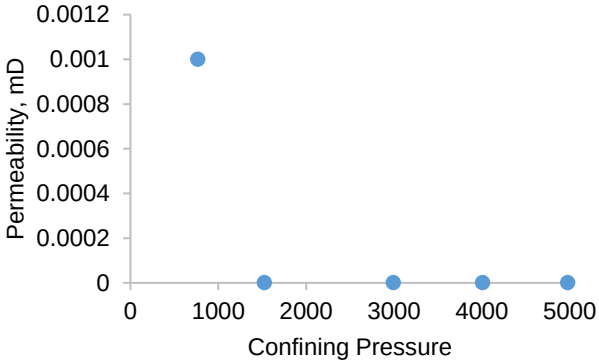

Figure 37. Porosity for plug #29 from the Washington Volcanic Group at a depth of 3056.35 ft

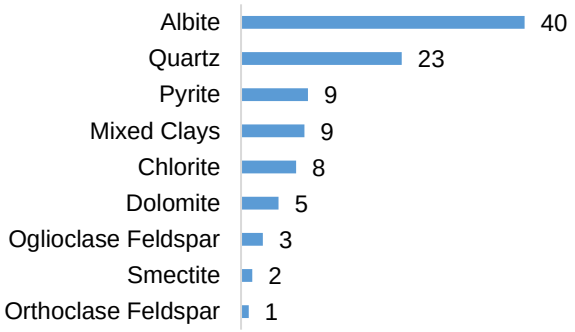

Figure 38. Mineralogy for Plug #29 from the Washington Volcanic Group at a depth of 3056.35 ft

Table 6. Geomechanical quantities calculated from sonic velocities for Plug #29 from the Washington Volcanic Group at a depth of 3056.35 ft

Confining Pressure	PR	YME (GPa)	Kb (GPa)	G (GPa)
750	0.22	89.31	53.11	5.31
1000	0.22	91.26	53.67	5.44
1500	0.22	92.49	54.92	5.50
2000	0.22	93.75	55.39	5.58
3000	0.22	94.65	56.99	5.61
4000	0.23	96.06	59.08	5.67
5000	0.23	98.12	59.84	5.80

3.5. Injection Data

As part of pre-analysis, I investigated well performance of the 29 disposal wells, within the seismic survey area, using daily injection rates, surface-tubing pressures and well-completion reports. Completion reports are obtained from OCC. Publicly disclosed injection data is highly variable, with the type of reporting that has changed radically over the past 20 years.

3.5.1. Data Quality Analysis

I diligently performed quality control of the available data with anomalous data identified and either corrected (whenever possible) or removed from further analyses. The pressure and the injection rate data are analyzed to find anomalies and are rectified. Data quality analysis for one of the well (Well E) is shown in **Figure 39**.

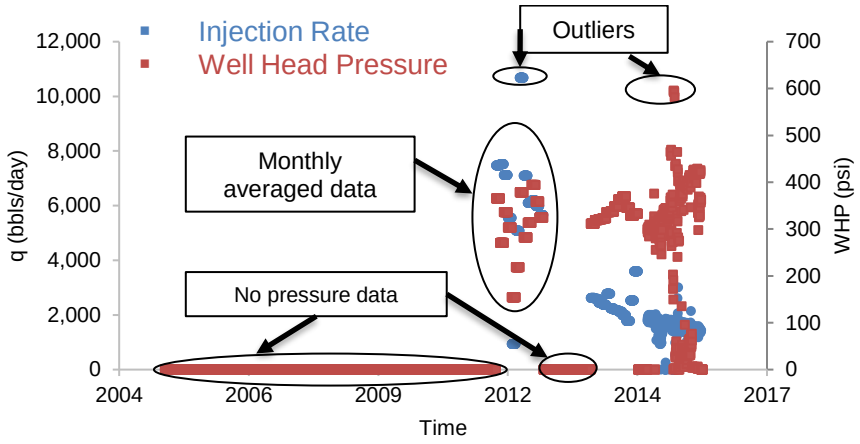

Figure 39. Pressure and Injection Rate data analysis (Well E)

The data points with no pressure data were not considered for the analysis. I ignored the outliers, such as very high pressure or injection rates. The possible reasons for zero data or very high range of the data could be erroneous measurements by the meters, meters not operational, etc.

3.5.2. Conversion of Wellhead Pressures to Bottom Hole Pressures

Bottom hole pressure was required for the analysis, however, only wellhead pressure data was available. I converted the wellhead pressures to bottom-hole

pressure using a commercial software and also carried out sensitivity analysis to identify any artifact introduced in the pressure conversion process. **Figure 40** shows the results of the pressure conversion for Well E.

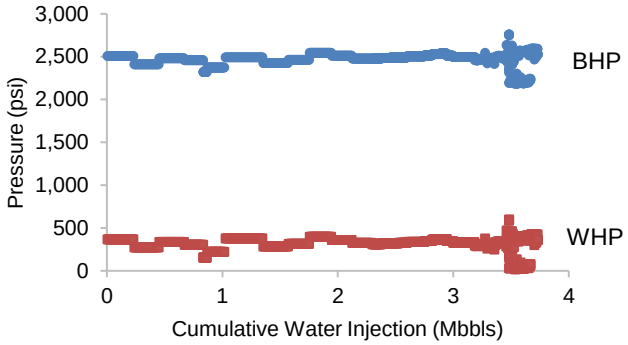

Figure 40. Conversion of wellhead pressure to bottomhole pressure (Well E)

Sensitivity analysis was carried out for the following parameters: salinity of the water, the pressure conversion correlation, and the temperature of injection water. Salinity values of 40000 ppm, 80000 ppm and 250000 ppm were chosen for sensitivity analysis. **Figure 41** shows the results by changing various salinity values. Salinity value was taken to be 190,000 ppm during the conversion, also recommended by an operator in that region. Four flow co-relations namely PETEX-2, Beggs and Brill, Mukherjee and Brill, and Duns and Ros Modified were considered for sensitivity analysis. **Figure 42** shows the conversion results of using various co-relations. PETEX-2 correlation was chosen for the conversion. Apart from these two parameters, sensitivity using different water injection temperatures was also checked, but it had no effect on the conversion. Water injection temperature was taken as 60°F.

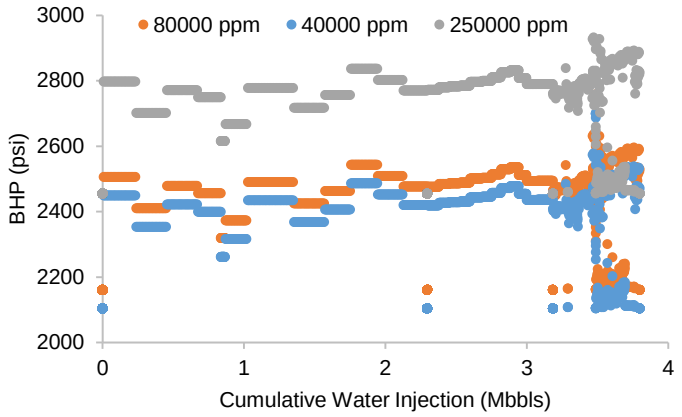

Figure 41. Effect of salinity for pressure conversion – Well E

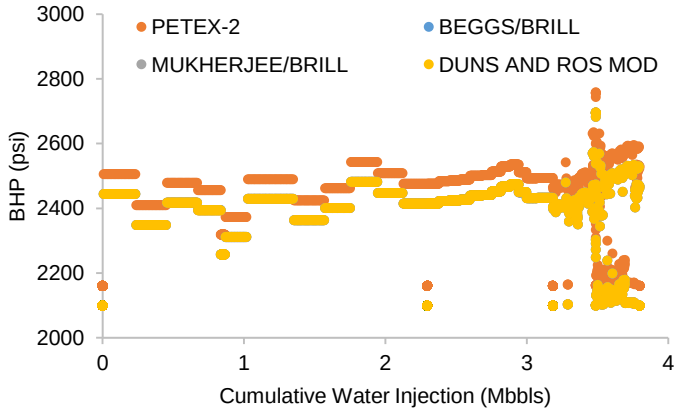

Figure 42. Effect of using various flow co-relations for pressure conversion – Well E

3.5.3. Flow Regime Identification

Ascertaining the onset of the steady-state flow regime allows identifying the appropriate range for pressure and injection data to be used in the modified-Hall analysis (MHA). I will be using MHA for understanding injection well behavior. The flow regimes were identified using material-balance time diagnostics plots (Anderson and Mattar, 2004). Material balance time is defined as the ratio of

cumulative injection and daily injection rate. In this technique, the daily injection rate is plotted against the material-balance time on a log-log plot. The steady-state regime is represented as unit slope in the resulting log-log plot.

Figure 43 shows the material balance time plot of the (Well E). The transient state and the steady state flow are identified in the plot.

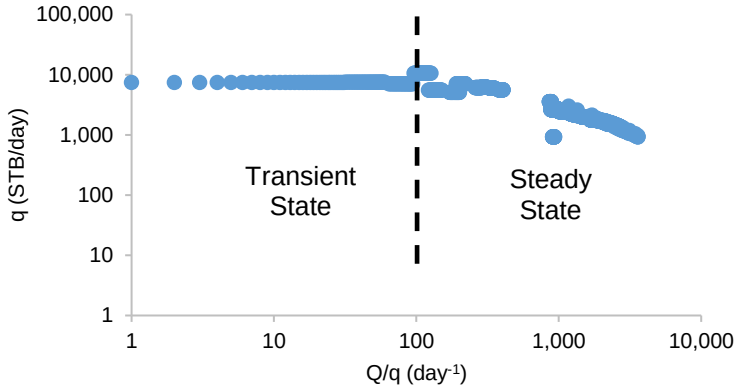

Figure 43. Material-balance-time diagnostics plot (Well E) for flow regime identification

3.5.4. Estimation of Ambient Reservoir Pressure

I used Silin slope analysis (Silin et al., 2005) to calculate the ambient reservoir pressure. The reservoir pressure at virgin conditions is termed as ambient reservoir pressure. Note Silin analysis can only provide an approximate characterization of the virgin pressure. In the absence of any other relevant techniques, this is a viable means to determine the ambient reservoir pressure. Silin devised the following equation for the slope analysis:

$$\frac{p_w}{q} = \frac{p_e}{q} + b. \qquad (13)$$

In Silin plot, the ratio of pressure and injection rate (p_w/q) is plotted against the inverse of injection rate ($1/q$). The injectivity parameter (b) does not change since it is assumed that the formation properties remain constant. The slope of this plot will give the ambient reservoir pressure (p_e). It is to be noted that Silin analysis should only be applied to injection data from transient flow regime. Late-time or pseudo-steady state pressure and rate data will influence the estimated virgin pressure. **Figure 44** shows the Silin slope plot for Well E.

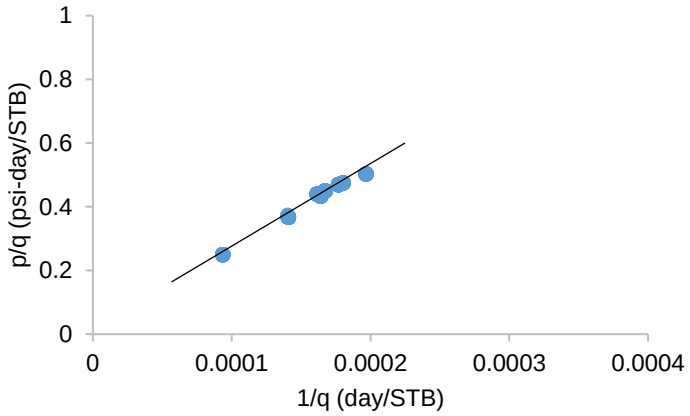

Figure 44. Estimating ambient reservoir pressure using Silin slope plot (Well E)

A straight line is fitted that would cover the maximum points on the plot and the slope of that line will give an estimate of ambient reservoir pressure. The slope of the line is found to be 2,350 psi, which will be the ambient reservoir pressure for this well. **Figure 45** presents the ambient reservoir pressure for all 29 wells calculated using the Silin slope analysis. The pressure values are presented in Appendix-I.

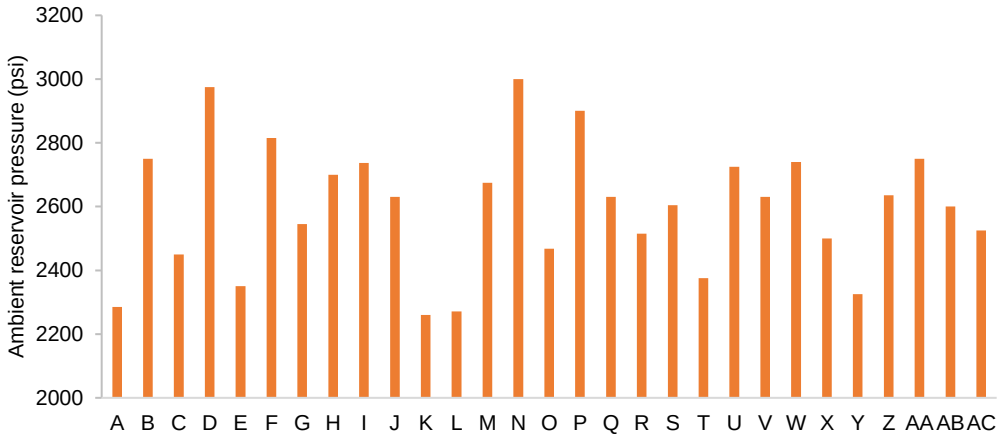

Figure 45. Ambient reservoir pressure of 29 wells estimated using Silin slope analysis

3.5.5. Modified Hall Analysis

Modified Hall Analysis (MHA) was carried out to understand the injection behavior of the wells. In MHA, Hall integrals and their derivatives (modified Hall derivatives) with respect to cumulative injection (Izgec and Kabir, 2011) are plotted against the cumulative injection. Hall integrals are calculated by:

$$I_H^n = \int_0^{t^n} (p_w - p_e)dt, \tag{14}$$

and the derivative term is calculated by:

$$D_{HI}^n = \frac{I_H^{n+1} - I_H^n}{ln(Q_i)^{n+1} - ln(Q_i)^n}. \tag{15}$$

Hall integral can be considered as a measure of injection-pressure buildup with time and the modified Hall derivatives indicate the rate of pressure buildup with incremental injection. In a normal injection scenario, both curves (Hall integrals and the modified Hall derivatives) will have similar slope against

cumulative injection. Whenever the two curves deviate away from each other, normal injection ceases. If the slope of the Hall derivatives increases faster than the Hall integral, this implies the well is struggling to inject fluid causing the pressure to build up rapidly. This is an injectivity-loss scenario for instance formation plugging and any other kind of formation damage. Whereas, if the slope of the Hall derivatives declines rapidly compared to the Hall integrals, this implies the injected fluid has found less resistant flow path and the pressure is not building up any further. In fact, the disposal well may experience pressure decline at this point. This is a typical disposal well pressure behavior after formation-fracturing has taken place.

Figure 46 shows the modified Hall analysis carried out on the Well E. As can be seen in the figure, the Hall derivatives increase faster than the Hall integral, after a certain point. It indicates normal injection up to the point it starts getting separated. And after that it can be inferred that the well is struggling to inject fluid causing the pressure to build up rapidly.

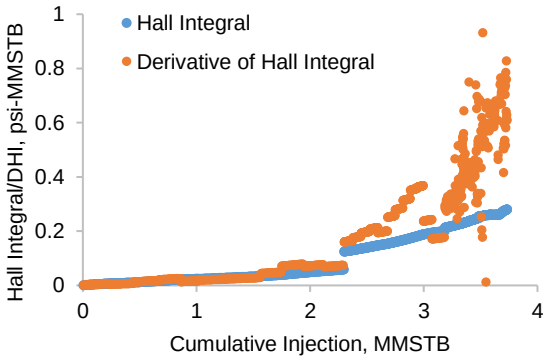

Figure 46. Modified Hall plot analysis (Well E) for understanding injection well behavior

The modified-Hall plots for all 29 wells are presented in Appendix-II.

3.6. Correlating Seismicity with Injection Data

I carried out a quick analysis to link the seismic events with various injection-related parameters. Four parameters: Peak injection rate, cumulative injected volume, peak wellhead pressure and ambient reservoir pressure calculated using Silin analysis were taken into consideration for this analysis. With this analysis, I identified regions and wells sensitive to the injection activity.

3.6.1. Peak Injection Rate

Peak injection rates for all the 29 wells under the study are presented in **Figure 47**. In **Figure 48**, each of the wells is represented by bubbles, with the size of the bubble representing the peak injection rate relative to other wells. The colors of bubble represent the year in which the peak injection rate occurred, which can be correlated with the base map where seismic events are represented color coded according to the year in which the event took place. The histogram of the peak injection rate values is presented in **Figure 49**.

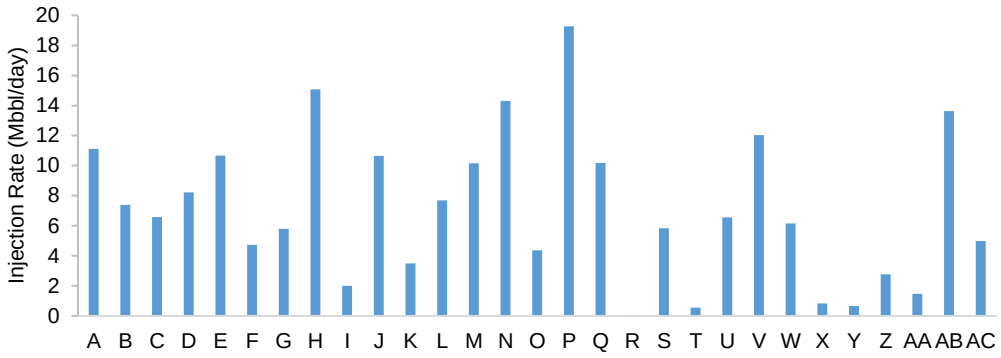

Figure 47. Peak injection rate for all 29 wells

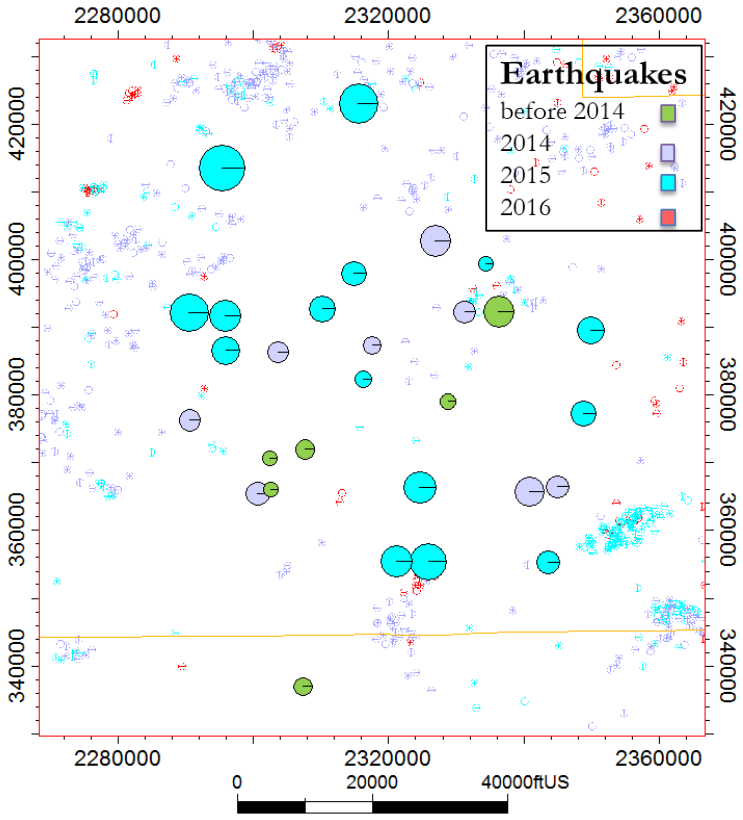

Figure 48. Peak injection rate tied with seismicity mapped year-wise

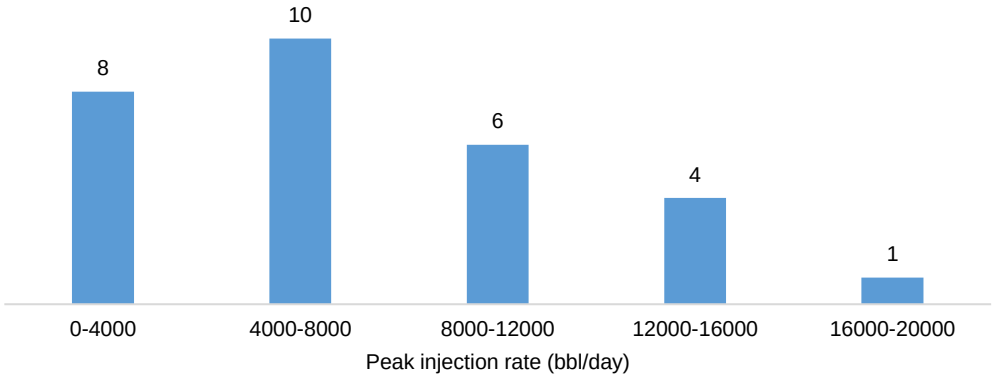

Figure 49. Histogram of peak injection rate for 29 wells

3.6.2. Cumulative Injected Volume

Cumulative injection volumes for all the 29 wells under the study are presented in **Figure 50**. In **Figure 51**, each of the wells is represented by bubbles, with the size of the bubble representing the amount of cumulative injected volume relative to other wells. In the base map seismic events are represented, and are color-coded according to the year in which the event took place.

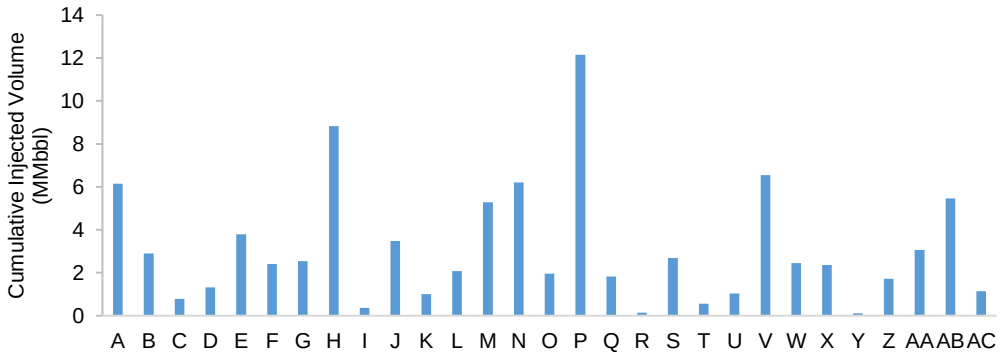

Figure 50. Cumulative injection volume for all 29 wells

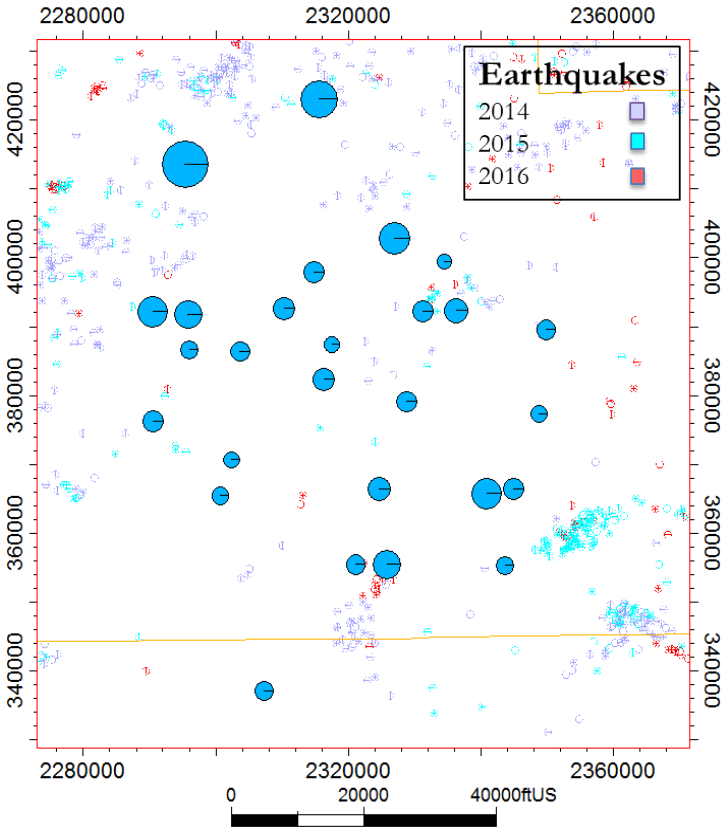

Figure 51. Cumulative injection volume tied with seismicity mapped year-wise

3.6.3. Peak Wellhead Pressure

Peak wellhead pressures for all the 29 wells under the study are presented in **Figure 52**. In **Figure 53**, each of the wells is represented by bubbles, with size of the bubble representing the wellhead pressure relative to other wells. The colors of bubble represent the year in which the peak wellhead pressure occurred, which can be correlated with the base map where seismic events are represented color coded according to the year in which the event took place. The histogram of the peak wellhead pressure values is presented in **Figure 54**.

Figure 52. Peak wellhead pressure for all 29 wells

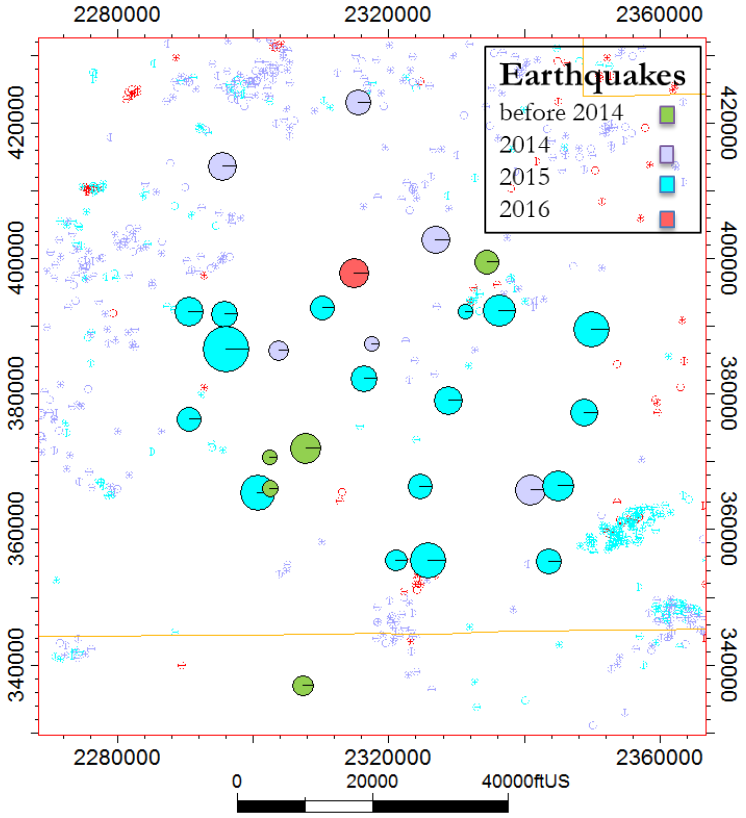

Figure 53. Peak wellhead pressure tied with seismicity mapped year-wise

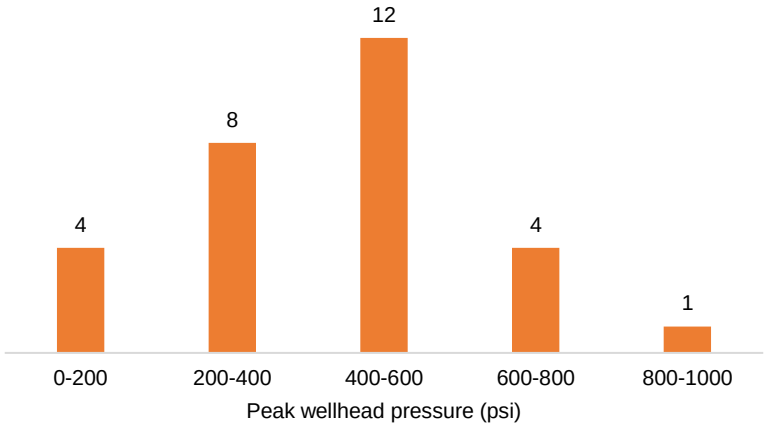

Figure 54. Histogram of peak wellhead pressure for 29 wells

3.6.4. Ambient Reservoir Pressure

Ambient reservoir pressures calculated using Silin slope analysis for all the 29 wells under the study are presented in **Figure 55** (same as Figure 45). In **Figure 56**, each of the wells is represented by bubbles, with the size of the bubble representing the magnitude of the ambient reservoir pressure relative to other wells. In the base map seismic events are represented, and are color-coded according to the year in which the event took place. The histogram of the ambient reservoir pressure values is presented in **Figure 57**.

Figure 55. Ambient reservoir pressure for all 29 wells

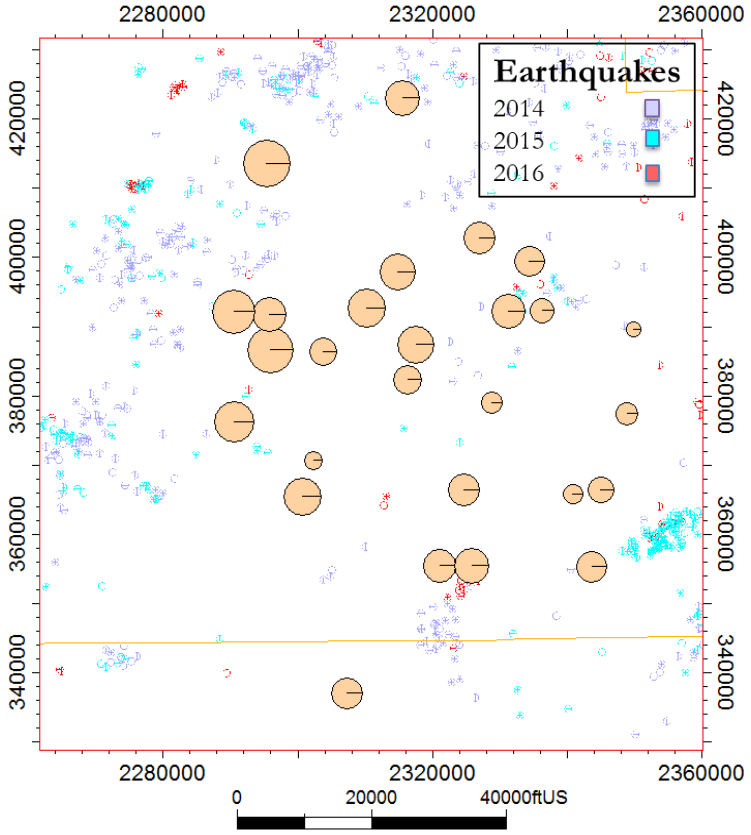

Figure 56. Ambient reservoir pressure tied with seismicity mapped year-wise

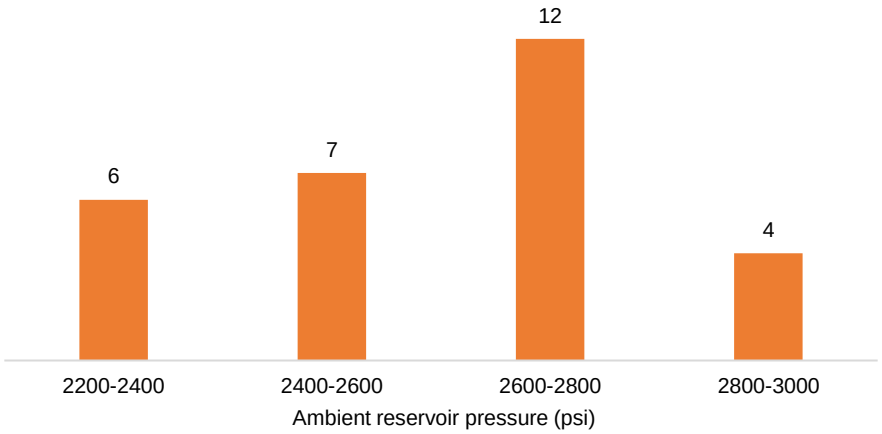

Figure 57. Histogram of ambient reservoir pressure for 29 wells

To summarize, I attempted to tie the peak injection rate, cumulative injected volumes, peak wellhead pressure and the estimated ambient reservoir pressure with the seismicity events shown on maps (Figures 48, 51, 53 and 56, respectively). A proper causality analysis using these records is beyond the scope of this study. Nonetheless using this analysis, I could identify key wells based on the cumulative injected volumes map that warrant further investigation.

In this chapter, I studied various available datasets. At first, I looked at the seismicity map where the seismic events in the study area were marked along with the location of the wells. Then, I focused on understanding the acquisition of the core data and its results. Thereafter, the injection data was analyzed in detail. Using this data, well behavior of all 29 wells was learned using modified-Hall analysis (MHA). Identification of the flow regime and estimation of ambient reservoir pressure was required for MHA. At last, various injection parameters were linked with the seismicity, to understand their impact. In the next chapter I will use these

datasets and learnings, to develop a simulation model for history matching and study its results.

Chapter 4: Characterizing Arbuckle Group

In this chapter, an overview of creating static model is provided by using the data and analysis discussed in Chapter 3. This model was prepared by the geology experts in the project team. Using this model, I constructed a simulation model for history matching. The description is provided in the methodology section. The injection pressures and rates are matched in order to characterize the Arbuckle-Group Formation. The outcomes and learnings of the history matching are presented in the results section.

4.1. Static Model

4.1.1. 3D Geocellular Model Construction

Structure-contour maps are used to create a 3D stratigraphic and structural framework of the study area. Fault surfaces from the interpreted faults from the 3D seismic data are included in the 3D grid. Also, the fault surfaces are subsequently used to map porosity trends within the Arbuckle-basement interval and are also included in the fluid-flow simulation for calibration as either conduits or barriers to flow. I included the basement in the 3D grid as a 500 ft thick interval (reservoir model zone) below the Arbuckle Group. The Arbuckle Group, as well as the Simpson and Viola formations (not mapped using the seismic data) are included in the grid based on surfaces that represent each formation. The 3D grid consists of grid cells with aerial cell dimensions of 500 ft by 500 ft and an average layer thickness of 10.5 ft. The 3D stratigraphic framework (3D grid), well logs, and variogram parameters are used to constrain 3D models of porosity and

permeability. A three-dimensional lithology or “rock type” model could not be accurately constructed to constrain the porosity and permeability models because of limited well and core data.

I used a simple proportional layering scheme, given the absence of seismic control above the top Arbuckle Formation, resulting in a grid containing approximately 6.5 million cells. Error! Reference source not found. shows the r esulting stratigraphic zones from the basement interval to the top of the Viola limestone formation.

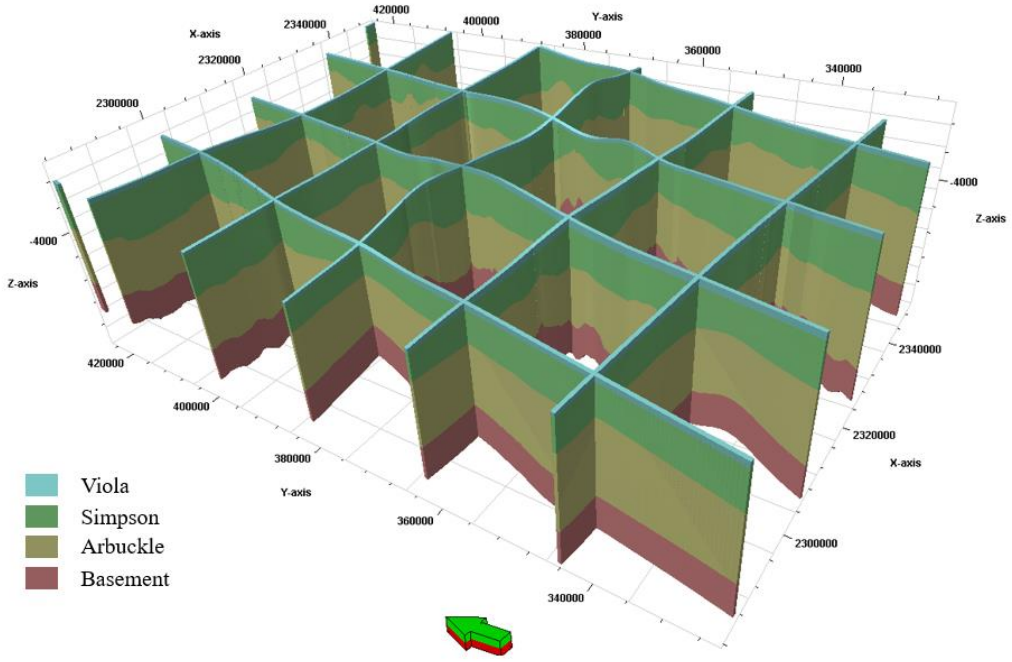

Figure 58. Stratigraphic framework (3D grid). A proportional layering scheme is used, and the resulting grid contains approximately 6.5 million cells. The 3D grid consists of cells with aerial dimensions of 500 ft. by 500 ft. and an average layer thickness of 10.

4.1.2. Porosity Model

Three-dimensional porosity models are generated and constrained to upscaled total porosity logs (based on neutron and density porosity logs) and porosity variogram parameters. Core data do not exist within the study area. I calculated the total porosity logs (ϕ_t) using the root-mean-square method with the NPHI and DPHI curves. The total porosity logs are upscaled to the grid and modeled using variogram-based sequential-Gaussian simulation (SGS). For the Arbuckle Group and shallower formations, the variogram ranges were set to 7,000 ft. (2,134 m) for both horizontal directions and 10 ft. (0.6 m) for the vertical direction. Due to lack of well-log data for the basement, the porosity distribution in the basement was modeled assuming that the porosity, in general, is greater near the faults and essentially zero in non-faulted areas (for igneous and metamorphic lithologies). This porosity distribution was computed using a "distance-to-object" property using commercial software in which the interpreted fault surfaces are the objects. This approach resulted in porosity values of 6% near fault surfaces and linearly decreasing to zero roughly 3,000 ft. away from the fault.

Porosity values in the basement range from 0 - 6%, and log-derived porosity values in the Arbuckle Group range from 5 - 10% (Error! Reference source not f ound.).

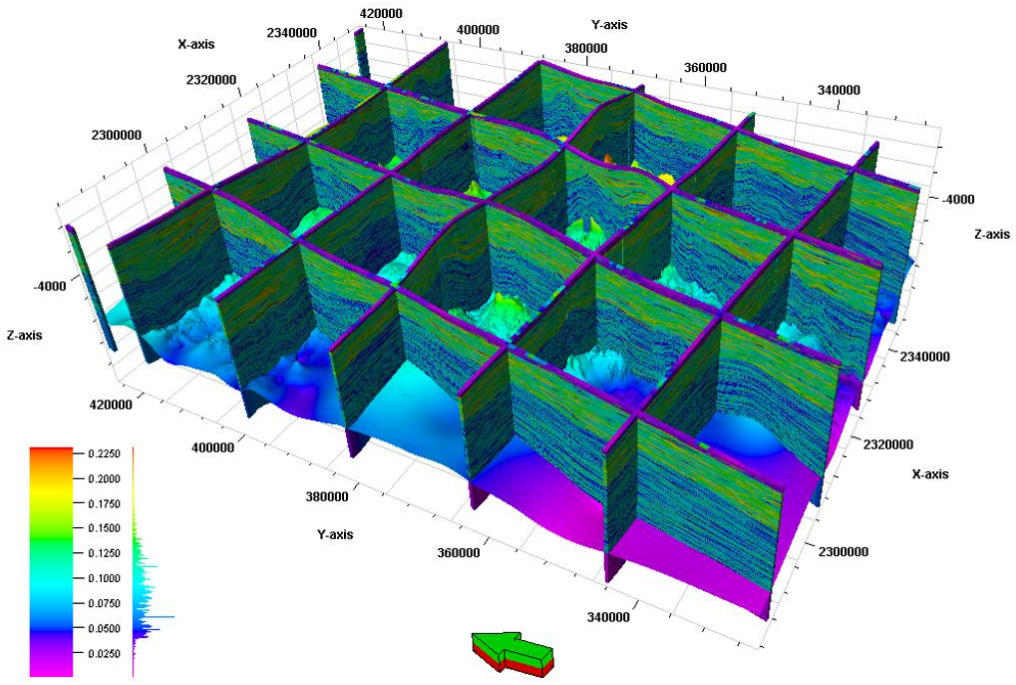

Figure 59. Porosity model of the basement through Viola intervals.

4.1.3. Permeability Model

Three-dimensional permeability models are generated and constrained to the 3D porosity model and a Buckle's (Schlumberger, 1989) relationship between calculated irreducible water saturation and porosity. Buckle's method estimates the irreducible water saturation, Sw_{irr}, using an empirical relationship between the effective porosity, φ_e, the fractional volume of shale, V_{sh}, and the Buckle's number κ_{Buckle}:

$$Sw_{irr} = \frac{\kappa_{BUCKL}}{\varphi_e(1-V_{sh})}. \tag{16}$$

V_{sh} is commonly calculated using the gamma-ray log. In this case, V_{sh} is set to be identically zero to assume only the presence of water. After irreducible water

saturation is estimated, qualitative permeability estimates are calculated using two different equations:

the Tixier Equation

$$\kappa = \left(250 \frac{\varphi_e^3}{Sw_{irr}} \right)^2 , \tag{17}$$

and the Timur Equation (Schlumberger, 1991),

$$\kappa = \left(100 \frac{\varphi_e^{2.25}}{Sw_{irr}} \right)^2 , \tag{18}$$

which are a function of the irreducible water saturation and the total porosity model. Three iterations of this process using equations 2 and 3 are run using $\kappa_{BUCKL} = 0.01$ for vuggy, $\kappa_{BUCKL} = 0.005$ for crystalline, and $\kappa_{BUCKL} = 0.001$ for fractured, corresponding to rock matrix types I ran another six models assuming 100% water saturation and no presence of hydrocarbons. A vuggy to fine vuggy matrix is assumed for the Arbuckle Group.

Permeability values associated with the Arbuckle Group range from 1-5 mD whereas the highest permeabilities are associated with faults interpreted from the seismic that penetrate the basement and Arbuckle zones. These faulted zones range from 10 – 100 mD (Error! Reference source not found.).

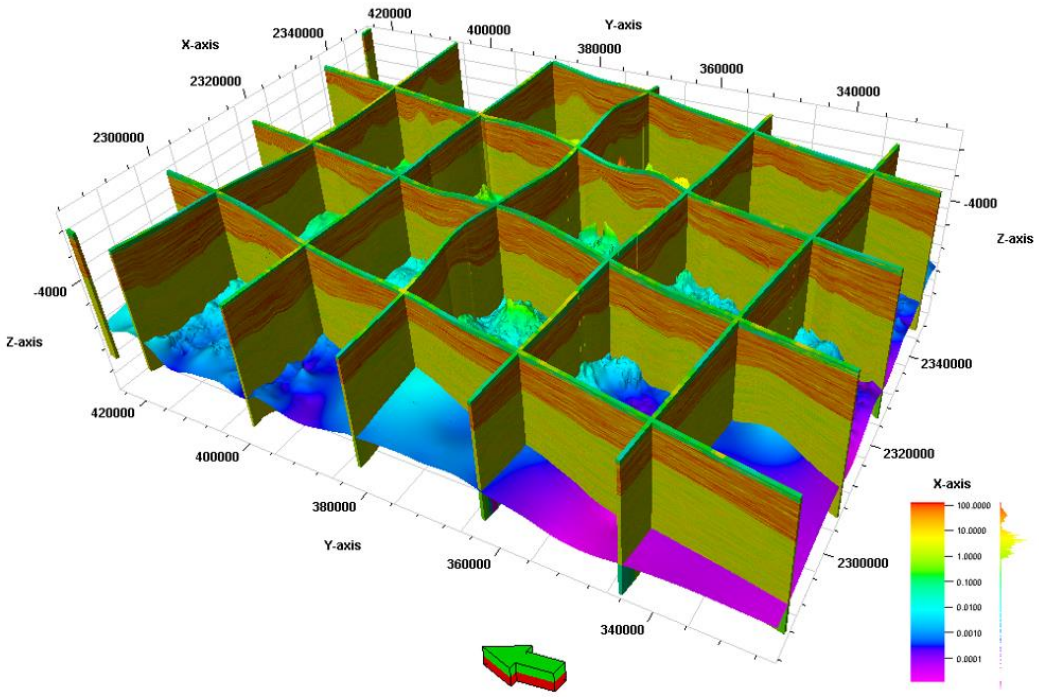

Figure 60. Permeability model of the basement through Viola intervals.

4.2. History Matching Methodology

In this section I present the procedure that is followed for history matching. Initially, the model construction for fluid flow simulation is explained. Then, the parameters selection process and methodology for the history matching process are described.

I considered Viola, Simpson, Arbuckle Group and basement Formations to be potential flow units from the geological model. The model is discretized using 500 ft. by 500 ft. grid cells, 164 grid points in the x (North), 217 grid points in y (East), and 185 grid points in z (vertical) directions, giving a model that extended

laterally approximately 66,500 ft. x 98,300 ft. Schematic of the simulation model is presented in **Figure 61**.

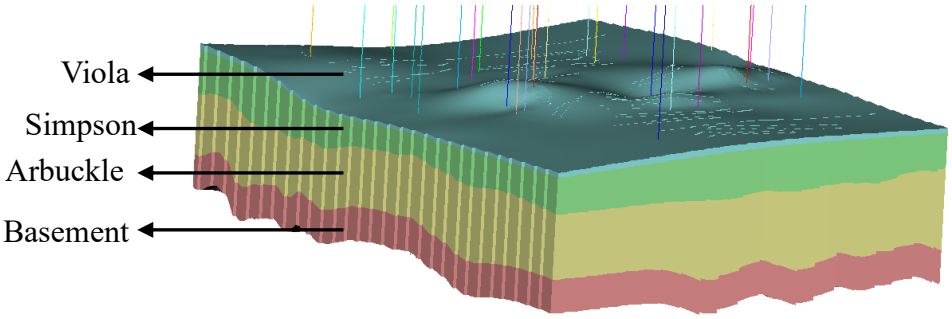

Figure 61. Simulation model schematic

Geological porosity and permeability parameters, as described in the Static Model section, are assigned to the simulation model. Rock properties are considered based on the type of the formation. I have considered the Arbuckle Group and the basement formations to be water filled as fluid distribution, as most of the injection takes place in these formations. I modeled completions of all 29 wells according to the available completion reports. Injection rates and pressures are assigned to the respective wells for the period between January 2005 to May 2016. Faults interpreted using the seismic model are also included in this simulation model.

I will now describe the history matching process followed in this study. At first, a region of interest for history-matching needs to be identified. Arbuckle-Group formation is the zone of interest for our study. History-matching can be carried out by automated process or by manual analysis. In this study, I opted for manual process. In general, the quality of results is better using the manual process.

Thereafter, it is required to recognize the variables of interest for which the matching will be carried out. I identified bottom-hole pressure and injection rate as the variables of interest.

The next step would be to identify uncertain parameters for history matching. I identified uncertain parameters to be permeability, horizontal and vertical anisotropy, porosity and compressibility of all Viola, Simpson, Arbuckle-Group and basement formations. As well as, formation water properties such as compressibility, viscosity, density and formation volume factor. For injection well each well, productivity multipliers (PI) are taken into consideration as uncertain parameters. The values of these parameters were not known, and thus were included in uncertainty characterization. In the beginning, reasonable values with a slightly broader range are selected for the all the parameters.

At each stage of history matching, I performed screening analysis, where the parameters which impacted the response variables the most were identified using Pareto plots. These parameters were mostly linked with key formations and wells identifies in previous analysis. And based on their impact, the ranges of the values were selected for the next stage of history matching, where again uncertainty characterization was carried out. This process is carried out till I got optimized match of the variables of interest.

As I mentioned earlier, injection rates and bottom-hole pressures are matched for calibration of the model. The bottom-hole pressures in this study are not available directly and are obtained from wellhead pressures using the pressure conversion process as described in section 3.5.2. More emphasis is given to the

wells with high cumulative injection volumes for the matching process. The results and analysis are presented in the next section.

4.3. History Matching Results

The simulation model is calibrated by the observed and measured injection data. Initially, around 50 parameters are varied through sensitivity runs. The impactful parameters based on history matching include permeability, horizontal and vertical anisotropy and porosity of Arbuckle-Group, permeability and horizontal anisotropy of overlying Simpson and underlying basement formations, formation water density and viscosity, and productivity multipliers (PI) of the key injection wells. These parameters were identified using Pareto plots. This can be explained as most of the injection takes place in the Arbuckle formation, and a few fault planes laying in the Arbuckle Group formation penetrate Simpson and basement formation. For this reason, the petrophysical properties of Arbuckle Group, Simpson and basement would be most impactful. Other than those, I identified key wells based on the amount of cumulative volumes. PI multipliers of those wells being identified as impactful parameters also can be explained.

The least impactful parameters were identified to be the parameters of the Viola formation and PI multipliers of some least important wells. There is limited pathway for the injection fluids to reach the Viola formation. And the least important wells are the wells in which the cumulative injection is less. Thus, the least impactful parameters can be explained.

I carried out multiple stages of history matching reasonable matches for the identified key wells are obtained. The injection rate match of all the wells was of high quality. An aerial view of the wells showing the bottom-hole pressure match is presented in **Figure 62**. The color coding is based on the percent mismatch calculation. Injection data for Wells K, O, R, X, Y, and AA are of limited reliability. These wells are color-coded in Grey color. Green color indicates that the pressure mismatch is within 10%, the yellow color is for the mismatch between 10% and 50% and red color shows the mismatch is greater than 50%.

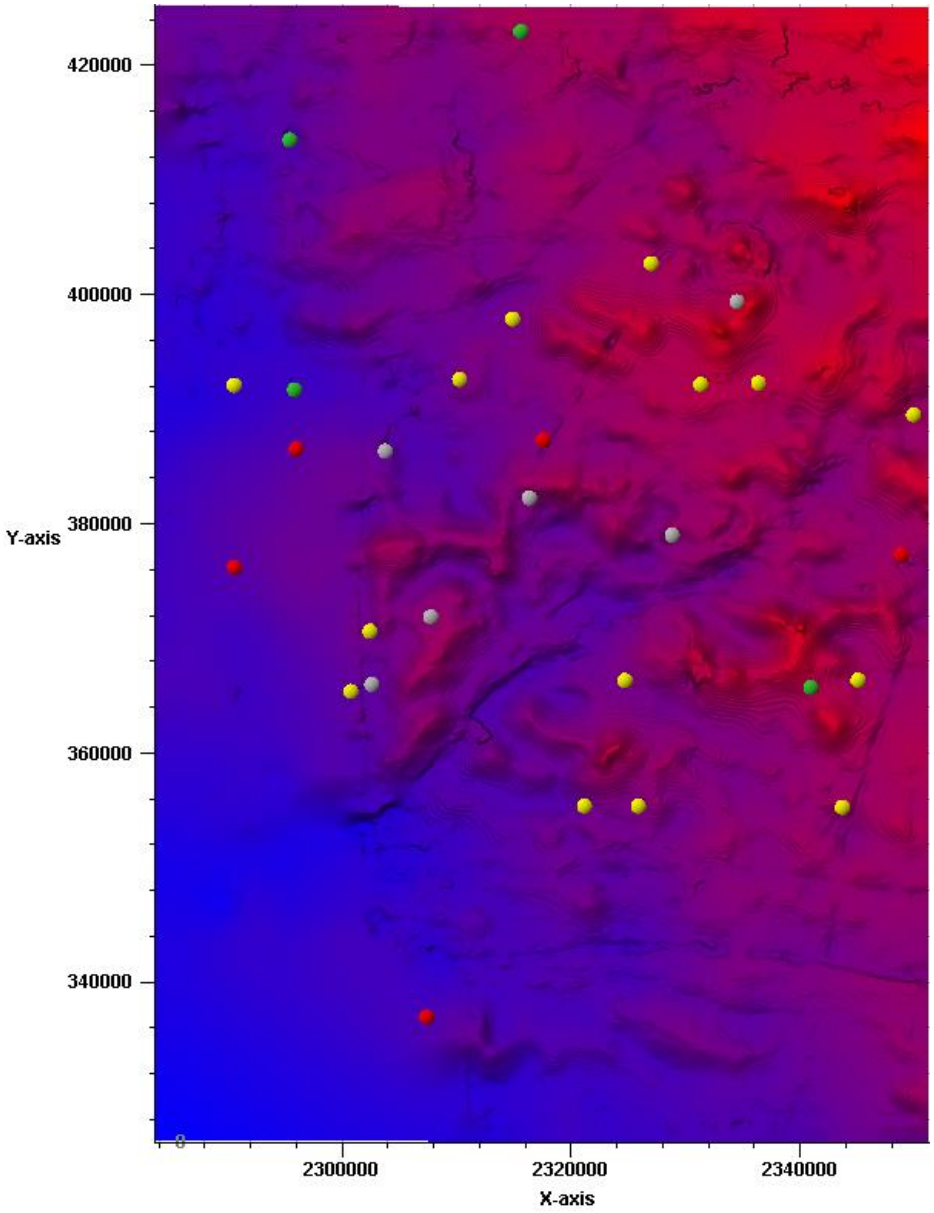

Figure 62. Bottom-hole pressure history-match results
Color according to mismatch as following: Grey – Inconsistent data, Green – within 10%, Yellow – within 50% and Red – Greater than 50%. Results are mapped on the horizon of Top of Arbuckle-Group formation

23 wells out of 29 wells have reliable data. 4 wells out of 23 wells have mismatch less than 10%, considering them as a good quality match. 14 wells have a mismatch between 10% and 50%, and shall be considered as a decent quality

match. Rest of the wells have mismatch greater than 50%, and are considered a poor quality match. The pressure build-up for these wells was not sufficient. The bottom-hole pressure and injection rate data matching for four wells, are presented here. Well H and Well A show good quality match. **Figures 62** and **63** present the bottom-hole pressure and injection rate match, respectively, for Well H. While **Figures 64** and **65** show the same matches for Well A. Well E and Well AB show decent quality match. **Figures 66** and **67** present the bottom-hole pressure and injection rate match, respectively, for Well E. **Figures 68** and **69** show the same for Well AB.

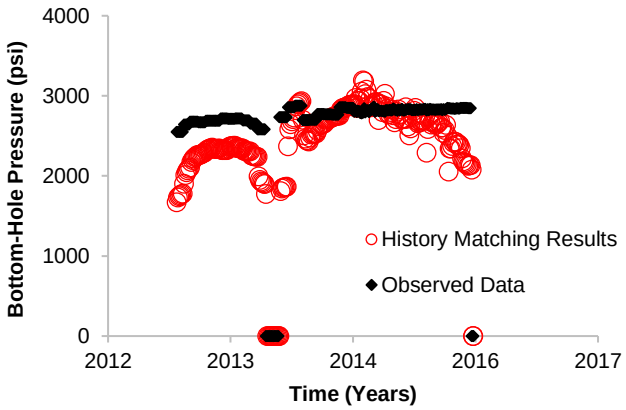

Figure 63. Bottomhole Pressure Matching for Well H showing good quality match

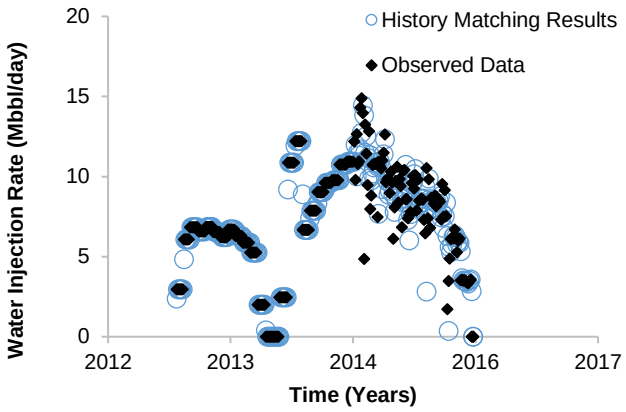

Figure 64. Injection Rate Matching for Well H showing good quality match

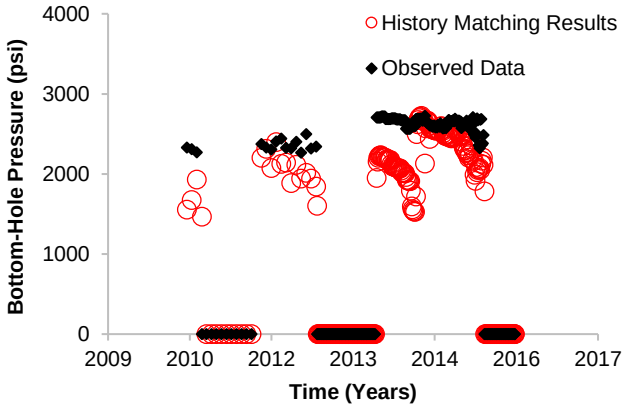

Figure 65. Bottomhole Pressure Matching for Well A showing good quality match

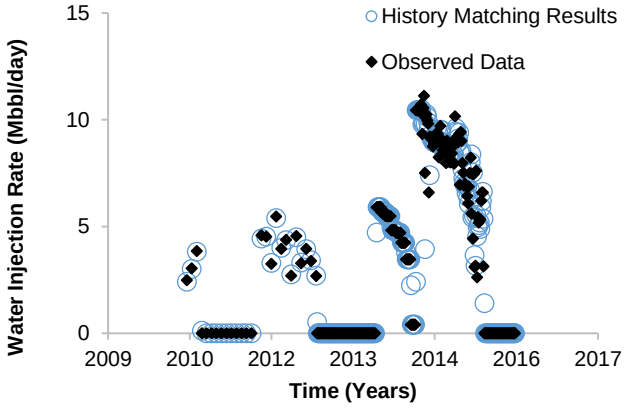

Figure 66. Injection Rate Matching for Well A showing good quality match

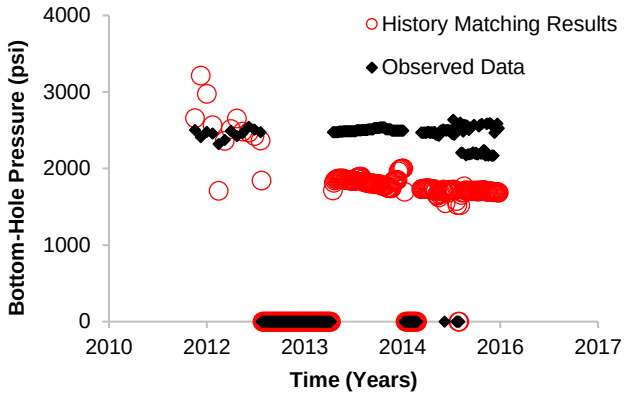

Figure 67. Bottomhole Pressure Matching for Well E showing decent quality match

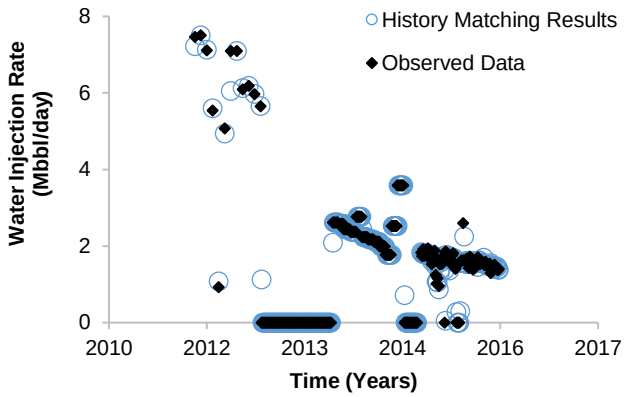

Figure 68. Injection Rate Matching for Well E showing decent quality match

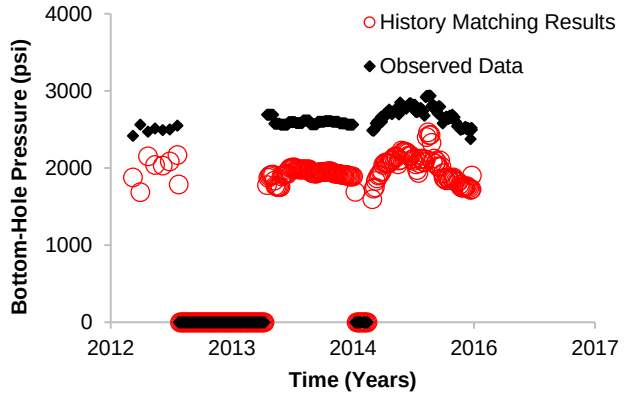

Figure 69. Bottomhole Pressure Matching for Well AB showing decent quality match

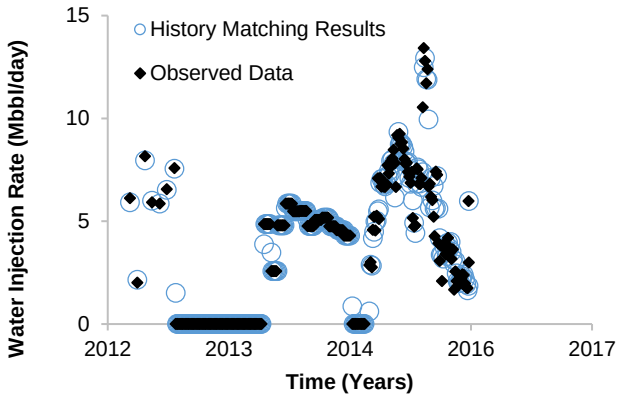

Figure 70. Injection Rate Matching for Well AB showing decent quality match

Based on the current history-match results, the porosity and permeability distribution of Arbuckle-Group and Simpson are presented here. **Table 7** and **Table 8** present the minimum, maximum, and average porosity and permeability results respectively for Arbuckle-Group and Simpson formations.

Table 7. Minimum, maximum and average ϕ values for Arbuckle and Simpson formations based on current history matching results

Formation	ϕ, min	ϕ, max	ϕ, avg
Arbuckle-Group	3%	15%	7%
Simpson	2%	22%	12%

Table 8. Minimum, maximum and average *k* values for Arbuckle and Simpson formations based on current history matching results

Formation	k, min	k, max	k, avg
Arbuckle-Group	1 mD	40 mD	10 mD
Simpson	1 mD	130 mD	40 mD

The history-matching process revealed evidence of fault effect on the performance of some of the disposal wells in the Arbuckle-Group. It is conjectured some of the faults may be acting as sealing fault while others as conduit. However, in order to conclusively verify the hypothesis further investigation will be required. This will not be undertaken in this study. Based on the current history-match results, a couple of hypotheses are presented here (refer **Figure 71)**:

- The wells around the faults marked as F1 to F4 presents insufficient pressure build-up due to injection. I hypothesize these faults to be sealing in nature.
- Seismic survey was not available in the shaded area marked as R1, therefore, it was not possible to identify faults in this region. History-match results for a couple of wells under this area indicate the possibility of some sealing faults nearby.

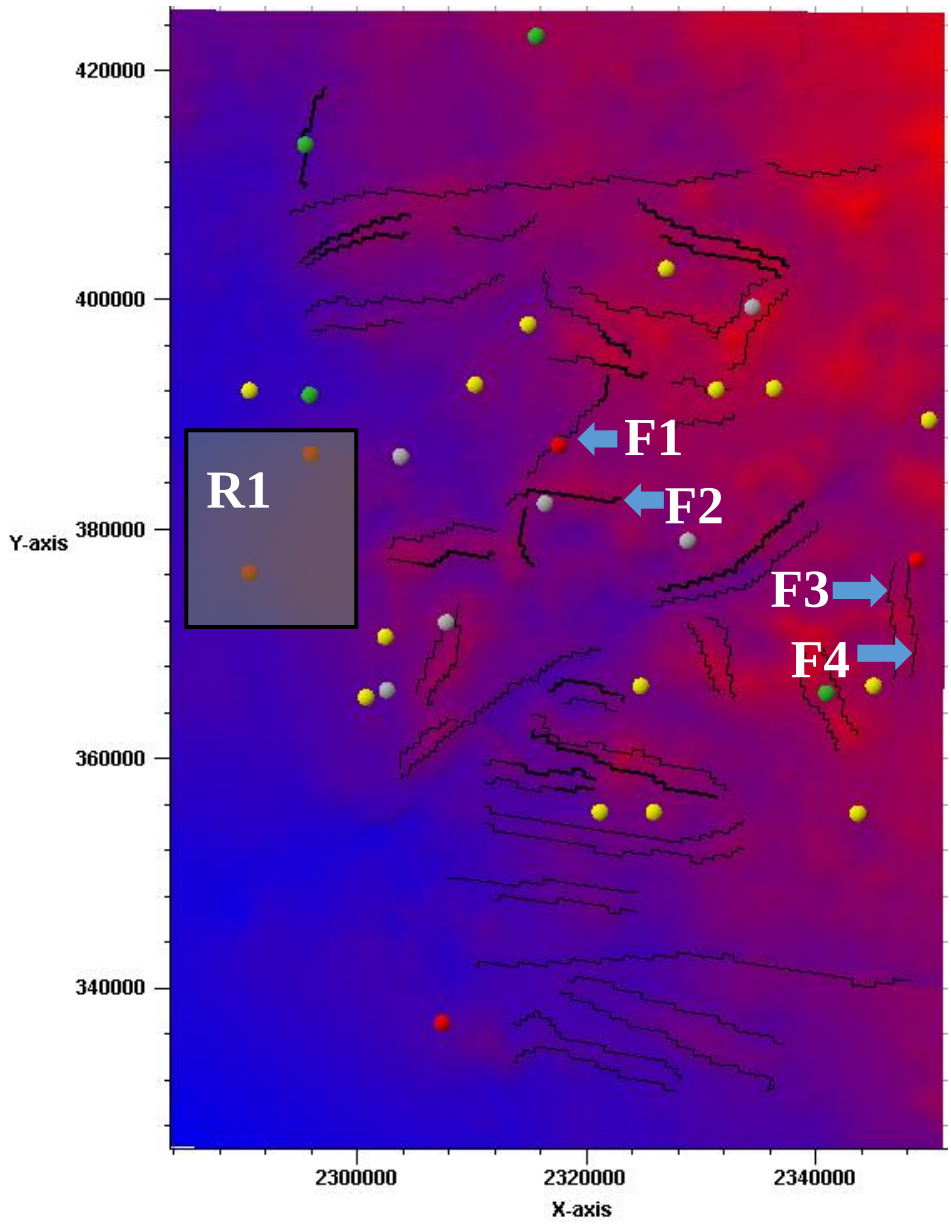

Figure 71. Effect of faults in history-match, interpreted fault planes are presented, also shown are wells color coded according to the quality of pressure match, mapped on horizon of top of Arbuckle-Group

I carried out multiple stages of history matching to achieve these results. Average porosity of the Arbuckle-Group is found to be around 7% and permeability is found to be around 10 mD. I observed that a slight lateral permeability anisotropy

of 1.25 towards the Northing direction with respect to the Easting direction in the Arbuckle-Group. This may be attributed to the nature of faults. I also observed a vertical to lateral permeability anisotropy (k_v/k_h) of 0.01. All these observations are based on the current history matching results. Scenarios with varying fault behavior and considering different fluid distribution would led more complete characterization. Thus, there is a scope to improve matches by carrying out few more stages of history matching.

In this chapter, I explained the construction of the simulation model for the study area using the available data. The methodology of history matching was described, and the analysis and results were presented. Based on the available history-match results, the characterization of the Arbuckle-Group formation is presented.

Chapter 5: Safe Water Disposal Operation

As I discussed earlier in Chapter 1, state and federal governments are looking for operational guidance towards reducing the risk of induced seismicity. Oklahoma Corporation Commission (OCC) (Baker 2016) issued a regulatory notice to all the operators related to be followed for wastewater disposal. Few additional steps learned from this chapter may help in further reduction of the seismic activities.

In this chapter, the wastewater-disposal process is explored in detail by studying various scenarios. Modified-Hall analysis (Izgec and Kabir 2009, 2011) and rate transient analysis methods are used for real-time monitoring of the wastewater-disposal operations. The onset of the abnormal behavior is detected using modified-Hall analysis and the cumulative injection at that point becomes the monitoring variable of interest. The behavior of cumulative injection with high impact variables, such as compartment size and the limiting fracture gradient are studied. At the end, an overall strategy that can provide operational guidance for safe wastewater disposal is established. This work was presented at the 2017 SPE Annual Technical Conference and Exhibition and is selected for publication in the SPE Reservoir Engineering and Evaluation journal (Gogri et al, 2017).

5.1. Literature Review

The seismic risks are not unique to wastewater disposal. Injection of carbon dioxide (CO_2) for both enhanced recovery operations and dedicated storage has triggered many seismic events in the USA, as discussed by White and Foxall

(2016). In a preceding study, Pawar et al. (2015) detailed both risk assessment and risk management of geologic storage of CO_2. While correlating induced seismicity and wastewater injection, Gono et al. (2015) reported that there exists a spatial and temporal correlation between seismic activity and pore pressure change during wastewater injection. They also suggested that preexisting faults appear necessary to trigger seismic events. In a more recent study, Abrahams et al. (2017) reported the impact of physical controls linked to fluid injection on statistical properties of injection-induced earthquake sequences.

Given the interest in reducing the emission of greenhouse gas, a plethora of studies have appeared for sequestering CO_2 over the last 10 years or so. Whereas safe disposal can occur in depleted hydrocarbon reservoirs, injection of CO_2 in saline formations presents challenges that are comparable to that of wastewater disposal. It should be noted that because the density of supercritical CO_2 (approximately over 0.8 g/cm^3) is comparable to that of water, the injection behavior is expected to be similar to that of water injection. Flow simulation studies involving both small-scale (Anchliya et al., 2012; Chasset et al., 2011; and Kumar et al., 2005; among others) and large-scale (Person et al., 2010; Yamamoto et al., 2009; among others) reservoirs reveal many insights into the feasibility of the sequestration process. More recently, the insightful study of Akinnikawe and Ehlig-Economides (2016) suggested that the Woodbine aquifer in East Texas can store CO_2 for 240 years with appropriate aquifer management strategy. On the wastewater-disposal front, Saripalli et al. (2000) presented a simulator to study the impact of several pertinent formations and operational characteristics on injection

decline. They attributed the decline in injectivity to high total-suspended-solids concentration in the waste stream, low injection rate, low injection pressures, formation heterogeneity, low porosity and low permeability.

Lessons learned from CO_2 injection and wastewater disposal of late suggest that well monitoring and analysis of surveillance data become a cornerstone for any disposal project. Therefore, understanding the process of disposal and the factors affecting injection becomes imperative. Also, in water flooding, CO_2 sequestration (Ehlig-Economides and Economides 2010, Aschehoug and Kabir 2013) and other injection-related EOR, the size of compartment plays an important role. Consequently, a large impact of compartment size in wastewater disposal operations is expected. In addition, operating limits will play a significant role because it is intrinsically tied to the fracture gradient.

5.2. Water-Disposal Well-Performance Workflow and its Application

Arbuckle Group in Oklahoma has been the primary focus of this study, as the amount of wastewater disposal in this formation is large. Hence, Arbuckle-specific well and formation data is used in the study. As reported by Murray (2015), in the year 2014, 25% of the injection wells in Oklahoma penetrated Arbuckle Group and that accounted for 75% of the total wastewater.

Understanding the disposal-zone reservoir dynamics under various conditions is important to identify and implement safe water-disposal operations. A workflow to investigate the water-disposal process is presented. A 3D reservoir model as shown in **Figure 72** is constructed, which contains a disposal and a

producing zone separated by a seal. **Figure 73** shows the schematic of the workflow. Second, fluid and petrophysical properties are assigned for each zone in accord with the open-hole logs, core, and relevant information from the available literature. Subsequently, an injection well for disposal zone and a production well for connected production zone is designed and completed. The well operational conditions are set via allocation of injection and production rates with appropriate bottomhole-pressure limits. The disposal zone is considered to be an aquifer containing saline water. The initial pressure in this zone is based on the hydrostatic head corresponding to the water. It has no-flow boundaries on the sides and at the bottom and is underlain by the seal. The integrity of the seal has been used as an uncertain variable through the vertical transmissibility of the seal. The overlying producing zone is initially filled with hydrocarbon and water with a water/oil contact specified within the producing zone.

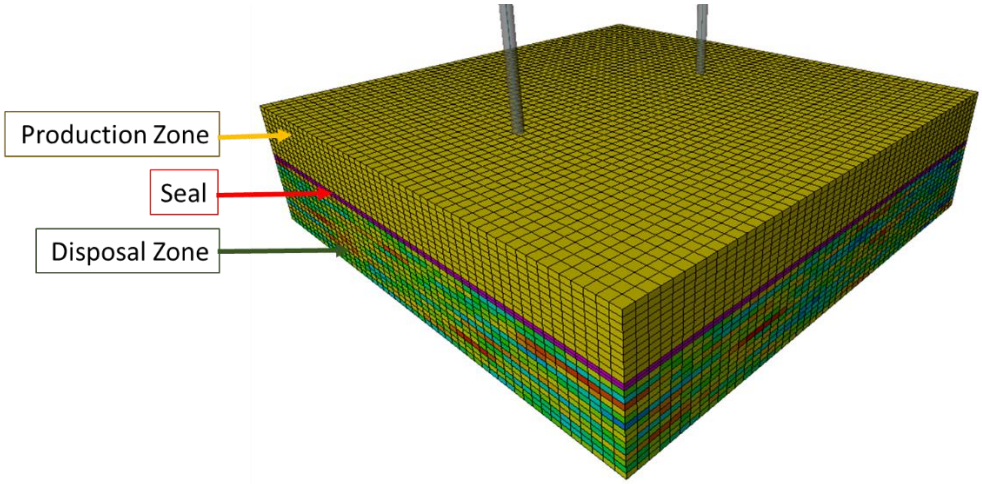

Figure 72. Schematic of the 3D model containing disposal zone and production zone separated by a seal

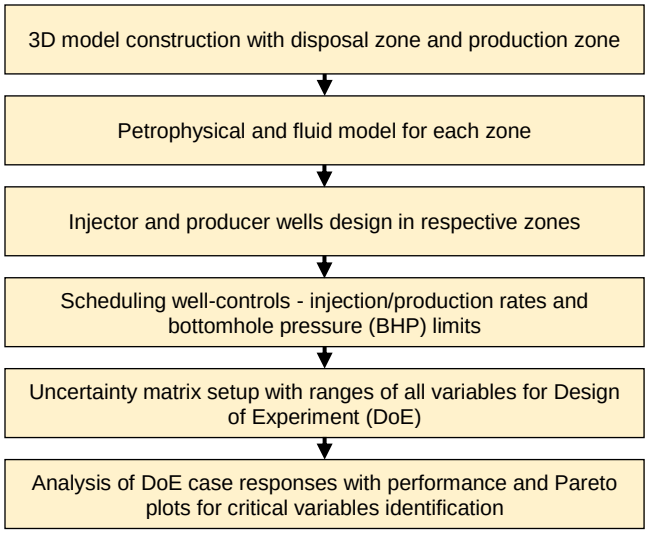

Figure 73. Schematic of the 3D model containing disposal zone and production zone separated by a seal

Uncertainty characterization is performed using the design of experiment (DoE). For this step, a list of parameters that can affect disposal-well performance is first identified. Appropriate ranges of these uncertain parameters are determined from the Arbuckle-specific sources. DoE simulation runs are performed, and responses examined via performance plots and Pareto charts. Pareto charts highlight the important factors affecting disposal-well performance variables, cumulative disposal water volume and disposal-well bottomhole pressure.

This workflow is applied to various scenarios, namely:

- Scenario 1: Base Case
- Scenario 2: Compressible fluid in a producing zone
- Scenario 3: Petrophysical heterogeneity in disposal zone
- Scenario 4: Presence of natural fractures
- Scenario 5: Communication through completion anomaly

For all five scenarios, fractional factorial design (level 2) over more compact design, such as Plackett-Burman as the DoE sampling template has been used. This step kept the number of simulation cases to a manageable number of 64. Additionally, it is intended to explore the extreme cases to bracket the solution space. The design choice, however, would not impact the conclusions or the applicability of the proposed approach. Description of various DoE can be found in Antony (2014).

Table 9 presents the uncertain parameters and their ranges for all five scenarios. A limited number of parameters for each scenario are considered to keep the simulation runs manageable. For a sealed compartment case, the vertical transmissibility of seal is zero, whereas that for a leaky compartment it is non-zero. The term "transmissibility" is standard in the reservoir-simulation literature. Transmissibility is comprised of a geometric component (stemming from the interface of the two adjacent cells) and a permeability component based on the values of the corresponding adjacent cells. Vertical anisotropy refers to the ratio of the vertical to lateral (or horizontal) permeability in the disposal zone and the producing zone. The uncertain parameters listed in Table 9 are based on Arbuckle-specific data. Morgan and Murray (2015) reported matrix and fracture permeability values. Porosity values considered are representative of this formation as characterized by History Matching process. Formation compressibility corresponding to the porosity values is obtained from the limestone-specific literature (Hall 1953, Newman 1973).

Table 9. Description of the uncertain parameters

Parameters	Low	High	Scenario 1	Scenario 2	Scenario 3	Scenario 4	Scenario 5
Vertical transmissibility multiplier of seal	0	10	√	√	√	√	√
Disposal zone formation compressibility, psi^{-1}	9E-6	5E-5	√	√	√	√	√
Production zone porosity, %	5	30	√	√			√
Disposal zone porosity, %	5	30	√	√	√	√	√
Production zone permeability, mD	5	50	√	√			√
Disposal zone permeability, mD	5	50	√	√	√	√	√
Vertical variogram range for porosity, ft	5	25			√		
Nugget for porosity	0.01	0.1			√		
Minor direction variogram range for porosity, ft	500	1200			√		
Major direction variogram range for porosity, ft	600	3600			√		
Matrix-fracture coupling	0.005	10				√	
Vertical anisotropy	0.1	10				√	√
Fracture porosity, %	0.5	3				√	
Fracture permeability, mD	500	5000				√	

Figure 74 through **78** identifies the critical factors impacting cumulative water injection and bottomhole pressure based on the Pareto plots for all five scenarios and **Table 10** presents a summary of the critical factors. These items will be discussed later for each scenario.

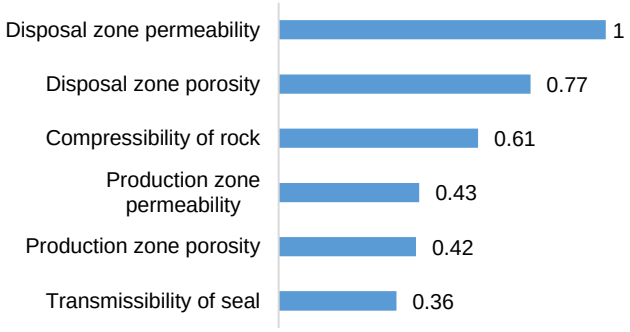

Figure 74. Impact of various parameters on cumulative disposal water volume and bottomhole pressure for the Base Case

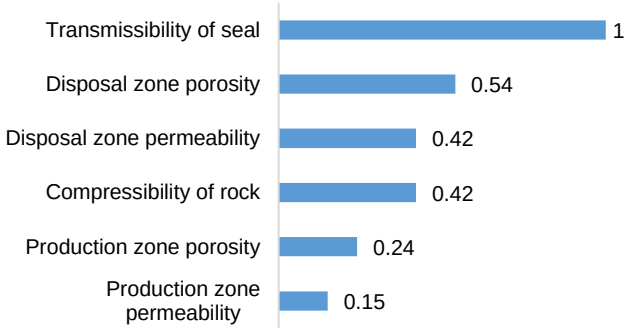

Figure 75. Impact of various parameters on cumulative disposal water volume and bottomhole pressure for the compressible fluid in producing zone scenario

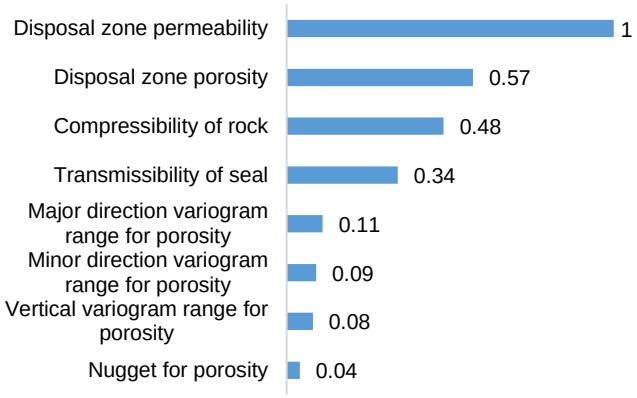

Figure 76. Impact of various parameters on cumulative disposal water volume and bottomhole pressure for the heterogeneity in disposal zone scenario

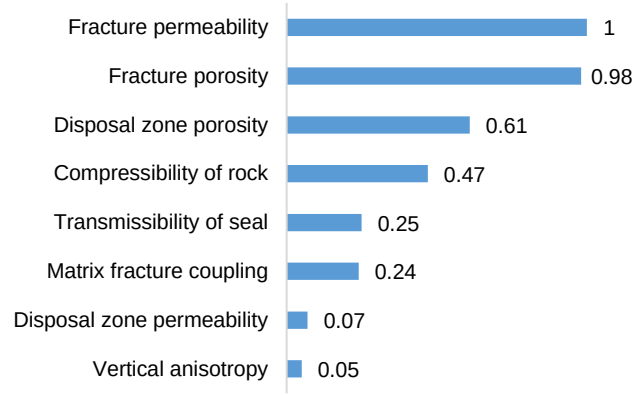

Figure 77. Impact of various parameters on cumulative disposal water volume and bottomhole pressure for the natural fractures scenario

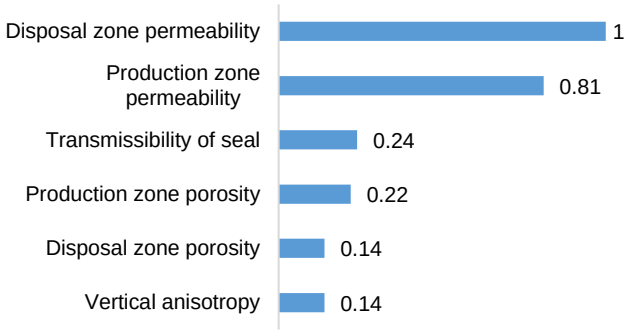

Figure 78. Impact of various parameters on cumulative disposal water volume and bottomhole pressure for the completion anomaly scenario

Table 10. Summary of critical factors for impacting cumulative injection and bottomhole pressure for all scenarios

Affecting variables→ / Scenarios ↓	Cumulative water injection (CWI)	Bottomhole pressure (BHP)	Combined CWI and BHP
Base case	Porosity, permeability and rock compressibility of disposal zone	Permeability and porosity of disposal zone and seal integrity	Porosity, permeability and rock compressibility of disposal zone
Compressible fluid in producing zone	Seal integrity and porosity, permeability and rock compressibility of disposal zone	Permeability, porosity and rock compressibility of disposal zone and seal integrity	Seal integrity and porosity, permeability and rock compressibility of disposal zone
Heterogeneity in disposal zone	Porosity, permeability and rock compressibility of disposal zone	Permeability and porosity of disposal zone and seal integrity	Porosity, permeability and rock compressibility

			of disposal zone
Natural fractures	Fracture porosity and permeability, porosity and rock compressibility of disposal zone	Fracture porosity and permeability, porosity and rock compressibility of disposal zone	Fracture porosity and permeability, porosity and rock compressibility of disposal zone
Completion anomaly	Vertical anisotropy and permeability of production zone	Permeability of disposal and production zone	Permeability of disposal and production zone

5.2.1. Base Case

In this scenario, all three zones (disposal zone, producing zone, and the seal) have homogenous petrophysical properties. Producing zone contains a slightly compressible fluid. **Table 11** presents the Base Case model description. The specifications described in the Base Case model are based on Arbuckle-specific data.

Table 11. Specifications of the base model.
(* indicates specification included in DoE)

Specification	Value
Compartment size	574 acres
Gross interval of compartment	700 ft
Maximum bottomhole pressure limit	2800 psi
Porosity of disposal zone*	10%
Permeability of disposal zone*	5 mD
Porosity of production zone*	15%
Permeability of production zone*	5 mD
Formation compressibility of disposal zone*	9E-6 psi^{-1}
Transmissibility multiplier of seal*	1

The average inter-well distance typical for the disposal wells in the Arbuckle zone is 5,000 ft. Therefore, the dimension of the simulation models corresponding to 5,000 ft is fixed. Gross interval is determined using average perforation thickness (Oklahoma Corporation Commission, 2017). Stratification-specific information for the Arbuckle Group is not available in well-logs or other records. For this study, the effect of stratification is ignored for simplicity. However, the effect of vertical anisotropy and gross interval is investigated as discussed later.

The maximum bottomhole pressure limit of 2,800 psi is considered based on the fracture gradient of 0.65 psi/ft for a perforation depth of 4,300 ft. Perforation depth of 4,300 ft is the typical depth for the disposal wells penetrating the Arbuckle Group. **Figure 79** displays the injection profile for all the cases. The injection-rate profile is considered in line with the wells in the Arbuckle Group.

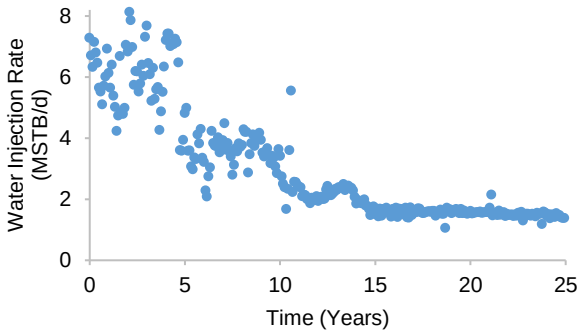

Figure 79. Well injection profile for all scenarios

For the Base Case, the impact of porosity and permeability of producing and disposal zones, formation compressibility of disposal zone and transmissibility of seal are investigated. A total of 64 cases constructed in the DoE are simulated. **Figure 80** presents the cumulative water injection profile of six extreme cases out of total 64 DoE case-responses. Cumulative injection profiles can be broadly classified into two categories: one having low disposal-zone permeability (labeled 3, 4 and 5 in Figure 80) and the other high (labeled 1, 2 and 6 in Figure 80). For the profiles 1, 2, 3 and 4, disposal-zone porosity is high, while for the profiles 5 and 6, it is low. Profile 1 has higher formation compressibility compared to Profile 2. Profile 3 has leaky seal compartment while Profile 4 has sealed compartment.

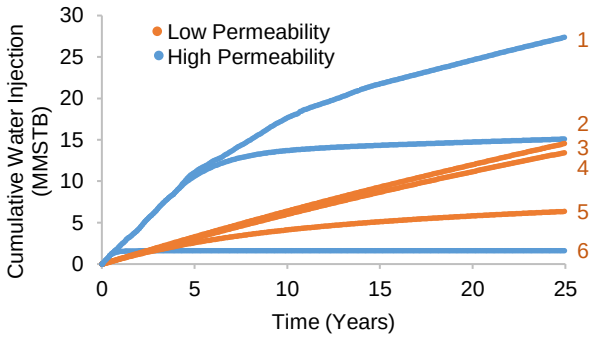

Figure 80. Cumulative water injection profiles of six extreme cases out of total 64 DoE case-responses for the Base Case scenario

When the properties are homogenous as in the Base Case, dominant factors (see Figure 74) are permeability, porosity and rock compressibility of the disposal zone. This aligns with the conventional wisdom. Similar findings are presented in Saripalli et al. (2000). In subsequent scenarios, changes are made to the Base Case to understand the impact of various parameters.

5.2.2. Compressible Fluid in the Producing Zone

The compressibility of the total system increases significantly in the presence of gaseous phase. This may have an impact on disposal-well performance where the producing zone is in communication with the disposal zone. The disposal zone will be in communication with the overlying producing zone when the vertical transmissibility of the seal is non-zero. This effect is investigated in this section. As Table 9 suggests, uncertainty parameters for this scenario are the same as the Base Case scenario.

When the disposal zone is in communication with a producing zone having compressible fluid, the seal integrity plays a significant role, as Figure 75 suggests. The more compressible the fluid in the communicating producing zone, the stronger will be the impact on injectivity. Porosity, permeability, and rock compressibility of the disposal zone have relatively less impact on disposal-well performance.

5.2.3. Petrophysical Heterogeneity in Disposal Zone

Heterogeneity in petrophysical properties will have a strong impact on well performance. In this scenario, the role of heterogeneity in disposal process is explored. Keeping all other parameters of the Base Case, heterogeneous porosity

and permeability distributions using vertical, major and minor direction variogram values, and nugget for porosity distribution are constructed for DoE. First, 3D stochastic models of porosity are constructed. Permeability models are then co-simulated using porosity distribution as a secondary variable.

The Pareto plot in Figure 76 shows that permeability is most dominant. Other critical factors for the heterogeneous medium are porosity, rock compressibility of disposal zone, and seal integrity.

5.2.4. Presence of Natural Fractures

Dual-porosity models are used to investigate the effect of pre-existing natural fractures and the interaction between natural fractures and the matrix. The presence of natural fractures alters porosity and connectivity of the disposal compartments. Generally, these two parameters are key to the performance of disposal operation. In this section, three additional parameters related to natural fractures are investigated, as shown in Table 9. These parameters are fracture porosity, fracture permeability, and matrix-fracture coupling. Description of dual-porosity models can be found in the reservoir engineering literature (Barenblatt et al. 1960, Kazemi 1969).

Figure 77 suggests that natural-fracture permeability and porosity have, by far, a significant impact on injection-well performance, whereas matrix porosity and rock compressibility of the disposal zone have a secondary effect. However, the effect of the matrix-fracture interaction term is apparently small. This may be

an artifact of how the statistical Design of Experiments (DoE) is constructed. This effect shall be explored in a future study.

5.2.5. Communication through Completion Anomaly

Completion anomaly refers to situation where the isolation of the producing and the disposal zones has been compromised due to damaged or leaky packer between the two zones within the injection well string. In case of a faulty well completion configuration, injection water may partially and unintentionally be injected into the producing zone. Such an outcome, which is fairly common, compromises the sealing nature of the disposal zone. Given this reality, a scenario is considered where the injection-well completion is an openhole type, and communication between the injection zone and overlying producing zone can take place. The additional parameter (see Table 9) for uncertainty analysis is vertical anisotropy.

When both zones are in communication, the permeability of both disposal and production intervals will have a dominant effect on injection-well performance, as Figure 78 suggests.

5.3. Diagnostics for Wastewater Disposal-Well Monitoring

Safe water disposal operations can be achieved by continuous monitoring of the injection process and checking the injection behavior. In this section a workflow as shown in **Figure 81** is devised, to monitor and identify abnormal injection behavior and applied it to all the scenarios analyzed in the previous section. The workflow starts with the generation of injection rate and pressure

profiles. First, the injectant/native fluid interface pressure is estimated, which is designated as p_e. Thereafter, the Hall integral (I_H) and its derivative (D_{HI}) (Izgec and Kabir 2009) are calculated. When plotted against the cumulative water injection, the two curves of I_H and D_{HI} overlay for normal injection. As shown in **Figure 82**, departure point is the maximum cumulative injection point up to which the normal injection is apparent; that is, before the D_{HI} curve starts deviating from its I_H counterpart. Cumulative injection is determined by the departure point, which is defined as CI_D, and further analysis of injection behavior using this information is carried out.

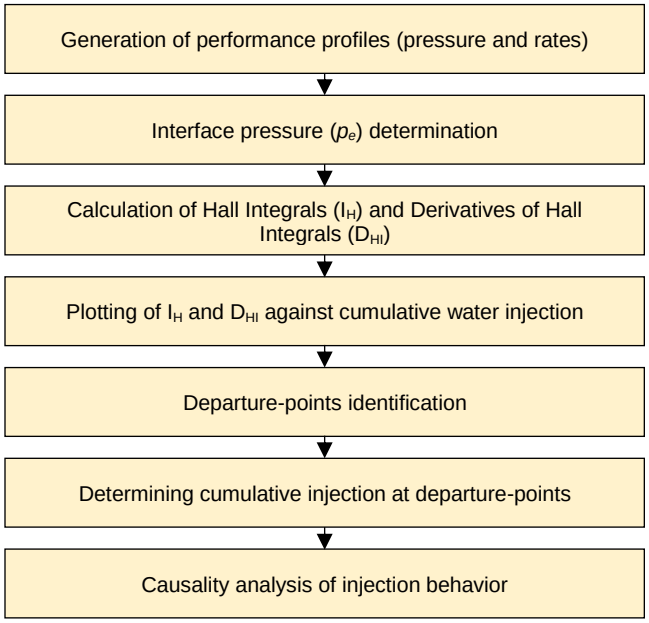

Figure 81. Wastewater disposal-well monitoring workflow

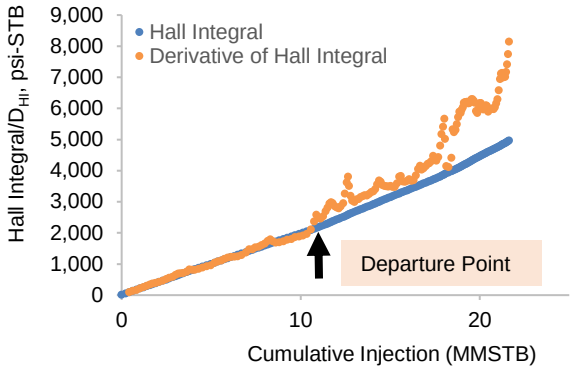

Figure 82. Departure point identification in the modified-Hall analysis plots

As discussed earlier in Chapter-3, in the modified-Hall analysis, the amount of pressure buildup in the disposal wells over time as well as the rate at which the pressure buildup takes place with injection, more precisely, cumulative injection volume are primarily determined and monitored. Under normal injection condition, both of these curves will have the same slope initially. When the disposal well experiences injectivity loss or some form of formation plugging, the derivative curve will deviate away (upward) from the Hall plot. That means the pressure is building up rapidly with small incremental injection. On the other hand, when disposal well experiences induced fracturing, the derivative plot will deviate away (downward) from the Hall plot. In this case, the pressure does not build up even when there is significant injection after the fracturing event.

In this analysis, single or multiple disposal-wells can be modeled in a consistent manner. The only complication that stems in the case of multiple disposal wells is that the virgin pressure around the disposal wells is affected by the flow from other interfering disposal wells. The proposed approach works in multi-well cases equally well.

Analysis involves calculation of percent pore-volume injection, which is designated as $PVI_{D\%}$, using the cumulative injection at the departure point (CI_D). $PVI_{D\%}$ is defined as CI_D divided by the pore-volume of the injection compartment. It is found that $PVI_{D\%}$ constitutes the major dependent variable in discerning safe operable limits. The underlying objective is to identify the limiting conditions of variables for safe operating conditions.

The above workflow and analysis are applied to all the identified scenarios. **Figures 83** through **92** show histograms of percent pore-volume injection and cumulative injection obtained from the analysis. In **Table 12**, the conditions where high percent pore-volume and cumulative injection exist and could be causing the abnormal injection behavior are summarized. It is identified that a pore-volume injection greater than 2% will trigger the abnormal behavior.

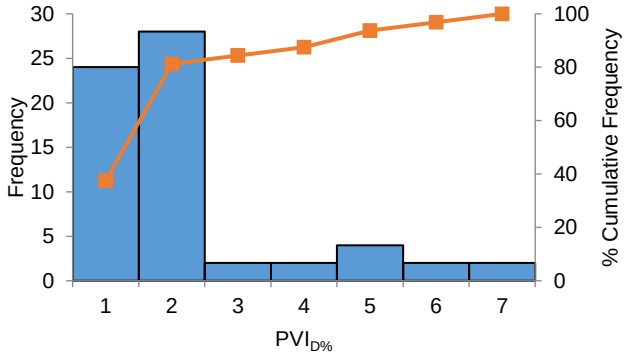

Figure 83. Histogram of % pore-volume injection – Base Case

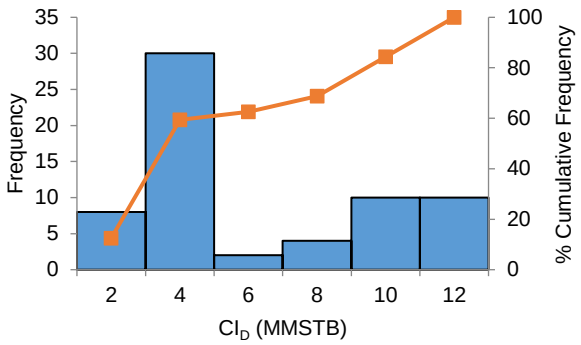

Figure 84. Histogram of absolute cumulative injection – Base Case

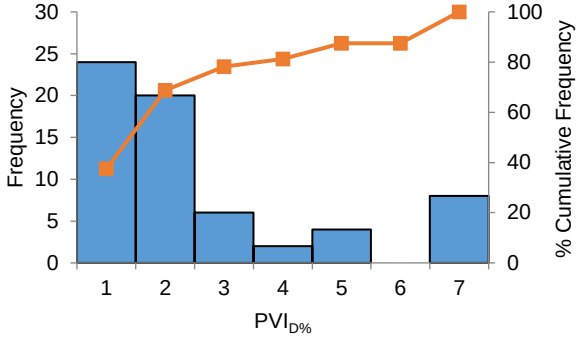

Figure 85. Histogram of % pore-volume injection – Compressible fluid in producing zone

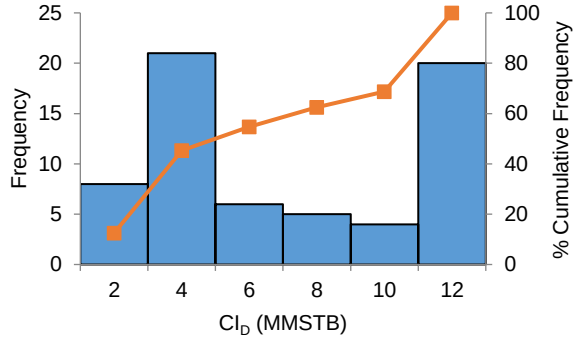

Figure 86. Histogram of absolute cumulative injection – Compressible fluid in producing zone

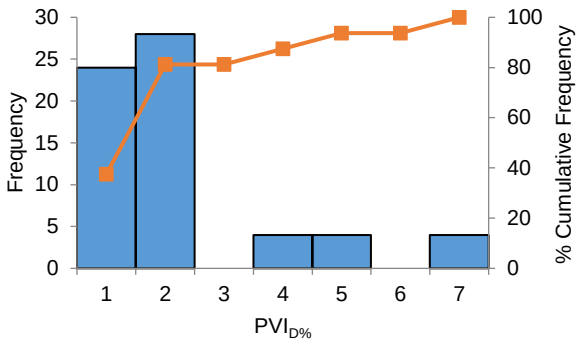

Figure 87. Histogram of % pore-volume injection – Heterogeneous scenario

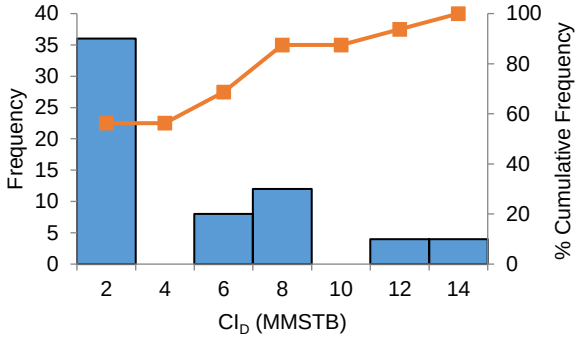

Figure 88. Histogram of absolute cumulative injection – Heterogeneous scenario

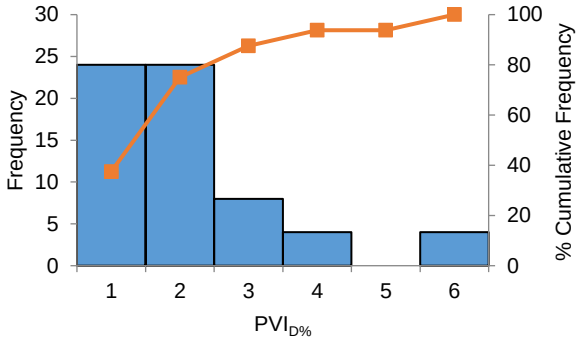

Figure 89. Histogram of % pore-volume injection – Natural-fractures scenario

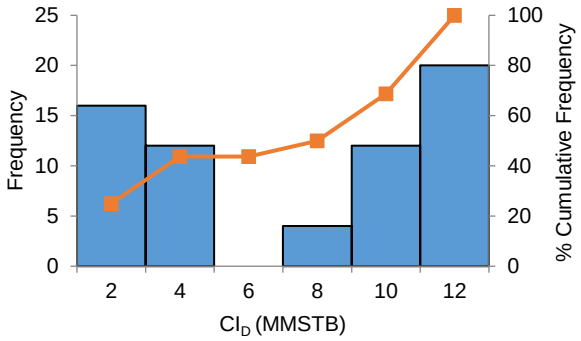

Figure 90. Histogram of % pore-volume injection – Natural-fractures scenario

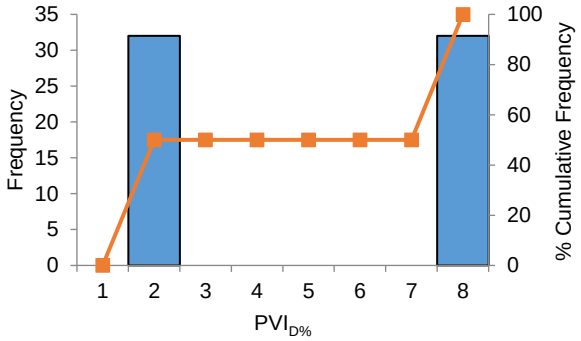

Figure 91. Histogram of % pore-volume injection – Completion anomaly scenario

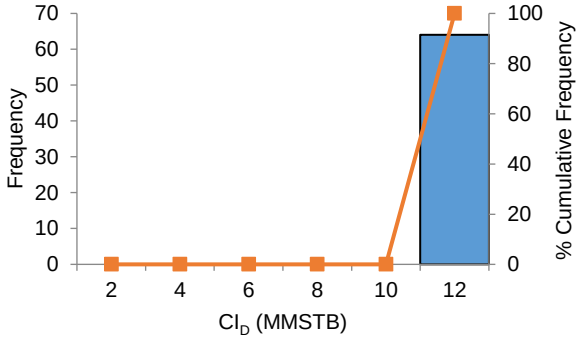

Figure 92. Histogram of % pore-volume injection – Completion anomaly scenario

Table 12. Conditions with high percent pore-volume and cumulative injection for all scenarios

Scenarios	Variables	
	Percent pore-volume injection ($PVI_{D\%}$)	Absolute cumulative injection (CI_D)
Base case	High conductivity allows more fluid injection and low porosity leads to low pore-volume - high $PVI_{D\%}$	High porosity and conductivity in disposal zone - high CI_D
Compressible fluid in producing zone	Leaky seal, along with high conductivity and low porosity - high $PVI_{D\%}$	High conductivity with leaky seal, or if seal is tight, high conductivity with high porosity - high CI_D
Heterogeneity in disposal zone	High conductivity and low porosity - high $PVI_{D\%}$	High conductivity - higher CI_D, expect when the seal is tight and formation compressibility is low
Natural fractures	Formation compressibility is high, and porosity is low in disposal zone, along with low fracture porosity and high fracture permeability - high $PVI_{D\%}$	High formation compressibility or high porosity in the disposal zone expect when the fracture porosity and permeability both are low - high CI_D
Completion anomaly	High permeability in disposal zone - high $PVI_{D\%}$	Constant cumulative injection profiles, as the fluid has enough porosity and conductivity to flow in both disposal and production zone

5.4. Impact of a Few Key Parameters

5.4.1. Effect of Porosity-Dependent Formation Compressibility

In the previous sections, the values of porosity and formation compressibility were varied independent of each other. Given that compressibility

has porosity dependency (Zimmerman 1986), this section explores the impact of porosity-dependent compressibility.

Two scenarios to study this effect of porosity-dependent compressibility are considered. In Scenario 1, formation compressibility is calculated using the pore-volume compressibility correlation with porosity for limestone (Jalalah 2006) as shown in **Eq. 16**. It is an empirical equation based on fitting data compiled data from different parts of the world. In Scenario 2, the compressibility value is kept constant at 1.8E-6 psi^{-1}. **Table 13** shows the values of porosity considered and the corresponding compressibility for both scenarios. Ten simulation cases are performed keeping the other parameters constant. Departure points are identified on the modified-Hall plots, and **Figure 93** displays the corresponding cumulative injection and percent pore-volume injection.

$$c_f = 5 \text{ x } 10^{-6} \cdot \phi^{-1} \quad (19)$$

Table 13. Compressibility values with corresponding porosity in both scenarios for comparing injectivity

Porosity (%)	Scenario 1 Compressibility (psi^{-1})	Scenario 2 Compressibility (psi^{-1})
2.5	2.0E-5	1.8E-6
5	1.0E-5	1.8E-6
10	5.0E-6	1.8E-6
15	3.5E-6	1.8E-6
20	2.4E-6	1.8E-6

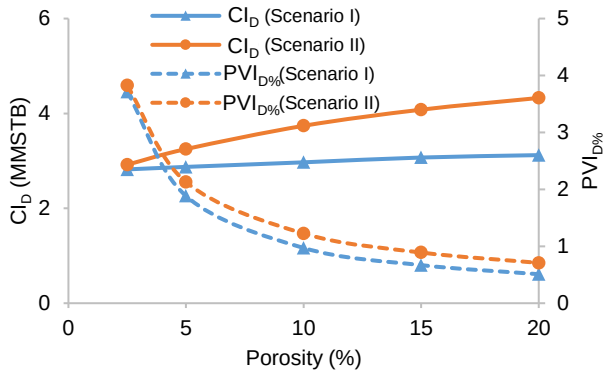

Figure 93. Percent pore-volume injection and cumulative injection show the effect of porosity dependent formation compressibility comparing varying and constant formation compressibility

It can be observed that cumulative injection (CI_D) is higher in Scenario 2 compared to Scenario 1. Also, with increasing porosity, there is a more pronounced increase in cumulative injection in Scenario 2 compared to Scenario 1. This study reveals that when both porosity and compressibility are considered independently, overestimation of the percent pore-volume injection ($PVI_{D\%}$) occurs because cumulative injection is too large. This overestimation can be as high as 40% at a porosity of 20%.

5.4.2. Effect of Injection Rate

One may question if the injection rate will affect the disposal operation. In this section, this point is investigated in the context of injection behavior. So far, injection-rate profiles similar to those observed in the Arbuckle Group disposal wells are considered. Here, injection rates in the multiples of 0.1, 0.25, 0.5 and 1.5 of the original injection-rate profile are considered. For each profile, a Design of Experiment (DoE) analysis using 16 simulation runs is carried out. **Figures 94 and 95** present percent pore-volume injection and cumulative injection at the departure points, determined using the modified-Hall plots and compared with the Base Case injection-rate (displayed in *x*-axis with a multiplier of one).

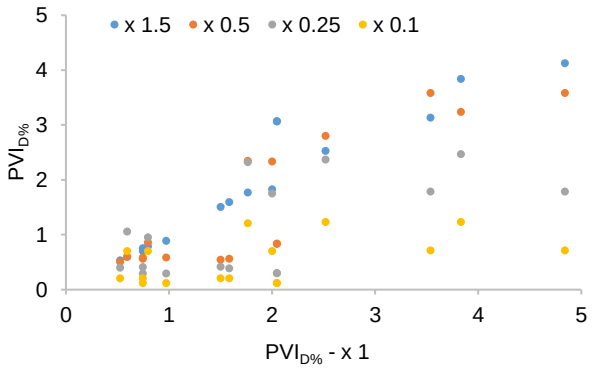

Figure 94. Percent pore-volume injection to show the effect of multiples of original injection rates

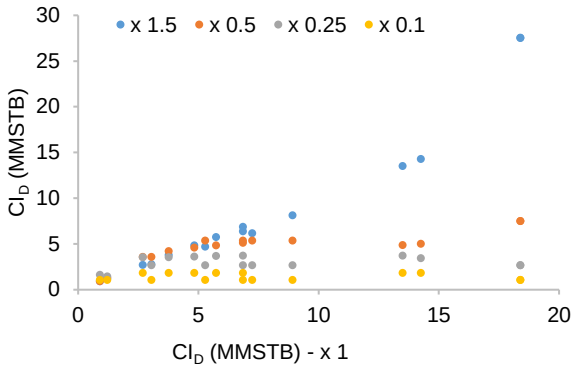

Figure 95. Cumulative injection to show the effect of multiples of original injection rates

Figures 94 and 95 display the injection-rate dependence on normal-injection behavior. They suggest that the high-injection rates (not high enough to fracture the formation) are favorable over those considered at lower rates. Saripalli et al. (2000) pointed out that injectivity declines with low injection rates. Note that the disposal volume is restricted to less than 2% of pore-volume under favorable conditions, such as that in the low-compressibility formation and in a large contiguous compartment. Zhu et al. (2017) illustrate the response of varying injection rate to reactivation of faults in detail.

5.4.3. Effect of Compartment Interval

Compartment thickness may have a different impact on well performance compared to compartment size. Gravity will also affect the well performance with increasing formation thickness. In all cases, a gross interval of 700 ft was considered. This value is based on the average perforation thickness of disposal wells in the Arbuckle. To understand the effect of the gross interval, a DoE analysis

using 16 simulation runs is carried out for interval thicknesses of 100 and 400 ft, respectively.

Percent pore-volume injection at the departure points for 100 and 400 ft intervals are shown in **Figure 96**. Only the sealed compartment cases are shown in this figure. The anomalously high percent pore-volume injection occurs for 100 ft interval with low porosity and high permeability. Apart from that, percent pore-volume injection for all the other cases is less than 2%. It can be concluded that disposal volume less than 2% of pore-volume will be a safe operational limit for disposal zones with a shorter gross interval.

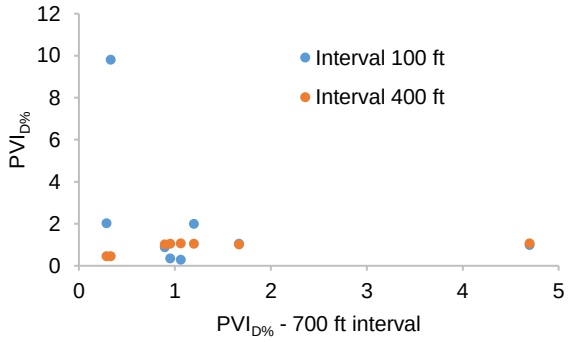

Figure 96. Percent pore-volume injection for gross interval of 700 ft (Base Case) with corresponding case of 100 ft and 400 ft intervals for sealed compartments

5.5. Impact of Compartment Size on Injectivity

Compartment size plays a very important role during the disposal process. Analysis showing the impact of compartment size on injectivity can be very useful in establishing safe operational procedure. In this context, the effect of different compartment sizes on injectivity under various conditions is investigated. **Figure**

97 presents a workflow to establish a relationship between the compartment size and cumulative injection. The same workflow reveals the correlation of fracture gradient with injectivity.

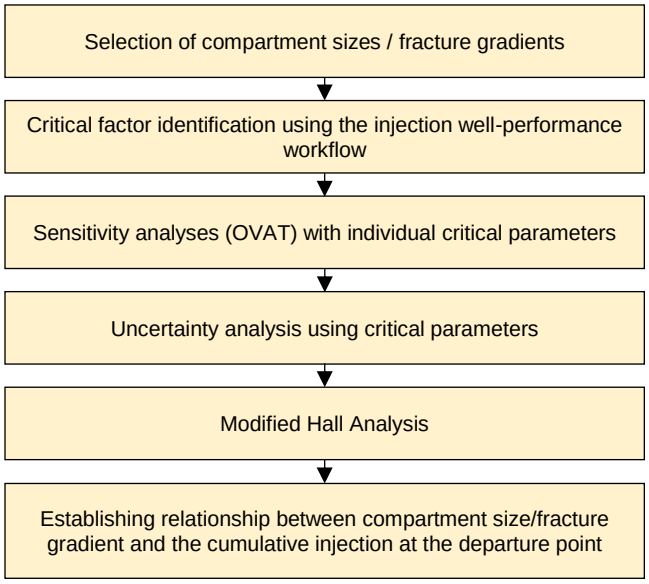

Figure 97. Impact of compartment size/fracture gradient workflow

In the workflow, compartment sizes are selected based on the range of inter-well distance for disposal wells in Arbuckle aquifer involving 144, 574, 1469 and 3305 acres. Thereafter, porosity, permeability, and compressibility of the disposal zone, and transmissibility of seal are selected as critical factors for the injection well performance workflow. The next step entails sensitivity analyses to check how each critical factor impacts compartment size. **Figures 98 through 101**, present the results from the diagnostics workflow applied for the sensitivity cases. The trend reveals that CI_D increases while $PVI_{D\%}$ decreases with increasing compartment size. From analysis carried out for porosity, $PVI_{D\%}$ in a low-porosity case is higher than those in a high-porosity case. This finding confirms the previous results; that

is, a lower formation porosity leads to lower available pore-volume, although $PVI_{D\%}$ is higher.

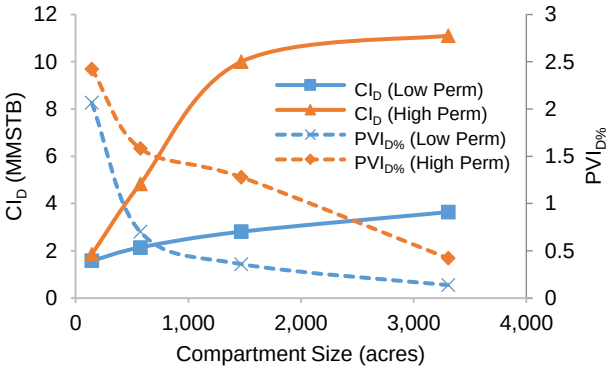

Figure 98. Impact of permeability on injectivity by varying compartment size

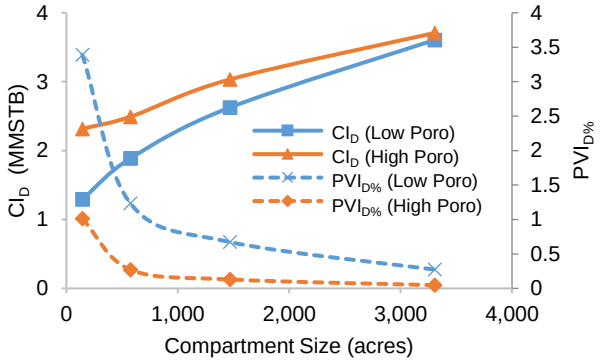

Figure 99. Impact of porosity on injectivity by varying compartment size

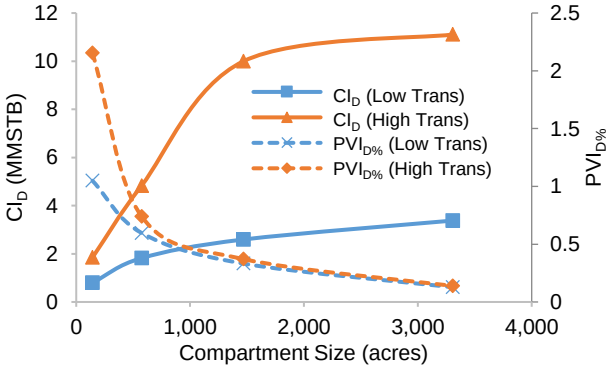

Figure 100. Impact of seal integrity on injectivity by varying compartment size

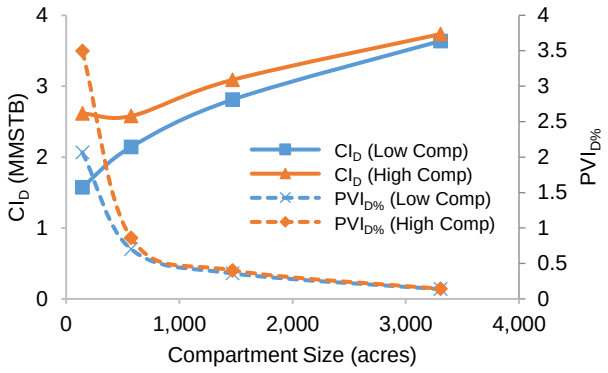

Figure 101. Impact of formation compressibility on injectivity by varying compartment size

Next, uncertainty analysis is performed using the critical factors for all the compartment sizes. **Table 14** presents the uncertainty matrix. Selecting the departure points on the modified-Hall plots became the cornerstone of this analysis. **Figure 102** presents a sample of identified departure points for the 1,469-acre compartment size. **Figures 103 and 104** display the relationship of percent pore-volume injection ($PVI_{D\%}$) and cumulative injection (CI_D) with compartment size, wherein the formation compressibility turned out to be the dominant parameter. Displayed within the orange envelope in the figures is a cluster of higher CI_D profiles, commensurate with high formation compressibility. In contrast, the blue envelope is a cluster of lower CI_D profiles, related to low formation compressibility. $PVI_{D\%}$ varies more in smaller compartment size compared to those in larger compartment size, where the values are lower. This observation is a consequence of the reciprocity effect of compartment pore-volume on percent-pore volume injection variable.

Table 14. Description of the uncertain parameters – Impact of compartment size and fracture gradient on injectivity

Parameter	Low	High
Disposal zone porosity, %	5	30
Disposal zone permeability, mD	5	50
Disposal zone formation compressibility, psi^{-1}	9E-6	5E-5
Transmissibility multiplier – seal	0	10

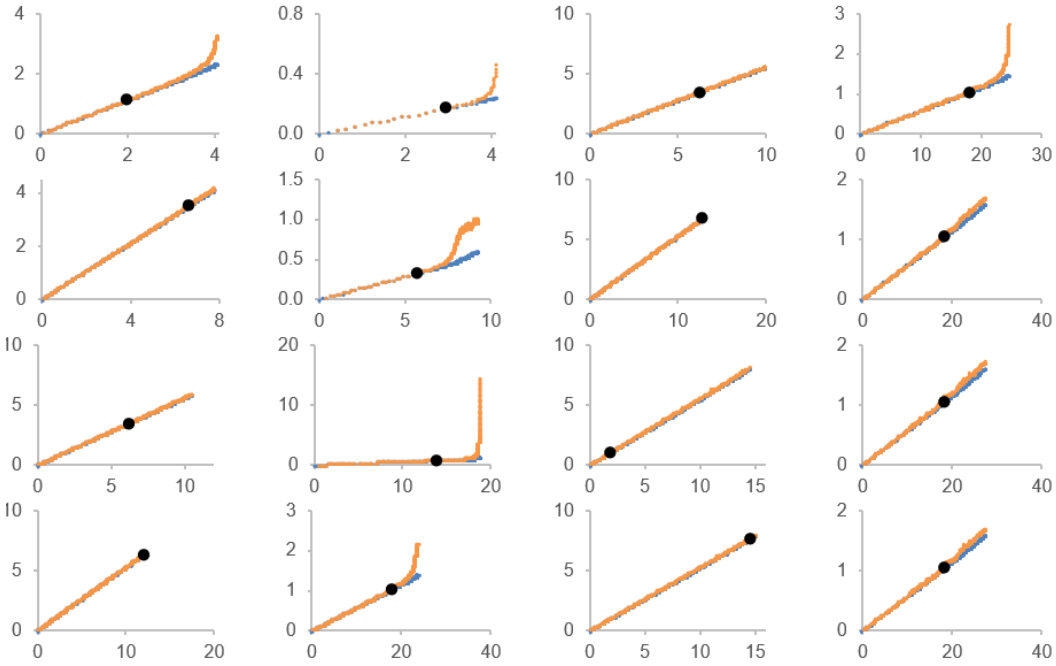

Figure 102. Example of departure points (shown as black dots) determination while analyzing the compartment size effect of 1469-acres. X-axis is cumulative water injection (MMSTB), Y-axis represents (psi-MMSTB) Hall Integral (blue) and Derivative of Hall Integral (orange)

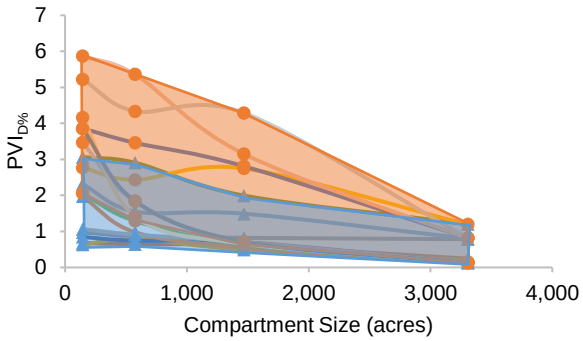

Figure 103. Relationship of percent pore-volume injection with compartment size, orange and blue envelopes are clusters based on formation compressibility

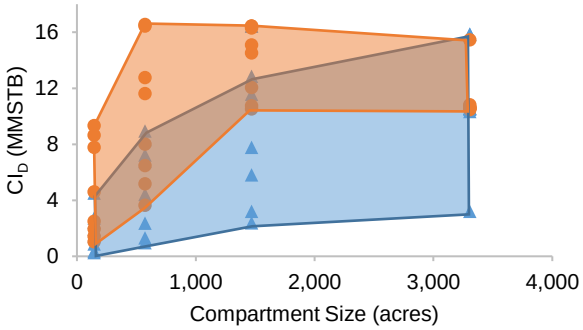

Figure 104. Relationship of absolute cumulative injection with compartment size, orange and blue envelopes are clusters based on formation compressibility

5.6. Correlating Fracture Gradient with Injectivity

Fracture gradient is defined as the maximum pressure gradient within which fractures are not induced in the disposal formation. In this study, the effect of fracture gradients via the maximum allowable bottomhole pressure is investigated. That is, if the formation fracture gradient is high, then the bottomhole pressure limit for injection will be high. This variable directly impacts the injectivity during disposal. Following the same steps, as shown in Figure 97**,** for determining the

effect of compartment size with injectivity, the relationship between cumulative injection and fracture gradient is developed.

A selection consisting of five pressure gradients ranging from 0.64 to 0.84 psi/ft (Holubnyak 2016) corresponding to maximum BHP limits of 2,800 to 3,650 psi, respectively is carried out. The same compartment size of 1,469 acres is retained in this study segment. The critical factors identified are porosity, permeability, formation compressibility of the disposal zone, and transmissibility of seal. **Figures 105** through **108** present the results of the sensitivity runs for these critical factors. As expected, the CI_D increased with increasing fracture gradient. In addition, the $PVI_{D\%}$ values are distinctly different for low and high porosity and permeability cases. However, these values are closer to the formation compressibility and seal integrity in the high and low cases. It can be inferred that, individually, porosity and permeability are more influencing in this study.

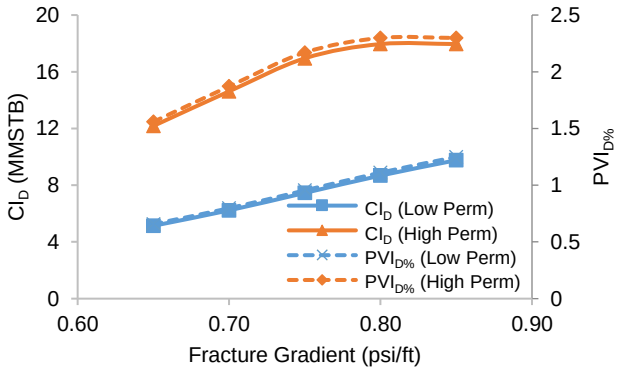

Figure 105. Impact of permeability on injectivity by varying fracture gradient

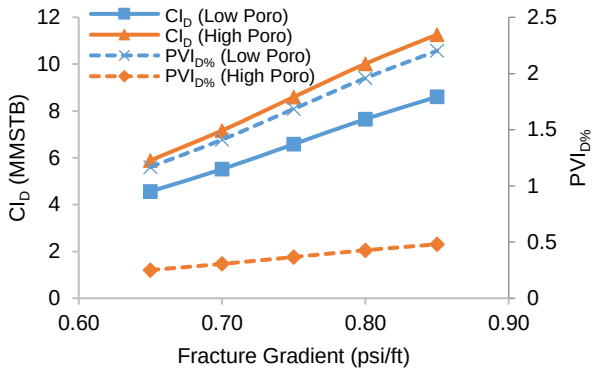

Figure 106. Impact of porosity on injectivity by varying fracture gradient

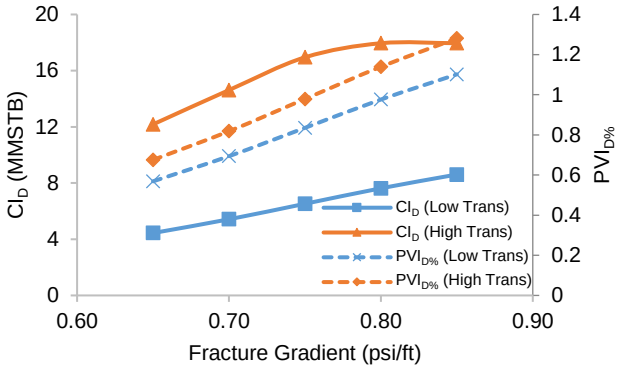

Figure 107. Impact of seal integrity on injectivity by varying fracture gradient

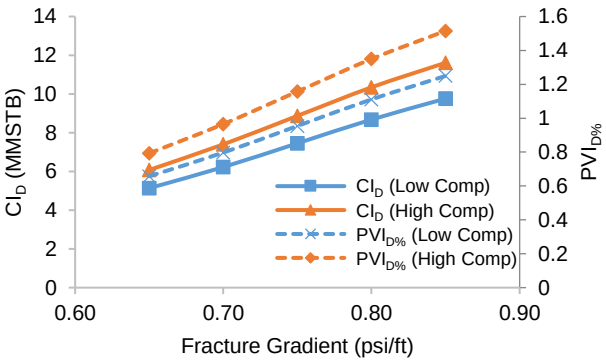

Figure 108. Impact of formation compressibility on injectivity by varying fracture gradient

The uncertainty matrix for fracture-gradient investigation is presented in Table 14. **Figures 109 and 110** show the relationship of absolute cumulative

injection (CI_D) and percent pore-volume injection ($PVI_{D\%}$) with fracture gradient. In general, $PVI_{D\%}$ increases with increasing fracture gradient. In the figures, orange envelope represents a cluster of high $PVI_{D\%}$ scenarios corresponding to high formation compressibility and low porosity. The blue envelope is a cluster of intermediate to low $PVI_{D\%}$ scenarios with low formation compressibility. While the green envelope clusters low $PVI_{D\%}$ scenarios found in high formation compressibility and high porosity. Thus, formation compressibility and porosity define the relationship between fracture gradient and injectivity.

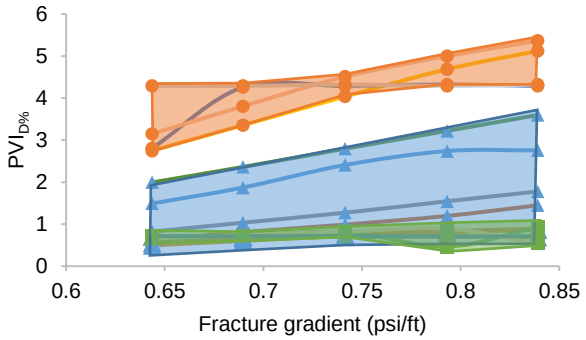

Figure 109. Relationship of percent pore injection with fracture gradient, orange, green and blue envelopes are clusters based on formation compressibility and porosity

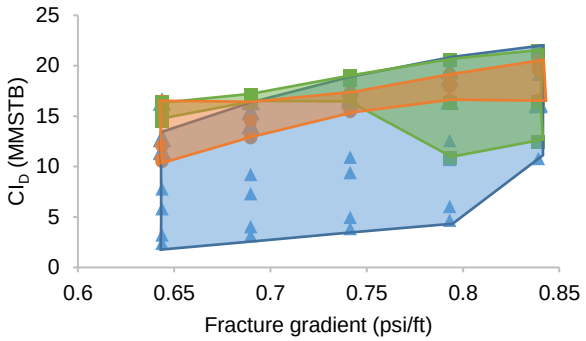

Figure 110. Relationship of absolute cumulative injection with fracture gradient, orange, green and blue envelopes are clusters based on formation compressibility and porosity

Around 300 simulation cases with sealed injection compartment are analyzed in this study. **Figure 111** shows a histogram of percent pore-volume injection ($PVI_{D\%}$) for all these simulation runs. The figure suggests that at about 80% probability, the percent pore-volume injection is less than 2%. However, a combination of high permeability, low porosity and high formation compressibility show higher percent pore-volume injection capability.

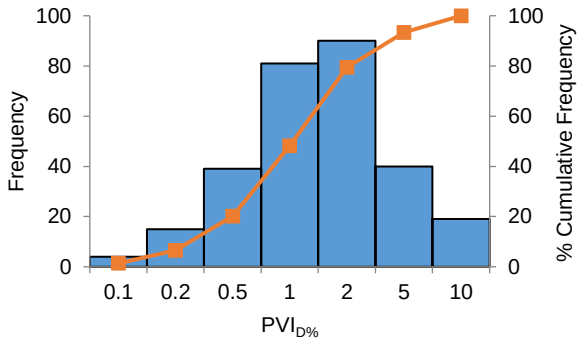

Figure 111. Histogram summarizing the percent pore-volume injection results of around 300 conditions having sealed compartments

5.7. Workflow for Safe Water-Disposal Operations

Lessons from all the studies are combined, and a simple workflow for the safe-water disposal operations is crafted, as shown in **Figure 112**. Well surveillance-data, such as injection rate and bottomhole pressure, and well completion data is required to implement the workflow. The use of rate transient analysis (RTA) ensured ascertaining the compartment volume. Certainly, geology and petrophysical information can assist in independent corroboration of the compartment volume.

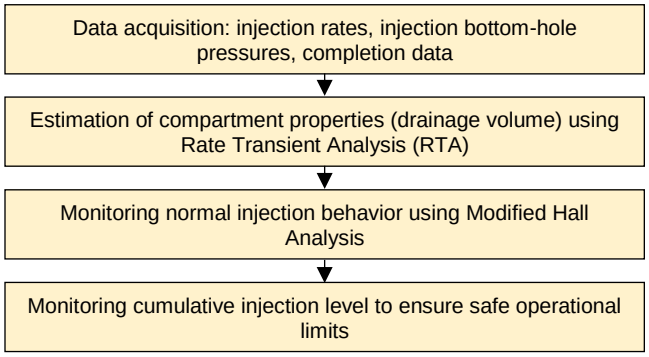

Figure 112. Workflow for safe water-disposal operations.

Next, the modified-Hall Analysis (Izgec and Kabir 2009) is used to monitor the real-time injection behavior. When the derivative of Hall integral deviates from the Hall integral, the injection limit is reached. Additionally, the cumulative injection and percent pore-volume injection should be continuously checked, to keep it within the safe operating limits. As a rule of thumb, the percent pore-volume injection needs to be kept less than 2% of the container volume for safe water disposal operation. The compartment size obtained from the rate-transient analysis or RTA constitutes the critical element in this workflow. It can be noted that the

fundamental purpose of RTA as used in the reservoir-engineering discipline pivots on estimating the connected pore volume in the presence of late-time boundary-dominated flow in producing wells. Here, an attempt to replicate the same idea in the context of available and contiguous pore volume connected with each disposal well is made.

I determined the average inter-well distances based on Arbuckle Group disposal wells. I obtained the average perforation-interval thickness from the completion reports. Both the average inter-well distance and perforation interval determined the compartment size for the synthetic models. The pore volume is simply the product of the disposal zone bulk volume and the net porosity. However in a realistic setting, I propose to use RTA of the injection rates and pressure to determine the equivalent pore volume intercepted by the disposal well.

Two cases for determining the compartment volume are presented here. One case had a sealed compartment and the other one contained a leaky fault. A compartment size of 1,469 acres was considered in both cases. **Figures 113 through 116** show the RTA results, including the p and q match, the log-log and the Blasingame type-curve plots, as detailed in Houze et al. (2017), for the tightly sealed compartment case. **Figures 117 through 120** show the RTA results for the leaky-fault. The compartment size, using RTA, was estimated to be 1,415 acres for the sealed compartment case and 1,552 acres for the leaky-fault case. As expected, in case of leaky fault case, the estimated compartment size turned out to be somewhat larger than the actual size due to fluid leakage. These results validate that RTA technique can yield a good estimate of the compartment size.

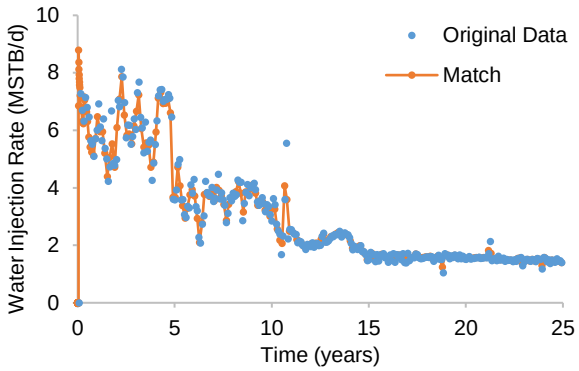

Figure 113. RTA results - q match (tightly sealed compartment)

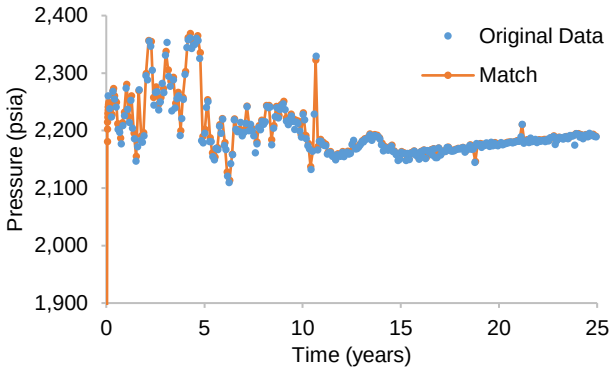

Figure 114. RTA results - p match (tightly sealed compartment)

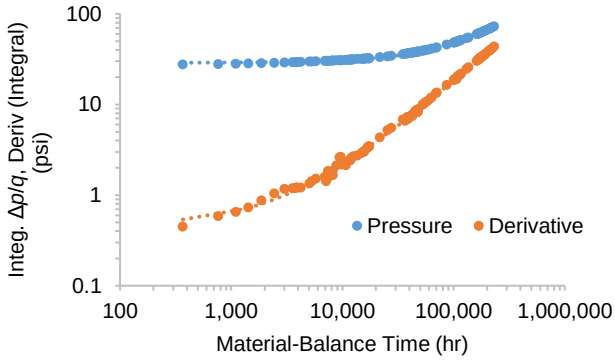

Figure 115. RTA results – log-log diagnostic (tightly sealed compartment)

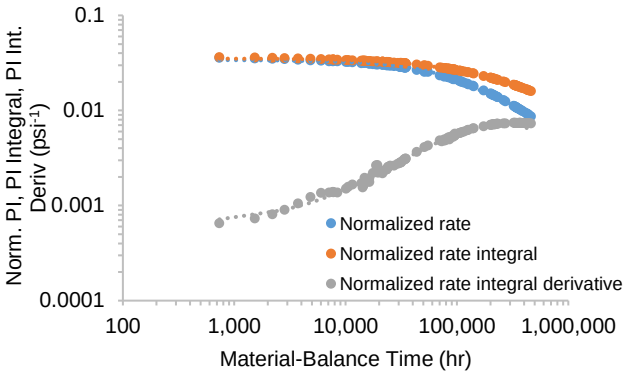

Figure 116. RTA results – Blasingame type curve (tightly sealed compartment)

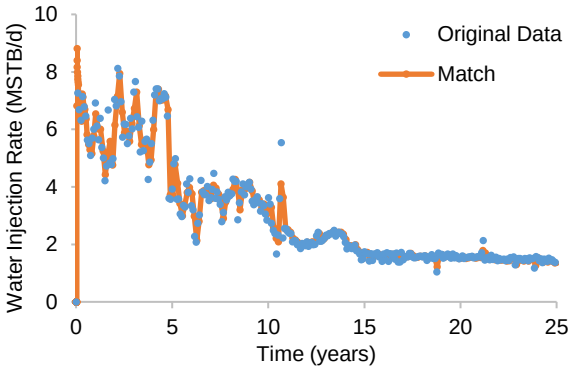

Figure 117. RTA results - q match (leaky fault)

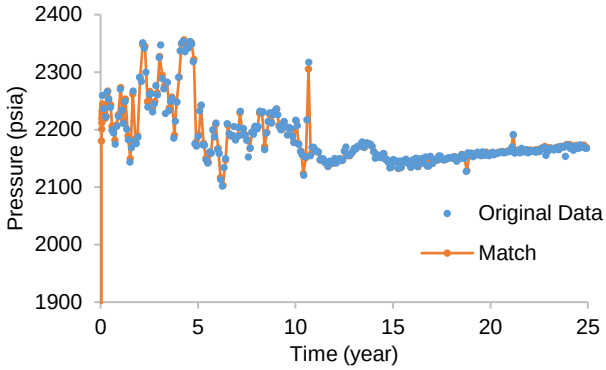

Figure 118. RTA results - p match (leaky fault)

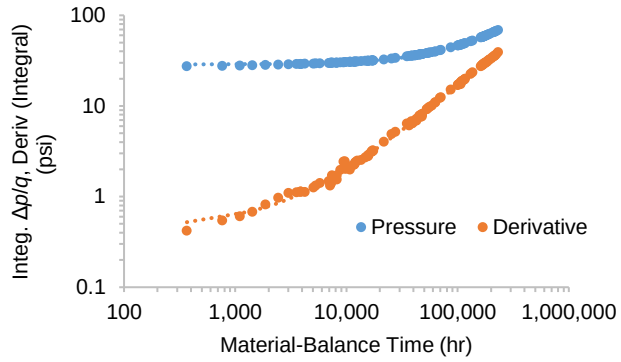

Figure 119. RTA results – log-log diagnostic (leaky fault)

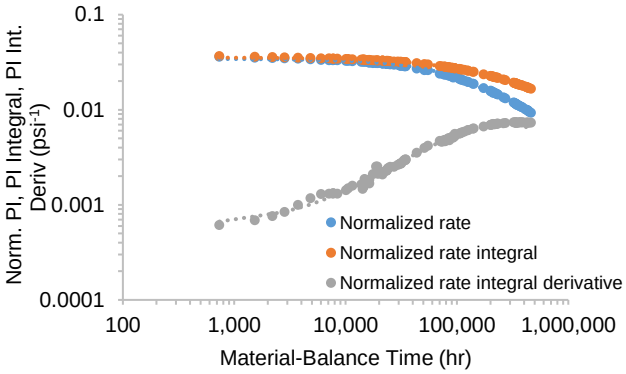

Figure 120. RTA results – Blasingame type curve (leaky fault)

In this chapter, I got a deep insight into the wastewater disposal process and the learning was based on studying various sub-surface scenarios. The parameters that affect the disposal process were also studied. Modified-Hall analysis (MHA) was not only used to understand the limiting behavior of disposal but also to quantify the safe amount of disposal. These learnings led to formulating an operational practice for safe-disposal. Compartment size was required for this process, which was obtained using Rate Transient Analysis (RTA). Next, I will present a few points of discussion, conclusions and recommendations based on the entire study.

Chapter 6: Discussion and Conclusions

In this chapter, I summarize the efforts to investigate and monitor the wastewater disposal process with the help of available information from the Arbuckle-Group formation. I also discuss the assumptions and limitations of the study. Finally, I shall present key findings of the study.

6.1. Discussion

Arbuckle-Group was chosen as a zone of interest as huge volumes of wastewater is disposed in this formation and an increase in seismicity linked with this process is observed. An integrated team of geophysicists, geologists and engineers were involved in this work. This study focuses on the engineering aspect of the integrated analysis.

I used 3D seismic survey, well log data, injection and completion data for 29 wells for the study. I estimated porosity, permeability, mineralogy and geomechanical properties of core samples from the SHADS #4 well in Rogers County, Oklahoma. I carried out analysis on injection dataset which includes performing data quality checks, conversion of the well-head pressure to bottom-hole pressure, identification of flow regimes using material time-balance diagnostics plot, estimating ambient reservoir pressures using Silin slope analysis and understanding the injection behavior of the wells using modified-Hall analysis. I also carried out a quick analysis to correlate the injection parameters with the seismicity.

I created a model for history matching process using the geological static model and available information about the study area. I carried out history matching iterations using the identified impactful parameters, until a reasonable match for bottom-hole pressure and injection rate is obtained. I also studied the behavior of the faults. There is a further scope to improve the characterization by carrying out more stages of history matching.

Various assumptions and limitations pertaining to these efforts include:

- No core data were available for the wells under study. Core data would enable us to create better porosity and permeability models initially with the availability of this data.
- Quality of the public datasets (injection and completion data), is of limited reliability. I commonly encountered conditions like averaged pressures and injection rates, abnormally high pressures and rates, increasing pressure with decreasing injection or vice-versa.
- The injection dataset contained wellhead pressures, however, the bottom-hole pressure is required for most of the analysis. To enable this conversion key parameters such as temperature, salinity and flowing conditions among others were not available. A judgment of key parameters was obtained using sensitivity analysis.
- The information regarding the fluid distribution in the study area is not available. As a part of this study, I considered the Arbuckle-Group and the connected basement to be entirely water saturated.

- There is limited information available regarding the Arbuckle-connected basement formation. Only a handful of well logs penetrate the basement. However, as pointed in literature, most of the seismic events take place in basement.

In the effort to learn the disposal process, I used a systematic approach to understand the overall issues surrounding wastewater disposal in saline aquifers, specifically in the Arbuckle Group in Oklahoma. The same method can be followed in any setting to assess the limits of safe water disposal requirements. In this context, specific workflows provide the foundations for understanding the physical processes of disposal and diagnostics for real-time monitoring.

The applicability of these workflows and analyses can be useful provided good quality injection data are available. Competent surveillance techniques proposed in this study become a requirement in recognizing the need for changing the disposal compartment. In this regard, operators and participating agencies alike need to implement the simple surveillance guidelines and frequent data analysis as espoused here for ensuring safe disposal operations. In this context, it is proposed that the modified-Hall plot is critical in that it alerts us when to cease injection in a given interval. In this study, monitoring of injection volumes and pressure using the proposed approach is recommended as a bare-bone surveillance method for injection wells. However, additional surveillance, such as temperature survey, pressure monitoring for well and completion integrity as suggested by Macary et al. (2012), among others, can bolster the cause for disposal.

The workflows encompassed various scenarios and a range of independent parameters in this study involving both single- and dual-porosity systems using simplified fluid-flow simulation models. However, faulted architecture of the disposal formation and geomechanics will play a significant role in disposal-well and formation dynamics and induced seismicity (Umholtz and Ouenes, 2016; Walsh and Zoback, 2015; Dusseault, 2010). Fan et al. (2016) have carried out geomechanical analysis to study the link between water disposal and initiation of seismic fault slip. A disposal formation with conductive faults communicating with overlying producing zone will have similar characteristics to the case where seal integrity is compromised and will accommodate a large volume of disposal water. On the other hand, sealing faults in the disposal formation will act as flow barriers and the container size will shrink, which will accommodate a smaller volume of disposal water. Notwithstanding, a full-blown study coupling fluid flow and geomechanical stress simulation will enhance the overall understanding of other disposal opportunities. This aspect will be probed in a future investigation.

More subsurface and operational scenarios involving variable salinity of injection water and the presence of solids, among other variables affecting disposal performance, need probing. Stress-sensitive permeability, permeability-reduction phenomena or effect of thermal stress have not been investigated in this study. These aspects can be addressed in future efforts to enhance understanding of the wastewater-disposal formation dynamics further.

Another aspect of produced water management and disposal is the chemical composition of the disposed water. Various technologies are available for recycling

and purification (removing salt, oil and grease contents) of the disposal water (Veil et al., 2011; Shafer, 2011). Al-Taq et al. (2017) suggested loss of injectivity takes place if suspended solids exceed 50 ppm, mean particle size exceeds 5 microns, the oil content exceeds 5 microns, or continuous injection is disrupted triggering particle settling. In this study, these aspects are neither investigated nor their impact on injectivity studied. Additionally, chemical reactions or mineral-water interactions are not discussed. An investigation coupling water chemistry, fluid flow, and stress simulation to ascertain the injection limits will be beneficial to the community. The approach of monitoring injection wells using modified-Hall plot will apply in these conditions where formation plugging is occurring (Izgec and Kabir 2009).

Overall, the results pointed to 2% of the container volume as the maximum safe disposal volume with 80% probability. The allowable disposal volumes are in substantial alignment with the CO_2 storage efficiency figures for limestone formations discussed in Goodman et al. (2011) and EIAGHG report (2009). Earlier, Ehlig-Economides and Economides (2010) suggested 1% of supercritical CO_2 disposal, while Zhou et al. (2008) proposed 0.5%. Multiphase flow condition in the case of CO_2 disposal in aquifers will have trapping mechanisms that may constrain the allowable injection volume to be lower than that in the wastewater disposal situation.

This approach should be considered as a proactive measure for monitoring disposal well performance. Induced seismicity can be prevented or minimized if safe operational practice proposed in this study is put in place. The primary

objective here is to establish a diagnostics and monitoring means for water-disposal wells. Irrespective of the physical processes, the ability to diagnose normal injection behavior can be achieved using the proposed approach. It is acknowledged that when multiple physical processes are in play, there may be compensating phenomena occurring that can prolong or reduce the duration of normal injection behavior. The monitoring and diagnosing approach will not change. However, the observed likely safe injection of 2% cumulative pore-volume injection may turn out to be marginally different.

6.2. Conclusions

Key conclusions from the characterization of Arbuckle-Group study are as follows:

- Average porosity and permeability of the Arbuckle-Group formation ranges between about 7% and 10 mD, respectively.
- I observe a slight lateral permeability anisotropy of 1.25 towards the Northing direction with respect to Easting direction evident in the Arbuckle-Group and observe vertical to lateral permeability anisotropy (k_v/k_h) is approximately 0.01 for the Arbuckle-Group.
- Dominant parameters affecting history-match are permeability, horizontal and vertical anisotropy and porosity of Arbuckle-Group, permeability and horizontal anisotropy of overlying Simpson and the underlying basement formations, formation water density and viscosity, and productivity index (PI) multipliers (for the injection wells).
- Faults play an important role in characterizing Arbuckle Group formation.

Important conclusions from water-disposal investigation are as follows:

- Besides porosity, permeability, and compressibility, seal integrity plays a critical role in water disposal storage. In general, the cumulative storage is tied to high-porosity and high-permeability systems due to favorable transmissivity for disseminating pressure.
- The overall disposal volume is restricted to less than 2% of pore-volume under favorable conditions, such as low-compressibility formation in a large contiguous compartment. The same 2% criterion also applies in a sealed compartment with 80% probability while considering a number of variables.
- The presence of natural fractures in the disposal zone improves the formation compressibility and transmissivity, leading to the increase of cumulative injection compared to its single-porosity counterpart.
- The proposed workflow for safe water-disposal operations as presented here involves continuous monitoring of the injection profile (of both injection volumes and pressure) with the modified-Hall plot to ensure a safe operating limit, and assessing the compartment size from the rate-transient analysis. Modified-Hall plot will indicate if the normal injection is taking place. Knowledge of the container size will assure if the cumulative injection volume is within the safe limit (~2% of pore-volume).

Chapter 7: Recommendations

In this study, I present an initial characterization Arbuckle-Group in Payne County, Oklahoma. I have analyzed from the wastewater disposal process in this confined reservoir and proposed monitoring and diagnostics techniques for safe wastewater disposal operation. I have also identified a few areas where additional work can be carried out for a deeper understanding of the problem and obtaining improved results. I recommend the following for future work:

- Improve characterization of Arbuckle-Group in the same study area by carrying out more stages of history matching and learn the fault-conductivity characteristics.
- Conduct a study to forecast the pressure propagation and build-up on allowing further injection in this area using fluid flow simulation is possible.
- Construct 3-D Mechanical Earth Model (MEM) representing the geomechanical properties of the formations. A workflow to this end had been established, however, the investigations could not be completed given the data available. Comprehensive understanding of the behavior of the Arbuckle-Group and basement formations, can be further enhanced through coupled fluid-flow and geomechanical stress simulation.
- Explore simpler analytical techniques such as RTA in more detail for all the disposal wells, estimating the compartment size around these wells. Knowledge of the compartment size will enable monitoring these wells using the scheme devised in this thesis.

- Examine additional scenarios including variable salinity of injection water and the presence of solids in the injection fluid, among the others can help to improve the understanding of the wastewater disposal process.
- Further develop the scenario having partial hydrocarbon fluid distribution was considered for analysis that was not investigated in detail in this study.
- Examine the effect of chemical composition of the disposal water and its interaction with the formation rock and fluid.

References

Abrahams, L. S., Norbeck, J. H., and Horne, R. N. 2017. Investigation of Physical Mechanisms that Influence Injection-Induced Earthquake Sequence Statistics. Presented at 42nd Workshop on Geothermal Reservoir Engineering, Stanford University, Stanford, California, USA, 13-15 February. SGP-TR-212.

Akinnikawe, O. and Ehlig-Economides, C. A. 2016. Geologic Model and Fluid Flow Simulation of Woodbine Aquifer CO_2 Sequestration. *Int J Greenh Gas Control* **49** (June): 1–13. http://dx.doi.org/10.1016/j.ijggc.2016.02.014.

Al-Taq, A. A., Al-Dahlan, M. N., and Alrustum, A. A. 2017. Maintaining Injectivity of Disposal Wells: From Water Quality to Formation Permeability. Presented at the SPE Middle East Oil & Gas Show and Conference, Manama, Kingdom of Bahrain, 6-9 March 2017. SPE-183743-MS. https://doi.org/10.2118/183743-MS.

Anchliya, A., Ehlig-Economides, C. A., and Jafarpour, B. 2012. Aquifer Management to Accelerate CO_2 Dissolution and Trapping. *SPE J.* **17** (3): 805–816. SPE-126688-PA. https://doi.org/10.2118/126688-PA.

Anderson, D.M., and Mattar, L. 2004. Practical Diagnostics using Production Data and Flowing Pressures. Presented at SPE Annual Technical Conference and Exhibition, Houston, TX, USA 26-29 September. SPE-89939-MS. https://doi.org/10.2118/89939-MS.

Antony, J. 2014. *Design of Experiments for Engineers and Scientists*, 2nd Edition. Waltham, MA: Elsevier.

Aschehoug, M. and Kabir, C. S. 2013. Real-Time Evaluation of Carbon Dioxide Production and Sequestration in a Gas Field. *SPE Res Eval & Eng* **16** (2): 134–143. SPE-163149-PA. https://doi.org/10.2118/163149-PA.

Baker, T. 2016. Wells located within Expanded Areas of Interest for Triggered Seismicity. Oklahoma Corporation Commission.

Ballard, B. 2007. Quantitative Mineralogy of Reservoir Rocks Using Fourier Transform Infrared Spectroscopy. Presented at the Annual Technical Conference and Exhibition, Anaheim, California, USA 11-14 November. SPE-113023-STU. https://doi.org/10.2118/113023-STU.

Barenblatt, G.I., Zheltov, I.P., Kochina, I.N., 1960. Basic concepts in the theory of seepage of homogeneous liquids in fissured rocks. *J of Appl Math and Mech* **24** (5), 1286–1303.

BC Oil and Gas Commission. 2011. Investigation of observed seismicity in the Horn River basin, Report of British Columbia Oil and Gas Commission. http://www.bcogc.ca/node/8046/download.

Chasset, C., Jarsjo, J., Erlstrom, M. et al. 2011. Scenario Simulations of CO_2 Injection Feasibility, Plume Migration and Storage in a Saline Aquifer, Scania, Sweden. *Int J Greenh Gas Control* **5** (5): 1303–1318. https://doi.org/10.1016/j.ijggc.2011.06.003.

Dusseault, M. B. 2010. Deep Injection Disposal: Environmental and Petroleum Geomechanics. Presented at the ISRM International Symposium 2010 and 6th Asian Rock Mechanics Symposium – Advances in Rock Engineering, New Delhi, India, 23-27 October. ISRM-ARMS6-2010-168.

Ehlig-Economides, C. and Economides M. J. 2010. Sequestering Carbon Dioxide in a Closed Underground Volume. *J Pet Sci & Eng* **70** (1-2): 123-130. http://doi.org/10.1016/j.petrol.2009.11.002.

Fan, Z., Eichhubl, P., and Gale, J. F. W. 2016. Geomechanical analysis of fluid injection and seismic fault slip for the M_w 4.8 Timpson, Texas, earthquake sequence. *Journal of Geophysical Research: Solid Earth* **121** (4): 2798–2812. http://dx.doi.org/10.1002/2016JB012821.

Friberg, P.A., Besana-Ostmanb, G.M., and Dricker, I. 2014. Characterization of an earthquake sequence triggered by hydraulic fracturing in Harrison County, Ohio. *Seismological Research Letters (2014)* **85** (6): 1295-1307. https://doi.org/10.1785/0220140127.

Gogri M.P., Rohleder J., Kabir C. et al. 2017. Prognosis for safe water-disposal-well operations and practiced based on reservoir flow modeling and real-time performance analysis. Paper SPE-187083-MS presented at the SPE annual conference and exhibition in San Antonio, Texas, 9-11 October 2017. https://doi.org/10.2118/187083-MS.

Gono, V., Olson, J. E., and Gale, J. F. 2015. Understanding the Correlation between Induced Seismicity and Wastewater Injection in the Fort Worth Basin. Presented at the 49th US Rock Mechanics/Geomechanics Symposium, San Francisco, California, USA, 28 June – 1 July. ARMA-2015-419.

Goodman, A., Hakala, A., Bromhal, G. et al. 2011. U. S. DOE Methodology for the Development of Geologic Storage Potential for Carbon Dioxide at the National and Regional Scale. *Int J Greenh Gas Control* **5** (4): 952-965. https://doi.org/10.1016/j.ijggc.2011.03.010.

Hall, H. N. 1953. Compressibility of Reservoir Rocks. *J Pet Technol* **5** (1): 17–19. SPE-953309-G. https://doi.org/10.2118/ 953309-G.

Holland, A. 2011. Examination of Possibly Induced Seismicity from Hyfraulic Fracturing in the Eola Field, Garvin County, Oklahoma. OF1-2011. Oklahoma Geological Survey, Norman, Oklahoma (March 2011).

Holland, A. 2013. Earthquakes triggered by hydraulic fracturing in south-central Oklahoma. *Bulletin of the Seismological Society of America* **103** (3): 1784-1792. https://doi.org/10.1785/0120120109.

Henao, T. 2017. *Multistage Triaxial Test on Conventional and Unconventional Rocks*. Master's thesis, University of Oklahoma, Norman, Oklahoma.

Holubnyak, Y. 2016. Reservoir Modeling of CO_2 Injection in Arbuckle Saline Aquifer at Wellington Field, Summer County, Kansas. OFR-2016-29. Kansas Geological Survey, Lawrence, Kansas (October 2016).

Horton, S. 2012. Disposal of hydrofracking waste fluid by injection into subsurface aquifers triggers earthquake swarm in central Arkansas with potential for damaging earthquake. *Seismol. Res. Lett.* **83**, 250–260.

Houze, O., Viturat, D., and Fjaere, O.S. 2017. Dynamic Data Analysis. v. 5.10. Chap. 4. https://www.kappaeng.com/documents/flip/dda512/.

International Energy Agency Greenhouse Gas. 2009. Development of Storage Coefficients for Carbon Dioxide Storage in Deep Saline Formations. 2009/13. IEAGHG, Chelteham, Gloucestershire, UK (November 2009).

International Energy Agency Greenhouse Gas. 2010. Pressurisation and Brine Displacement Issues for Deep Saline Formation CO_2 Storage. 2010/15. IEAGHG, Chelteham, Gloucestershire, UK (November 2010).

Izgec, B. and Kabir, C. S. 2009. Real-Time Performance Analysis of Water-Injection Wells. *SPE Res Eval & Eng* **12** (1): 116–123. SPE-109876-PA. https://doi.org/10.2118/109876-PA.

Izgec, B. and Kabir C. S. 2011. Identification and Classification of High-Conductive Layers in Waterfloods. *SPE Res Eval & Eng* **14** (1): 113–119. SPE-123930-PA. https://doi.org/10.2118/123930-PA.

Jacobs, T. 2016. Seismic Shifts in Oklahoma Lead to Stricter Regulations. *J Pet Technol* **68** (5): 44–48. SPE-0516-0044-JPT. https://doi.org/10.2118/0516-0044-JPT.

Jalalah, A. A. 2006. Compressibility of Porous Rocks: Part II. New relationships. *Acta Geophysica* **54** (4): 399–412. https://doi.org/10.2478/s11600-006-0029-4.

Johnson, K.S., 1991, Geologic overview and economic importance of Late Cambrian and Ordovician rocks in Oklahoma, in Johnson, K. S., ed., Late Cambrian-Ordovician geology of the southern Midcontinent, 1989 Symposium: Oklahoma Geological Survey Circular **92**, 3-14.

Karasatathis, A. 2007. *Petrophysical Measurements on a Tight Gas Shale*. Master's thesis, University of Oklahoma, Norman, Oklahoma.

Kazemi, H., 1969. Pressure transient analysis of naturally fractured reservoirs with uniform fracture distribution. *SPE Journal* **9** (4), 451–462. SPE-2156-A. https://doi.org/10.2118/2156-A.

Kim, W.Y. 2013 Induced seismicity associated with fluid injection into a deep well in Youngstown, Ohio. *Geophys. Res.* **118**, 3506–3518.

Kumar, A., Noh, M. H., Ozah, R. C. et al. 2005. Reservoir Simulation of CO_2 Storage in Aquifers. *SPE J.* **10** (3), 336–348. 89343-PA. http://dx.doi.org/10.2118/89343-PA.

Macary, S., Tenizbaeva, B., Azhigaliyeva, A. et al. 2012. Waste Water Disposal Has Become Critical Strategic Focus Area. Presented at the SPE Russian Oil & Gas Exploration & Production Technical Conference and Exhibition, Moscow, Russia, 16-18 October 2012. SPE-160769-RU. https://doi.org/10.2118/160769-RU.

McGarr, A., Bekins, B., Burkardt, N. et al. 2015. Coping with earthquakes induced by fluid injection. *Science*. **347**, 830–831.

Morgan, B. C. and Murray, K. E. 2015. Characterizing Small-Scale Permeability of the Arbuckle Group, Oklahoma. OF2-2015. Oklahoma Geological Survey, Norman, Oklahoma (9 March).

Murray, K. E. 2013. State-scale perspective on water use and production associated with oil and gas operations, Oklahoma, U.S. *Environ. Sci. Technol.* **47**, 4918–4925.

Murray, K. E. 2014. Class II underground injection control well data for 2010–2013 by geologic zones of completion, Oklahoma. OF1-2014. Oklahoma Geological Survey, Norman, Oklahoma.

Murray, K. E. 2015. Class II Saltwater Disposal for 2009–2014 at the Annual-, State-, and County- Scales by Geologic Zones of Completion, Oklahoma. OF5-2015. Oklahoma Geological Survey, Norman, Oklahoma (31 December).

Newman, G. H. 1973. Pore-volume compressibility of consolidated, friable, and unconsolidated reservoir rocks under hydrostatic loading. *J Pet Technol* **25** (2): 129–134. SPE-3835-PA. https://doi.org/10.2118/ 3835-PA.

Oklahoma Corporation Commission. 2017. Oil and Gas Info. Occeweb, https://apps.occeweb.com/RBDMSWeb_OK/OCCOGOnline.aspx (accessed 10 January 2017).

Pawar, R. J., Bromhal, G. S., Carey, J. W. et al. 2015. Recent Advances in Risk Assessment and Risk Management of Geologic CO_2 Storage. *Int J Greenh Gas Control* **40** (September): 292–311. http://dx.doi.org/10.1016/j.ijggc.2015.06.014.

Person, M., Banerjee, A., Rupp, J. et al. 2010. Assessment of Basin-Scale Hydrologic Impacts of CO_2 Sequestration, Illinois basin. *Int J Greenh Gas Control* **4** (5): 840–854. https://doi.org/10.1016/j.ijggc.2010.04.004.

Saripalli, K.P., Sharma, M. M., and Bryant, S. L. 2000. Modeling Injection Well Performance during Deep-Well Injection of Liquid Wastes. *Journal of Hydrology* **227** (1-4): 41-55. https://doi.org/10.1016/S0022-1694(99)00164-X.

Schlumberger. 1991. *Log Interpretation Principles/Applications*. Sugar Land, TX: Schlumberger.

Shafer, L. 2011. Water Recycling and Purification in the Pinedale Anticline Field: Results from the Anticline Disposal Project. Presented at the SPE Americas E&P Health, Safety, Security and Environmental Conference, Houston, Texas, USA, 21-23 March. SPE-141448-MS. https://doi.org/10.2118/141448-MS.

Silin, D.B., Holtzman R., Patzek, T.W. et al. 2005. Waterflood Surveillance and Control: Incorporating Hall Plot and Slope Analysis. Presented at the SPE Annual Technical Conference and Exhibition, Dallas, TX, USA 9-12 October. SPE-95685-MS. https://doi.org/10.2118/95685-MS.

Sondergeld, C. H. and Rai, C. S. 1993. A New Exploration Tool: Quantitative Core Characterization. *Pure and Applied Geophysics* **141** (2): 249-268. https://doi.org/10.1007/BF00998331.

Sopher, D., Juhlin, C., and Erlstorm, M. 2014. A Probabilistic Assessment of the Effective CO_2 Storage Capacity within the Swedish Section of the Baltic Basin. *Int J Greenh Gas Control* **30** (November): 148-170. https://doi.org/10.1016/j.ijggc.2014.09.009.

Stringer Jr., C.P. 1958. Subsurface Geology of Western Payne County, Oklahoma: Oklahoma City Geological Society, *The Shale Shaker Digest II*, **VI-VIII**, 258-273

The Royal Society. 2012. Shale gas extraction in the UK: A review of hydraulic fracturing. The Royal Society and the Royal Academy of Engineering (June 2012). https://royalsociety.org/topics-policy/projects/shale-gas-extraction.

U.S. Geological Survey. 2017. USGS FAQs. https://www2.usgs.gov/faq/categories/9833/3424_home (accessed 10 April 2017).

U.S. Environmental Protection Agency. 2014. Minimizing and Managing Potential Impacts of Injection-Induced Seismicity from Class II Disposal Well: Practical Approaches. Revised Report. US EPA, Washington, DC (November 12, 2014).

Umholtz, N. and Ouenes, A. 2016. The Effects of Faults on Induced Seismicity Potential during Water Disposal and Hydraulic Fracturing. Presented at the SPE Western Regional Meeting, Anchorage, Alaska, USA 23-26 May 2016. SPE-180461-MS. https://doi.org/10.2118/180461-MS.

Veil, J. A. and Clark, C. E. 2011. Produced Water Volume Estimates and Management Practices. *SPE Prod Oper* **26** (3): 234–239. SPE-125999-PA. https://doi.org/10.2118/125999-PA.

Veil, J. A., Harto, C. B., and McNemar, A. T. 2011. Management of Water Extracted from Carbon Sequestration Projects: Parallels to Produced Water Management. SPE Americas E&P Health, Safety, Security and Environmental Conference, Houston, Texas, USA 21-23 March 2011. https://doi.org/10.2118/140994-MS.

Walsh, F. R. and Zoback, M. D. 2015. Oklahoma's Recent Earthquakes and Saltwater Disposal. *Science Advances* **1** (5): 9. http://doi.org/10.1126/sciadv.1500195.

Walters, R. J., Zoback, M. D., Baker, J. W., et al. 2015. Characterizing and Responding to Seismic Risk Associated with Earthquakes Potentially Triggered by Fluid Disposal and Hydraulic Fracturing. *Seismological Research Letters* **86** (4): 1110-1118.

White, J. A. and Foxall, W. 2016. Assessing Induced Seismicity Risk at CO_2 Storage Projects: Recent Progress and Remaining Challenges. *Int J Greenh Gas Control* **49** (June): 413–424. http://doi.org/10.1016/j.ijggc.2016.03.021.

Wolaver, B. D., Hovorka, S. D., and Smyth, R. C. 2013. Greensites and Brownsites: Implications for CO_2 Sequestration Characterization, Risk Assessment, and Monitoring. *Int J Greenhouse Gas Control* **19** (November): 49–62. http://dx.doi.org/10.1016/j.ijggc.2013.07.020.

www.earthquakes.ok.gov. 2017. Earthquakes in Oklahoma (accessed 10 December 2017).

Yamamoto, H., Zhang, K., Karasaki, K. et al. 2009. Numerical Investigation Concerning the Impact of CO_2 Geologic Storage on Regional Groundwater Flow. *Int J Greenh Gas Control* **3** (5): 586–599. https://doi.org/10.1016/j.ijggc.2009.04.007.

Zhou, Q., Birkholzer, J. T., Tsang, C. F. et al. 2008. A Method for Quick Assessment of CO_2 Storage Capacity in Closed and Semi-Closed Saline Formations. *Int J Greenh Gas Control* **2** (4): 626–639. http://dx.doi.org/10.1016/j.ijggc.2008.02.004.

Zhu, C., Fan, Z., and Eichhubl, P. 2017. The effect of variable fluid injection rate on the stability of seismogenic faults. Presented at the 51st US Rock Mechanics/Geomechanics Symposium, San Francisco, California, USA, 25-28 June. ARMA-2017-0098.

Zimmerman, R. W., Somerton, W. H., and King, M. S. 1986. Compressibility of Porous Rocks. *Journal of Geophysical Research: Solid Earth* **91** (B12): 12,765–12,777. http://dx.doi.org/10.1029/JB091iB12p12765.

Zoback, M. D., Hickman, S. and Ellsworth, W. 2010. Scientific Drilling into the San Andreas Zone. *Eos Trans,* AGU, **91** (22), 197-199. http://dx.doi.org/10.1029/2010EO220001.

Zoback, M. D. 2012. Managing the seismic risk posed by wastewater disposal. *Earth Mag.* **57**, 38–43.

Appendix I: Ambient Reservoir Pressure of 29 wells

Table 15. Values of Ambient Reservoir Pressure calculated using Silin slope analysis

Well Name	Ambient Reservoir Pressure (psi)
Well A	2285
Well B	2750
Well C	2450
Well D	2975
Well E	2350
Well F	2815
Well G	2545
Well H	2700
Well I	2737
Well J	2630
Well K	2260
Well L	2271
Well M	2675
Well N	3000
Well O	2468
Well P	2900
Well Q	2630
Well R	2515
Well S	2604
Well T	2375
Well U	2725
Well V	2630
Well W	2740
Well X	2500
Well Y	2325
Well Z	2635
Well AA	2750
Well AB	2600
Well AC	2525

Appendix II: Modified-Hall Plots of 29 wells

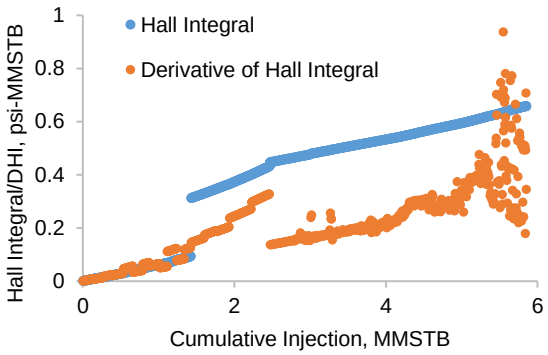

Figure 121. Behavior of injection well using modified-Hall plot for Well A

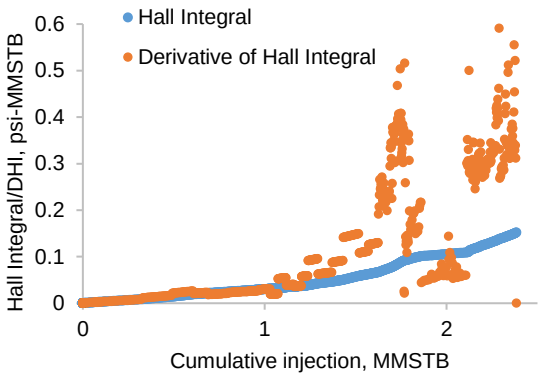

Figure 122. Behavior of injection well using modified-Hall plot for Well B

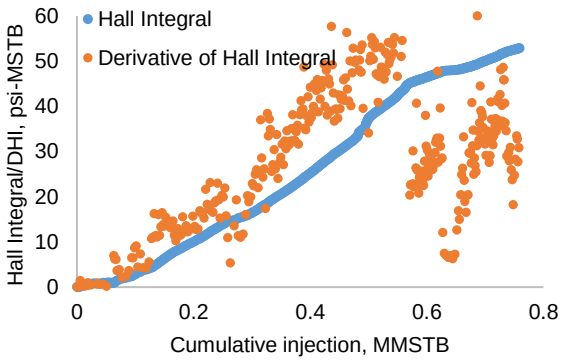

Figure 123. Behavior of injection well using modified-Hall plot for Well C

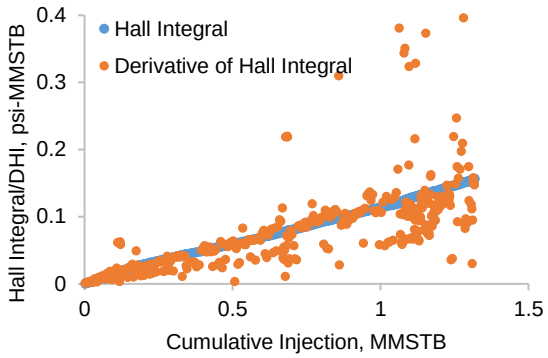

Figure 124. Behavior of injection well using modified-Hall plot for Well D

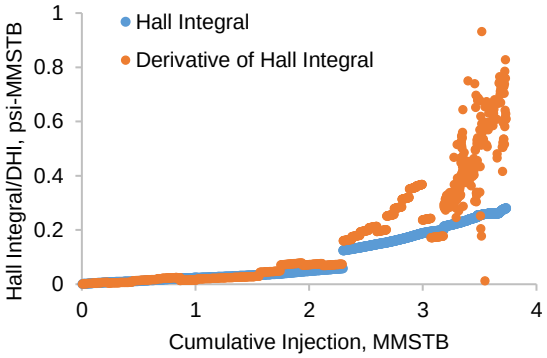

Figure 125. Behavior of injection well using modified-Hall plot for Well E

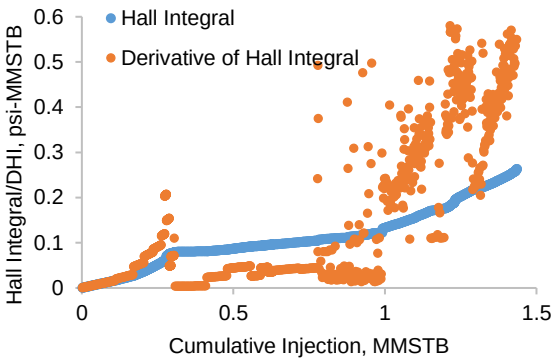

Figure 126. Behavior of injection well using modified-Hall plot for Well F

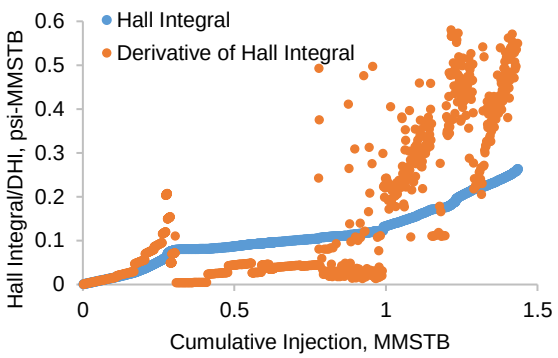

Figure 127. Behavior of injection well using modified-Hall plot for Well G

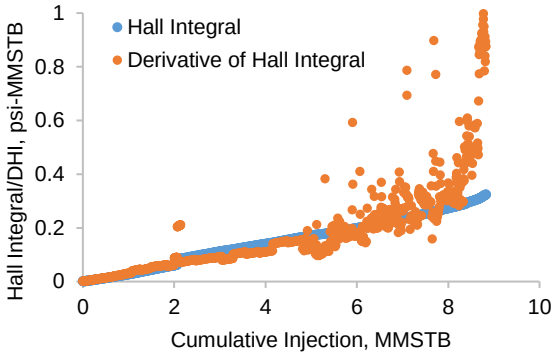

Figure 128. Behavior of injection well using modified-Hall plot for Well H

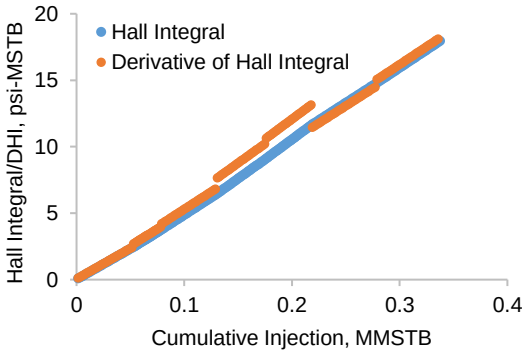

Figure 129. Behavior of injection well using modified-Hall plot for Well I

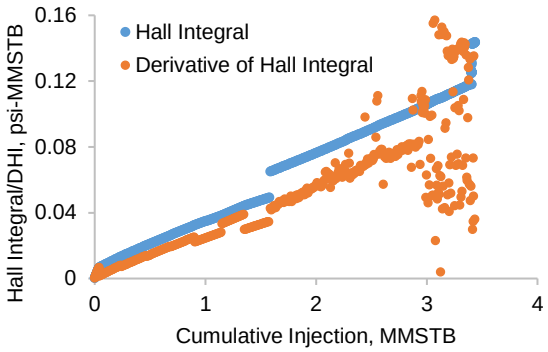

Figure 130. Behavior of injection well using modified-Hall plot for Well J

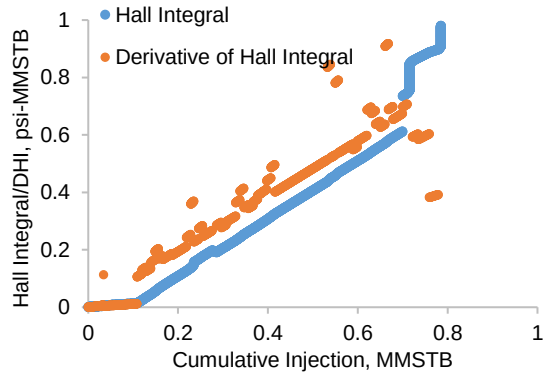

Figure 131. Behavior of injection well using modified-Hall plot for Well K

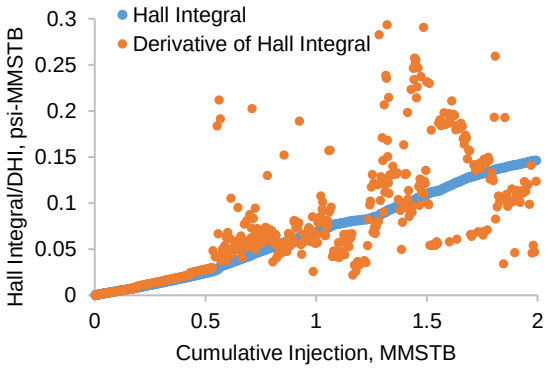

Figure 132. Behavior of injection well using modified-Hall plot for Well L

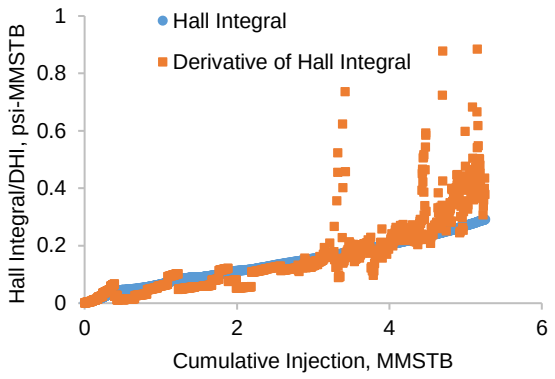

Figure 133. Behavior of injection well using modified-Hall plot for Well M

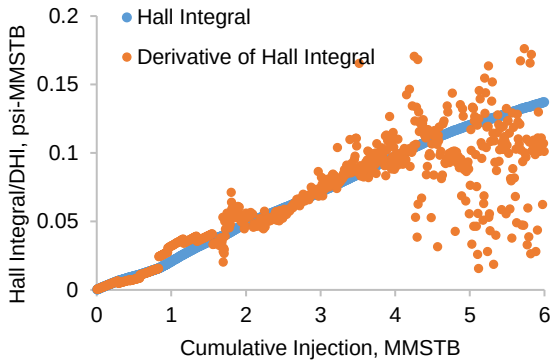

Figure 134. Behavior of injection well using modified-Hall plot for Well N

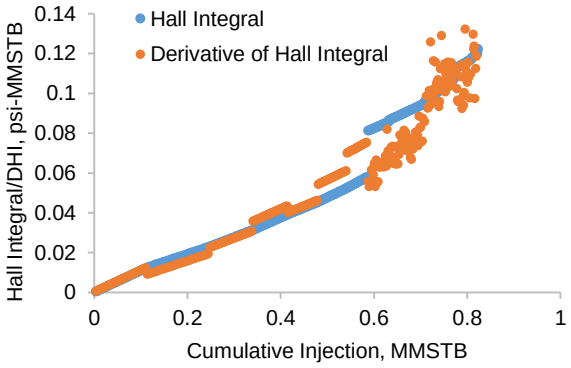

Figure 135. Behavior of injection well using modified-Hall plot for Well O

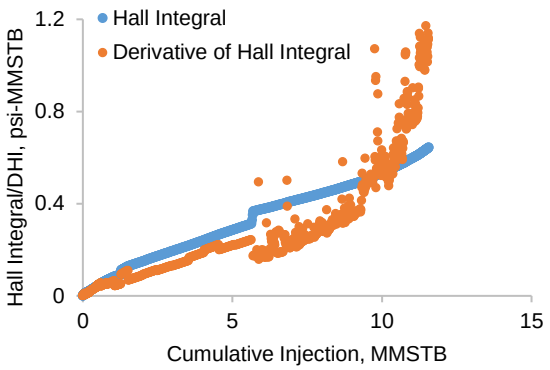

Figure 136. Behavior of injection well using modified-Hall plot for Well P

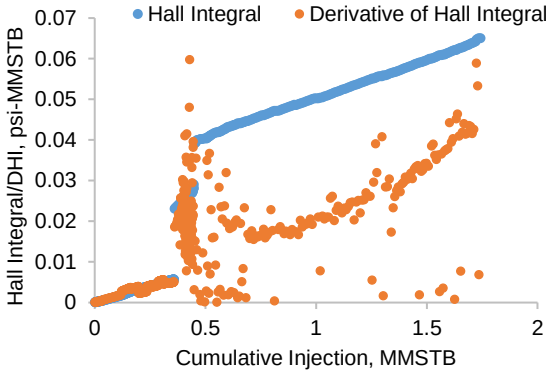

Figure 137. Behavior of injection well using modified-Hall plot for Well Q

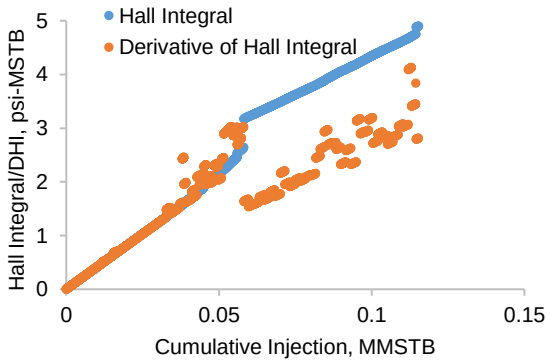

Figure 138. Behavior of injection well using modified-Hall plot for Well R

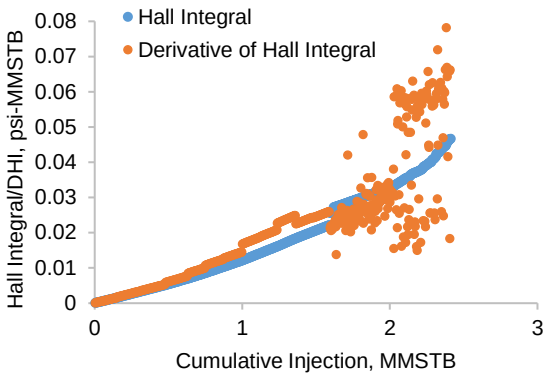

Figure 139. Behavior of injection well using modified-Hall plot for Well S

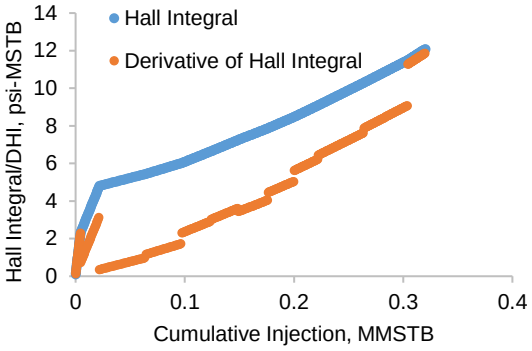

Figure 140. Behavior of injection well using modified-Hall plot for Well T

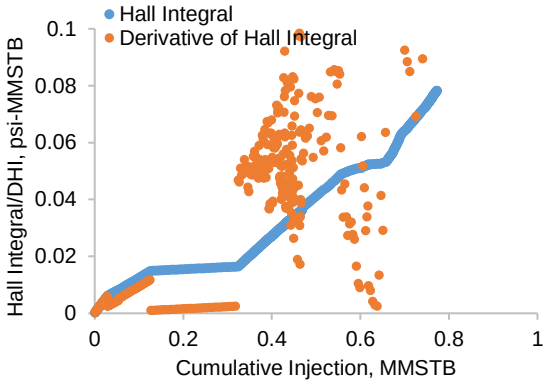

Figure 141. Behavior of injection well using modified-Hall plot for Well U

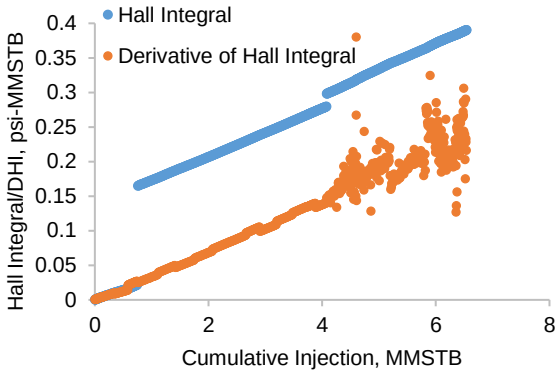

Figure 142. Behavior of injection well using modified-Hall plot for Well V

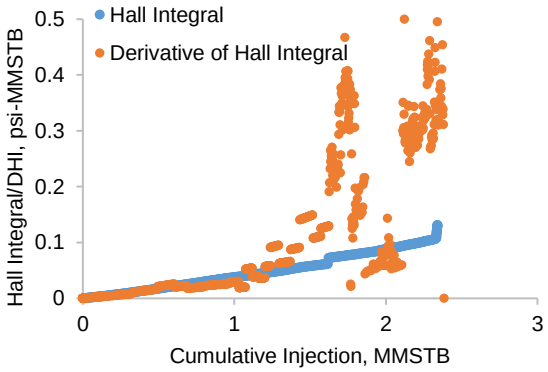

Figure 143. Behavior of injection well using modified-Hall plot for Well W

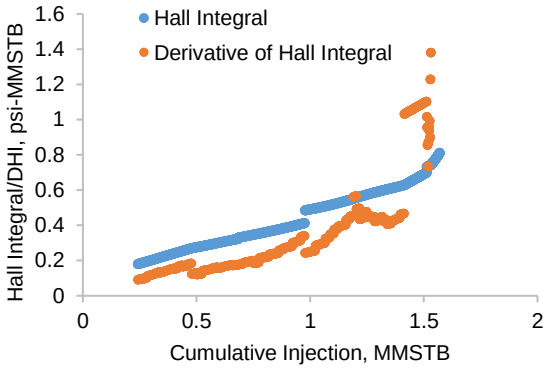

Figure 144. Behavior of injection well using modified-Hall plot for Well X

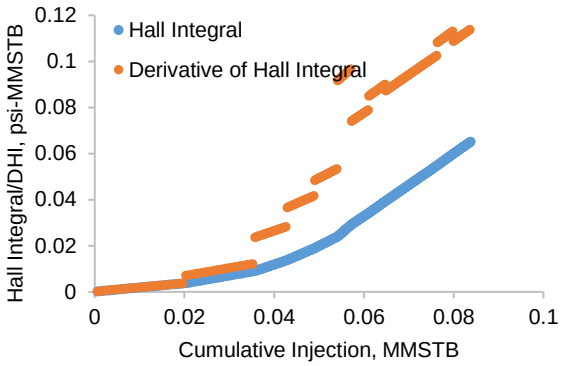

Figure 145. Behavior of injection well using modified-Hall plot for Well Y

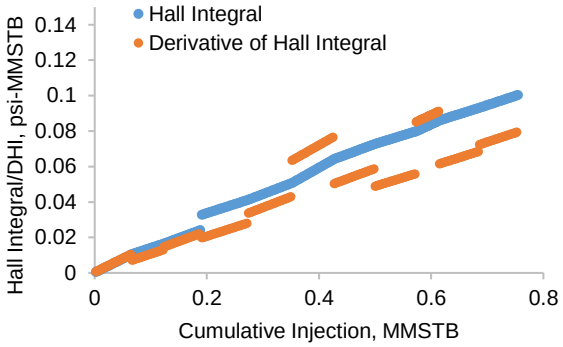

Figure 146. Behavior of injection well using modified-Hall plot for Well Z

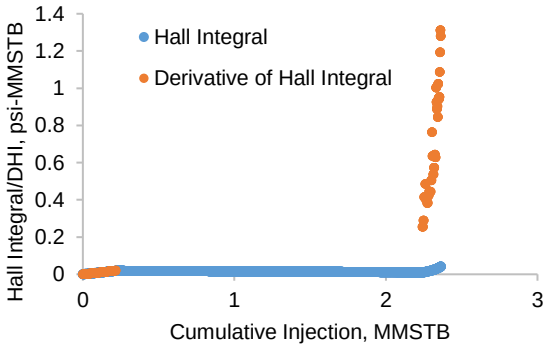

Figure 147. Behavior of injection well using modified-Hall plot for Well AA

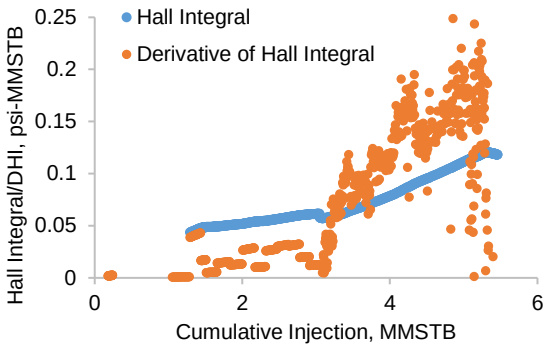

Figure 148. Behavior of injection well using modified-Hall plot for Well AB

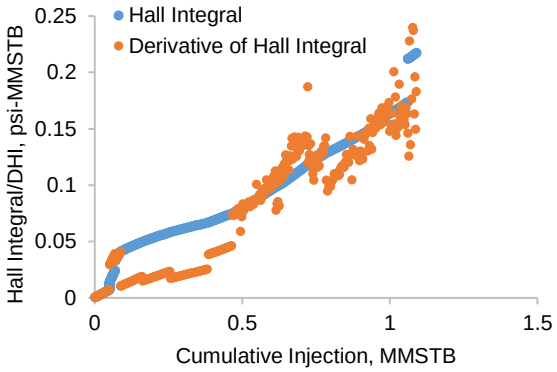

Figure 149. Behavior of injection well using modified-Hall plot for Well AC